

CHARACTERIZATION AND EVALUATION OF GPS PPP  
TECHNIQUES FOR OPTICAL CLOCK COMPARISONS

Von der Fakultät für Mathematik und Physik  
der Gottfried Wilhelm Leibniz Universität Hannover

zur Erlangung des akademischen Grades  
Doktorin der Naturwissenschaften  
Dr. rer. nat.

genehmigte Dissertation von  
Dipl.-Phys. Julia Leute

Referent: PD Dr. Ekkehard Peik  
Koreferent: Prof. Dr. Steffen Schön  
Tag der Promotion: 28.06.2017

## ABSTRACT

---

In the 50 years since the redefinition of the second based on the hyperfine transition of the ground state of the  $^{133}\text{Cs}$  atom, new atomic frequency standards based on optical transitions in various atomic species have been developed that surpass the best caesium atomic clocks in terms of accuracy and precision. Relative systematic frequency uncertainties as low as a few  $10^{-18}$  have been reported for optical clocks. The direct comparison of optical clocks developed at institutes around the world is an important step for the validation of their uncertainty budgets and to find the best candidates for a possible redefinition of the second. Global Positioning System (GPS) time and frequency transfer allows to compare atomic clocks on regional to intercontinental distances. For the new generation of optical clocks, the standard microwave time and frequency transfer techniques, reaching an instability of  $10^{-15}$  at one day averaging time, become a limiting factor in this comparisons.

In this work, the suitability of an improved GPS time and frequency transfer technique for the comparison of optical clocks at the  $10^{-16}$  level is investigated. Two GPS time and frequency transfer techniques, Precise Point Positioning (PPP) and Integer Precise Point Positioning (IPPP), are compared on a local baseline at Physikalisch-Technische Bundesanstalt (PTB) and on continental baselines between various European national metrology institutes (NMIs). PPP is based on undifferenced dual-frequency carrier-phase and code observations, whereas IPPP can be classified as a carrier-phase only method.

An optical fiber link established between PTB and Laboratoire national de métrologie et d'essais - Système de Références Temps-Espace (LNE-SYRTE) is used to characterize the PPP and IPPP links between both institutes. Due to its superior stability and accuracy, the optical fiber link serves as the ground truth and does not contribute noise to the comparison. For two different GPS stations at LNE-SYRTE, the agreement between the IPPP link and the optical fiber link is  $(-0.34 \pm 2.66) \times 10^{-16}$  and  $(-0.23 \pm 0.57) \times 10^{-16}$  for an averaging time of  $1.2 \times 10^6$  s and  $0.9 \times 10^6$  s respectively. For the PPP links on the other hand, the agreement with the optical fiber link is  $(-5.94 \pm 2.73) \times 10^{-16}$  and  $(1.23 \pm 1.07) \times 10^{-16}$ . A systematic frequency offset due to a code-phase inconsistency is observed for one of the PPP links, but not for the IPPP link using the same GPS stations.

Finally, direct remote frequency comparisons of  $^{171}\text{Yb}^+$  ion clocks developed at PTB and National Physical Laboratory (NPL) via IPPP links are performed. The impact of frequent dead time due to the limited duty cycle of the clocks on the statistical uncertainty of the clock frequency comparison via GPS link is studied. A method to optimize the statistical uncertainty of the clock comparison is applied that uses flywheel oscillators to bridge the frequent dead time. The average fractional frequency deviation of the clocks based on the electric quadrupole transition is  $y_{\text{PTB}} - y_{\text{NPL}} = (-1.46 \pm 0.55) \times 10^{-15}$  including the systematic uncertainties of the optical clocks. A systematic frequency offset, not accounted for in the systematic uncertainty budgets is observed. For the clocks based on the electric octupole transition, the average fractional frequency deviation is  $y_{\text{PTB}} - y_{\text{NPL}} = (-0.1 \pm 3.1) \times 10^{-16}$ , no systematic frequency offset is observed. Both results agree with indirect absolute frequency measurements against caesium fountain clocks. The statistical uncertainty is limited by the noise contribution of the flywheel oscillator at NPL that has a flicker floor of  $2 \times 10^{-15}$ .

**keywords:** *Frequency Transfer, GPS, Precise Point Positioning, Optical Clock*

## ZUSAMMENFASSUNG

---

In den 50 Jahren seit der Neudefinierung der Sekunde basierend auf dem Hyperfeinstrukturübergang des Grundzustandes des  $^{133}\text{Cs}$  Atoms, wurden atomare Frequenzstandards basierend auf optischen Übergängen entwickelt, welche die besten Cäsium-Atomuhren hinsichtlich ihrer Genauigkeit und Stabilität weit übertreffen. Relative systematische Unsicherheiten von wenigen  $10^{-18}$  wurden für optische Uhren erzielt. Der direkte Vergleich von optischen Uhren, welche an verschiedenen Instituten weltweit entwickelt werden, ist ein wichtiger Schritt für die Validierung ihrer Unsicherheitsbudgets und um die besten Kandidaten für eine Mögliche Neudefinierung der Sekunde zu finden. Global Positioning System (GPS) Zeit- und Frequenzübertragung erlaubt den Vergleich von Atomuhren von regionalen bis zu interkontinentalen Distanzen. Für die Frequenzvergleiche von optischen Uhren stellen die klassischen satellitenbasierten Zeit- und Frequenzübertragungsmethoden mit einer Instabilität von  $10^{-15}$  bei einer Mittelungszeit von einem Tag eine Limitierung dar.

In dieser Arbeit wird die Eignung einer verbesserten GPS Zeit- und Frequenzübertragungsmethode für den Vergleich optischer Uhren auf dem  $10^{-16}$  Niveau untersucht. Zwei Frequenzübertragungsmethoden, Precise Point Positioning (PPP) und Integer Precise Point Positioning (IPPP), werden auf lokalen Basislinien an der Physikalisch-Technische Bundesanstalt (PTB) und auf kontinentalen Basislinien zwischen europäischen Metrologieinstituten verglichen. PPP basiert auf undifferenzierten Trägerphasen- und Codebeobachtungen, wohingegen IPPP als eine reine Trägerphasenmethode klassifiziert werden kann.

Ein optischer Faserlink zwischen PTB und Laboratoire national de métrologie et d'essais - Système de Références Temps-Espace (LNE-SYRTE) wird zur Charakterisierung der PPP und IPPP Links zwischen den Instituten verwendet. Dank seiner besseren Stabilität und Genauigkeit trägt er kein Rauschen zu dem Vergleich bei und dient als Referenzmessung. Für zwei verschiedene GPS Stationen am LNE-SYRTE stimmen der IPPP Link und der Faserlink zwischen PTB und LNE-SYRTE auf  $(-0.34 \pm 2.66) \times 10^{-16}$  und  $(-0.23 \pm 0.57) \times 10^{-16}$  überein bei eine Mittelungszeit von  $1.2 \times 10^6$  s beziehungsweise  $0.9 \times 10^6$  s. Für die PPP links auf der anderen Seite ist Übereinstimmung mit dem Faserlink  $(-5.94 \pm 2.73) \times 10^{-16}$  und  $(1.23 \pm 1.07) \times 10^{-16}$ . Eine systematische Frequenzabweichung aufgrund einer Code-Trägerphaseninkonsistenz wurde für einen der PPP Links beobachtet.

In dieser Arbeit werden  $^{171}\text{Yb}^+$  Uhren, welche an der PTB und am National Physical Laboratory (NPL) entwickelt werden, mit Hilfe von PPP und IPPP Links verglichen. Der Einfluss von Totzeiten der optischen Uhren auf die statistische Unsicherheit des Uhrenvergleichs via GPS Links wird untersucht. Eine Methode zur Optimierung der statistischen Unsicherheit des Uhrenvergleichs wird angewendet, welche die Lokaloszillatoren zur Überbrückung der Totzeiten nutzt.

Die gemittelte relative Frequenzabweichung der Uhren basierend auf dem elektrischen Quadrupol-Übergang in  $^{171}\text{Yb}^+$  ist  $y_{\text{PTB}} - y_{\text{NPL}} = (-1.46 \pm 0.55) \times 10^{-15}$ , wobei die systematische Unsicherheit der Uhren bereits berücksichtigt ist. Eine systematische Frequenzabweichung wurde beobachtet, die nicht vom Unsicherheitsbudget abgedeckt wird. Für die Uhren basierend auf dem elektrischen Oktupol-Übergang beträgt die gemittelte relative Frequenzabweichung  $y_{\text{PTB}} - y_{\text{NPL}} = (-0.1 \pm 3.1) \times 10^{-16}$ , keine systematische Frequenzabweichung wurde beobachtet. Beide Ergebnisse stimmen mit lokalen Absolutfrequenzmessungen mit Cäsium-Fontänenuhren überein. Die erreichte statistische Unsicherheit ist limitiert durch den Rauschbeitrag des Lokaloszillators am NPL, der einen Flickerfloor von  $2 \times 10^{-15}$  hat.

**Schlagwörter:** *Frequenzübertragung, GPS, Precise Point Positioning, Optische Uhr*

# CONTENTS

---

Introduction	1
1 Frequency Stability Analysis	4
1.1 Phase and Frequency Noise	4
1.2 Time Domain Stability	5
1.2.1 Autocovariance and Standard Variance	6
1.2.2 Two-sample Variances	6
1.3 Fourier Frequency Domain Stability	7
1.3.1 Autocovariance and Standard Variance	7
1.3.2 Two-sample Variances	8
1.4 Conversion between Standard and Two-sample Variances	9
1.5 Effect of Dead Time on the Variances	11
1.5.1 Standard Variance with Dead Time	11
1.5.2 Allan Variance (AVAR) with Dead Time	13
1.6 $\Lambda$ -Weighted Sample Mean and its Variance	16
1.7 Discrimination of Additional Power-Law Noise Types	18
1.7.1 B-spline Basis Functions and Wavelets	18
1.7.2 Parzen Weighting Function	21
1.7.3 B-spline Weighted Sample Mean	22
1.8 Noise Simulation	23
1.9 Summary	23
2 GPS Time and Frequency Transfer Techniques	25
2.1 GPS Observations	25
2.2 Linear Combinations of Observations	27
2.2.1 Wide-lane (WL) Linear Combination	27
2.2.2 Narrow-lane (NL) Linear Combination	28
2.2.3 Melbourne-Wübbena (MW) Linear Combination	28
2.2.4 Ionosphere-free Linear Combinations	29
2.3 International GNSS Service (IGS)	29
2.4 Common-View (CV) and All-in-View (AV)	30
2.5 Precise Point Positioning (PPP)	31
2.5.1 Standard Observation Model	31
2.5.2 Code-Phase Inconsistencies	33
2.5.3 Parameter Adjustment	34
2.5.4 Batch-Boundary Discontinuities	35
2.5.5 Continuous PPP solutions	36
2.6 Integer Precise Point Positioning (IPPP)	38
2.6.1 Decoupled Clock Model	38
2.6.2 User Ambiguity Resolution	38
2.6.3 Precise Integer Satellite Products	39
2.6.4 Link Formation	40
2.7 Summary	41

3	GPS Link Characterizations	42
3.1	Station Hardware Stability . . . . .	42
3.2	Local Common-Clock Baselines . . . . .	44
3.2.1	Long-term Code-CV Analysis . . . . .	44
3.2.2	PPP and IPPP Analysis . . . . .	45
3.3	Continental Baselines . . . . .	49
3.3.1	International Timescales with Optical Clocks (ITOC) . . . . .	49
3.3.2	PTB-LNE-SYRTE Baseline . . . . .	54
3.3.3	PTB-NPL Baseline . . . . .	56
3.4	Fiber Link Comparison on the PTB-LNE-SYRTE Baseline . . . . .	60
3.4.1	Experimental Setup . . . . .	60
3.4.2	Data Analysis . . . . .	61
3.4.3	Results and Discussion . . . . .	61
3.5	Summary . . . . .	65
4	Direct Remote Frequency Comparisons of Optical Clocks	66
4.1	Principles of Remote Frequency Comparisons of Optical Clocks . . .	66
4.1.1	Local and Remote Measurements . . . . .	66
4.1.2	Data Analysis Strategies . . . . .	68
4.1.3	Estimation of the Statistical Uncertainty Contributions . . . . .	70
4.2	Remote Comparison of Yb <sup>+</sup> Ion Clocks between PTB and NPL . . . . .	72
4.2.1	Measurement Campaign using the Quadrupole Transition . . .	72
4.2.2	Measurement Campaign using the Octupole Transition . . . . .	76
4.3	Summary . . . . .	77
	Outlook	79
	Bibliography	81

LIST OF FIGURES

---

Figure 1	Weighting functions for the standard and two-sample variances. . . . .	5
Figure 2	Fractional frequency deviations for power-law noise types: white, flicker and random walk frequency modulation. . . . .	8
Figure 3	Sigma-tau plot for ADEV and MDEV. . . . .	9
Figure 4	Weighting function for the sample mean with dead time and $\Pi$ -averaging of the individual samples. . . . .	11
Figure 5	Autocorrelation with dead time for flicker phase modulation (FPM). . . . .	13
Figure 6	Weighting function for the AVAR with dead time. . . . .	14
Figure 7	Effect of regularly distributed dead time on the ADEV for WPM. . . . .	15
Figure 8	Weighting function for the $\Lambda$ -weighted sample mean and the $\Pi$ -weighted sample mean of $\Lambda$ -averaged samples. . . . .	16
Figure 9	N-dependence of the $\Lambda$ -weighted deviation of the sample mean and the $\Pi$ -weighted deviation of the sample mean for $\Lambda$ -averaged samples. . . . .	17
Figure 10	B-spline basis functions and derivatives. . . . .	19
Figure 11	Weighting functions $w_{\sigma_k, n}$ with n-th order differences of smoothness k and their relationship described by n-th order derivatives. . . . .	20
Figure 12	Dependence of the two-sample variance for the k = 3 B-spline weighting function on $\tau$ for various noise types demonstrated based on simulated power-law noise. . . . .	21
Figure 13	Demonstration of the two-scale relation for the 3rd order B-spline (Parzen window). . . . .	22
Figure 14	Spectral density and MDEV for simulated power-law noise types. . . . .	24
Figure 15	Schematic depiction of the AV and CV methods. . . . .	30
Figure 16	Daily and continuous batch PPP clock comparison on PTB common-clock baseline . . . . .	37
Figure 17	Example of day-boundary discontinuities in an IPPP link. . . . .	40
Figure 18	Experimental setup for local common-clock baseline for GPS link characterizations. . . . .	44
Figure 19	GNSS installations on the rooftop of the Kopfermann building at PTB. . . . .	45
Figure 20	CV time difference for common-clock baselines at PTB. . . . .	46
Figure 21	MDEV for long-term Code-CV analysis of common-clock baselines at PTB. . . . .	46
Figure 22	PPP and IPPP time difference for local common-clock baselines at PTB. . . . .	48
Figure 23	PPP and IPPP frequency stability for a common-clock baselines at PTB. . . . .	48
Figure 24	Frequency standards developed at the European NMIs involved in the ITOC measurement campaigns. . . . .	49
Figure 25	Impact of the number of estimated tropospheric zwd parameters on the IPPP frequency stability for the PTB-LNE-SYRTE baseline. . . . .	50
Figure 26	PPP and IPPP frequency stability for European baselines between LNE-SYRTE, NPL and PTB. . . . .	51

Figure 27	Frequency instability for PPP and IPPP links on European baselines between PTB, NPL, INRIM and LNE-SYRTE. . . . .	53
Figure 28	Time difference for active hydrogen maser (AHM) comparison with PTB station KOP1 and LNE-SYRTE station OPMT via batch PPP, daily PPP, IPPP and Code-CV. . . . .	54
Figure 29	WRB for OPMT and KOP1 station during the 2015 measurement campaign. . . . .	55
Figure 30	Time difference for PPP and IPPP AHM comparisons between PTB and LNE-SYRTE using two different stations at LNE-SYRTE. . . . .	55
Figure 31	Time difference for PPP and IPPP local common clock local at LNE-SYRTE using OPMT and OPM8 station. . . . .	56
Figure 32	Frequency stability for PPP and IPPP on European baselines between PTB, NPL, INRIM and LNE-SYRTE with OPM8 station. . . . .	56
Figure 33	WRB for NP11 and KOP1 station during the campaign in 2014. . . . .	58
Figure 34	Time difference for the PPP and IPPP links on the NPL-PTB baseline during the 2014 measurement campaign. . . . .	58
Figure 35	Time difference for the PPP and IPPP links between NPL and PTB during the 2015 measurement campaign. . . . .	58
Figure 36	WRB for NP11 and KOP1 station during the campaign in 2015. . . . .	59
Figure 37	Difference between the PPP and IPPP links on the NPL-PTB baseline during the 2015 measurement campaign. . . . .	59
Figure 38	Simplified experimental setup for the characterization of GPS links between LNE-SYRTE and PTB using an optical fiber link. . . . .	60
Figure 39	Fractional frequency deviations of the AHM comparison via GPS and optical fiber link. . . . .	62
Figure 40	Frequency instability of the AHM comparison via GPS and optical fiber link. . . . .	63
Figure 41	Experimental setup for remote frequency comparisons of optical clocks using GPS . . . . .	66
Figure 42	Typical instabilities of oscillators and GPS for remote optical clock comparisons. . . . .	67
Figure 43	Set of intervals of the remote flywheel comparison, and the two local comparisons between the optical clocks and the flywheel oscillators. . . . .	68
Figure 44	Set of intervals for the remote flywheel comparison and the two local comparisons between the optical clocks and the flywheel oscillators in the extrapolation case. . . . .	69
Figure 45	Measurement schedule for local measurement at NPL. . . . .	73
Figure 46	ADEV for flywheel oscillators and PPP link for NPL-PTB $\text{Yb}^+$ frequency comparison. . . . .	73
Figure 47	Average fractional frequency difference for the comparison of the $^{171}\text{Yb}^+$ E2 transition between PTB and NPL. . . . .	75
Figure 48	Average fractional frequency difference for the comparison of the $^{171}\text{Yb}^+$ E3 transition between PTB and NPL. . . . .	76



## LIST OF TABLES

---

Table 1	Two-sample and standard variances for common noise types for $\Pi$ - and $\Lambda$ -weighted averages. . . . .	10
Table 2	N-scaling for the standard and two-sample variance with $\Pi$ -averaging for WPM and WFM with and without dead time. . . . .	15
Table 3	Dependence of the two-sample variance for k-th order B-spline weighting functions on $\tau$ depending on the noise type for various k. . . . .	19
Table 4	GNSS stations at PTB used in this work. . . . .	44
Table 5	GNSS stations at European NMIs used in this work. . . . .	50
Table 6	Average fractional frequency differences ( $\Pi$ -averaging) for AHMs comparisons via continuous PPP and IPPP links (MJD 56951-56960) for baselines between European NMIs. . . . .	51
Table 7	Average fractional frequency deviations ( $\Pi$ -averaging) of the AHM comparison via PPP and IPPP links (MJD 57 177-57 196) for baselines between European NMIs. . . . .	52
Table 8	AHM frequency comparison ( $\Pi$ -averaging) via PPP and IPPP links with LNE-SYRTE station OPM8 (MJD 57 183-57 196). . . . .	57
Table 9	Results of the comparison between the GPS links and the optical fiber link on the PTB-LNE-SYRTE baseline. . . . .	64
Table 10	GPS stations for AHM comparison between PTB and NPL. . . . .	72
Table 11	Noise models (AVAR at 1 s averaging time) of the flywheel oscillators H <sub>9</sub> and HM <sub>2</sub> , and the PPP and IPPP link between NPL and PTB. . . . .	74

## ACRONYMS

---

AC	analysis center
ACES	Atomic Clock Ensemble in Space
ADEV	Allan Deviation
AHM	active hydrogen maser
AVAR	Allan Variance
AOS	Astrogeodynamic Observatory
AV	All-in-View
BIPM	Bureau International des Poids et Mesures
C/A code	Coarse / Acquisition code
CNES	Centre National d'Études Spatiales
CV	Common-View
FPM	flicker phase modulation

FFM	flicker frequency modulation
GINS	Géodésie par Intégrations Numériques Simultanées
GMF	Global Mapping Function
GNSS	Global Navigation Satellite System
GPS	Global Positioning System
GPT	Global Pressure and Temperature
GUM	Central Office of Measures
IGS	International GNSS Service
IGST	IGS Time
INRIM	Istituto Nazionale di Ricerca Metrologica
IPPP	Integer Precise Point Positioning
IRC	integer recovery clock
ITOC	International Timescales with Optical Clocks
LNE-SYRTE	Laboratoire national de métrologie et d'essais - Système de Références Temps-Espace
MDEV	Modified Allan Deviation
MIKES	Mittatekniikan keskus
MJD	Modified Julian Date
MPQ	Max Planck Institute for Quantum Optics
MVAR	Modified Allan Variance
MW	Melbourne-Wübbena
NL	Narrow-lane
NMI	national metrology institute
NPL	National Physical Laboratory
NRCan	National Resources Canada
PCO	phase center offset
P code	Precision code
PCV	phase center variation
PE	polyethylene
PTB	Physikalisch-Technische Bundesanstalt
PPS	pulse per second
PPP	Precise Point Positioning
RMS	Root Mean Square
RRS	Revised Rinex Shift

RWFM	random walk frequency modulation
TAI	International Atomic Time
TDEV	Time Deviation
TSA	temperature-stabilized antenna
TVAR	Time Variance
TWSTFT	Two-Way Satellite Time and Frequency Transfer
USNO	United States Naval Observatory
UTC	Coordinated Universal Time
WFM	white frequency modulation
WL	Wide-lane
WPM	white phase modulation
WRB	wide-lane receiver bias
WSB	wide-lane satellite bias
zhd	zenith hydrostatic delay
zwd	zenith wet delay



*Just like moons and like suns, with the certainty of tides,  
just like hopes springing high, still I'll rise.*

Maya Angelou

## INTRODUCTION

---

During the 13th Conférence Générale des Poids et Mesures in 1967 (Terrien, 1968), the unit of time, the second, was redefined as

the duration of 9 192 631 770 periods of the radiation corresponding to the transition between the two hyperfine levels of the ground state of the caesium 133 atom.

This decision marks the moment of the transition from a definition of the second based on the motion of celestial bodies to a definition based on what is believed to be a constant of nature. It followed the development and testing of atomic clocks based on the hyperfine transition of the ground state of caesium atoms in the 1960s.

Caesium atomic clocks are passive frequency standards in which the frequency of an external microwave oscillator is used to interrogate the atoms, so that the frequency of the oscillator can be steered to be in resonance with the electronic transition of the atoms. The frequency uncertainty is proportional to the linewidth of the observed resonance feature and inversely proportional to the frequency of the transition. The linewidth is inversely proportional to the interrogation time, which could be increased by a factor of 100 in caesium fountain clocks compared to the classical caesium beam clocks, due to the development of laser cooling. For a given linewidth, the uncertainty decreases with the frequency of the transition. Higher transition frequencies offer the potential for a lower frequency uncertainty up to 5 orders of magnitude for optical transitions compared to microwave transitions.

50 years after the last redefinition of the second, new atomic frequency standards based on optical transitions in various atomic species have been developed that surpass the best caesium atomic clocks in terms of accuracy and precision significantly. Cold caesium fountain clocks reach a systematic frequency uncertainty of 1 to  $2 \times 10^{-16}$  (Guaena et al., 2012; Heavner et al., 2014), whereas for optical clocks relative systematic frequency uncertainties as low as a few  $10^{-18}$  have been reported, e. g.  $2.1 \times 10^{-18}$  for a  $^{87}\text{Sr}$  lattice clock (Nicholson et al., 2015) and  $3 \times 10^{-18}$  for a  $^{171}\text{Yb}$  single-ion clock (Huntemann et al., 2016). The frequency instabilities are  $3 \times 10^{-15}$  for cold single-ion clocks and  $3 \times 10^{-16}$  for lattice clocks at an averaging time  $\tau$  of one second and decrease with  $\tau^{-1/2}$ .

Many optical clock species have been accepted as secondary representations of the second by the Consultative Committee on Time and Frequency and a redefinition of the second based on an optical transition is discussed (Gill, 2016). The direct comparison of optical clocks developed at various NMIs is an important step for the validation of their uncertainty budgets and to find the best candidates for a new definition.

GPS time and frequency transfer allows to compare atomic frequency standards from regional to intercontinental distances and plays an important role in the steering of the International Atomic Time (TAI). TAI is a time scale calculated by the Bureau International des Poids et Mesures (BIPM) based on 400 atomic clocks distributed in over 50 laboratories around the world (Panfilo et al., 2010). As the atomic clocks become more and more stable and accurate, reaching accuracies in

the low  $10^{-18}$  range, the standard microwave time and frequency transfer techniques, Two-Way Satellite Time and Frequency Transfer (TWSTFT) and GPS time and frequency transfer, reaching an instability of  $10^{-15}$  at one day averaging time, become a limiting factor in this comparisons.

In recent years, optical fiber links have been developed (Lopez et al., 2012; Predehl et al., 2012) that allow to compare optical clocks without contributing to the uncertainty (Lisdat et al., 2016). Unfortunately not all NMIs are connected via optical fiber link yet and especially for intercontinental baselines the establishment of optical fiber links will pose a challenge. Currently, improved techniques are developed and tested to max out the performance of microwave time and frequency transfer, e.g. broadband TWSTFT (Margolis et al., 2013), carrier-phase TWSTFT (Fujieda et al., 2014), Atomic Clock Ensemble in Space (ACES) MicroWave Link (Cacciapuoti et al., 2011) and improved GPS frequency transfer (Loyer et al., 2012; Petit et al., 2016).

In this work the possibility to compare optical clocks with GPS based time and frequency transfer techniques at the  $10^{-16}$  level will be investigated and demonstrated. The following main topics will be discussed:

- Which GPS time and frequency techniques are suitable for the frequency comparison of optical clocks at this level of precision and accuracy?
- What is the acceptable GPS station hardware instability?
- What is the impact of frequent dead time due to the limited duty cycle of the optical clocks on the statistical uncertainty of the frequency comparison via GPS link?
- How to optimize the data analysis strategy for the remote comparison of optical clocks via GPS link in the presence of frequent dead time?

Two GPS frequency transfer techniques, Precise Point Positioning (PPP) and Integer Precise Point Positioning (IPPP), based on undifferenced dual-frequency carrier-phase and code observations will be investigated. By making use of precise satellite clock and orbit products, these techniques allow the comparison of clocks using an All-in-View (AV) approach, in which all satellites in view are used to determine the clock error of the individual GPS station. In contrast, a CV approach only uses satellites for the determination of the clock error that are in view of both GPS stations. The All-in-View (AV) approach is especially useful for intercontinental baselines with only very few satellites in common view.

In the PPP standard model, the ambiguity of the carrier-phase observation is estimated as a floating number and the code measurements are used to decorrelate the estimated clock error and the floating ambiguity, whereas the decoupled clock model used in IPPP preserves the integer nature of the ambiguity, so that IPPP is in principle a carrier-phase only technique. The different observation models used in PPP and IPPP have important consequences for the attainable accuracy and precision for time and frequency transfer. In chap. 2, the PPP and IPPP techniques and their application to time and frequency transfer will be discussed.

To profit from the improved accuracy and precision of frequency transfer with the IPPP technique, averaging times of longer than one day are necessary, but the continuous operation of optical clocks for several days is still challenging. The effect of dead time on the statistical uncertainty and measures of frequency instability depending on the dominant noise type is discussed in chap. 1. In this chapter measures of frequency instability will be discussed that can be used to characterize noise types that are not commonly encountered in time and frequency metrology, but have recently been observed in stabilized fiber links.

In ch. 3, the hardware instability of GPS stations will be reviewed and PPP and IPPP links on local baselines at PTB and on continental baselines between European NMIs will be compared. To accurately characterize a GPS time and frequency link, the time and frequency reference must not contribute noise to the clock comparison. At NMIs, active hydrogen masers (AHMs) are often used as local flywheel oscillators. They do fulfill this criteria for averaging times of less than one day, but start to dominate the clock comparison via GPS link for longer averaging times.

On local baselines, a common-clock setup can be used, in which the same clock serves as the time and frequency reference for both GPS stations and therefore cancels in the clock comparison. This approach will be used in sec. 3.2 to study local baselines at PTB. On the continental baseline between PTB and LNE-SYRTE a 1415 km long optical fiber link has been established that can serve as the ground truth for the clock comparison via GPS link, due to its superior performance. In sec. 3.4 the results of comparisons between the optical fiber link and PPP and IPPP links between GPS stations at PTB and LNE-SYRTE will be reported.

In ch. 4 finally, frequency comparisons of optical clocks will be performed. Cold single-ion clocks based on the electric quadrupole and octupole transition in the  $^{171}\text{Yb}^+$  ion developed at NPL and PTB will be compared using PPP and IPPP links. A strategy to estimate the various statistical uncertainty contributions and to minimize the total statistical uncertainty in the presence of dead time will be presented.

In this chapter the basics of frequency stability analysis will be introduced. Different measures of frequency stability in the time and Fourier frequency domain and their properties will be discussed.

Important groundwork on this topic was laid in the sixties (e.g. Allan, 1966, Barnes et al., 1971). Rutman, 1978 gives an extensive review of frequency stability characterization including the relation to the  $n$ -th order structure functions (Lindsey et al., 1976).

Of special interest for this work is the estimation of the uncertainty of a weighted mean frequency for different noise types, and the effect of measurement dead time on this uncertainty. The discussion will be based on the „transfer function concept“ that translates between the time domain and the Fourier frequency domain. The transfer function concept, already described in the classic literature (e.g. Rutman, 1974), still lead to new insights about measures of frequency stability in recent years.

In Rubiola, 2005 the transfer function concept is applied to samples counted with a  $\Lambda$ -type frequency counter instead of the classical  $\Pi$ -type counter and in Benkler et al., 2015 and Vernotte et al., 2016 the concept is applied to samples weighted with a linear phase regression weighting.

In Lee et al., 2010 the uncertainty of a weighted mean frequency for a signal with white phase modulation (WPM) is derived and the impact of dead time on this uncertainty is investigated. In this work, this discussion will be extended to other noise types and other measures of stability.

Furthermore, the  $\Lambda$ -weighted sample mean and its variance will be introduced, which allows to profit from the properties of the  $\Lambda$  weighting function in post-processing averaging. The  $\Lambda$  and  $\Pi$  weighting function will be described as members of the same class of weighting functions, the B-spline basis functions, that enable noise discrimination for additional noise types. The properties of the B-spline basis functions will be used to derive the B-spline weighted sample mean, which is a generalization of the  $\Pi$ - and  $\Lambda$ -weighted sample mean.

Additionally, the algorithm by Kasdin et al., 1992 will be discussed that is used in this work for simulations of time series of power-law noise.

## 1.1 Phase and Frequency Noise

The instantaneous output voltage of an oscillator can be written as

$$V(t) = [V_0 + \epsilon(t)] \sin(2\pi\nu_0 t + \varphi(t)), \quad (1)$$

in which  $\nu_0$  and  $V_0$  are the nominal frequency and amplitude respectively, and  $\varphi(t)$  and  $\epsilon(t)$  are the instantaneous phase and amplitude noise. In the following, the amplitude noise  $\epsilon(t)$  is assumed to be sufficiently small. With this, the instantaneous frequency of the signal generator can be defined as:

$$\nu(t) = \nu_0 + \frac{1}{2\pi} \frac{d\varphi(t)}{dt} = \nu_0 + d\nu(t) \quad (2)$$

with the frequency noise  $d\nu(t) = d\varphi(t)/2\pi dt$ .



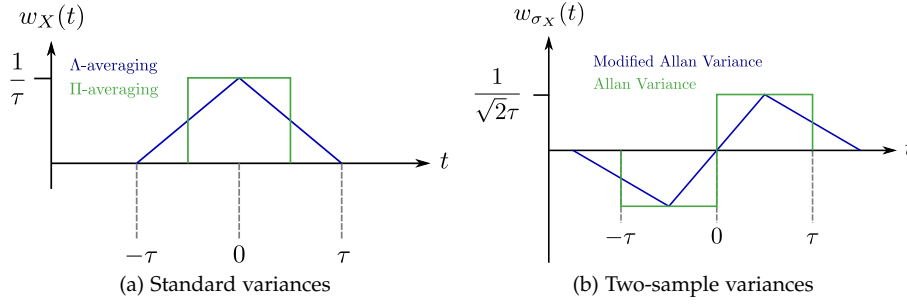


Figure 1: Weighting functions for the standard (a) and two-sample variances (b) for  $\Pi$ - and  $\Lambda$ -averaging.

Another useful parameter is the fractional frequency deviation from the nominal frequency  $\nu_0$ :

$$y(t) = \frac{d\nu(t)}{\nu_0} = \frac{\nu(t)}{\nu_0} - 1 = \frac{1}{2\pi\nu_0} \frac{d\varphi}{dt} = \frac{dx(t)}{dt} \quad (3)$$

with the phase time  $x(t) = \varphi(t)/2\pi\nu_0$ , which is the instantaneous time error of a clock with the instantaneous frequency  $\nu(t)$ . The dimensionless frequency deviation is especially useful for the comparison of oscillators with different nominal frequencies.

## 1.2 Time Domain Stability

In the time domain, the definition of frequency stability is based on the frequency fluctuations that occur over an averaging time interval  $\tau$ , measured with a frequency counter. A continuous measurement without dead time is assumed.

The fractional frequency deviation  $y(t)$  averaged over  $\tau$  beginning at time  $t_k$  (with  $t_{k+j} = t_k + j\tau$ ) can be expressed as the convolution of  $y(t)$  with a generalized weighting function  $w_X(t)$ :

$$\bar{y}_{k,X}(t_k) = \int_{-\infty}^{\infty} y(t)w_X(t - t_k)dt. \quad (4)$$

Often encountered weighting functions in time and frequency metrology are  $\Pi$ -averaging and  $\Lambda$ -averaging.  $\Pi$ -averaging corresponds to a constant weighting function:

$$w_{\Pi}(t) = \begin{cases} 1/\tau, & \text{for } -\tau/2 < t \leq \tau/2, \\ 0, & \text{elsewhere,} \end{cases} \quad (5)$$

and the weighting function for  $\Lambda$ -averaging is triangular:

$$w_{\Lambda}(t) = \begin{cases} (\tau - |t|)/\tau^2, & \text{for } |t| \leq \tau, \\ 0, & \text{elsewhere.} \end{cases} \quad (6)$$

The weighting functions are depicted in fig. 1a. It is noted that in the case of  $\Lambda$ -averaging  $y(t)$  is averaged over  $2\tau$ , it is therefore an overlapping weighting function.

## 1.2.1 Autocovariance and Standard Variance

A measure of frequency stability in the (averaging) time domain is the autocovariance function, which quantifies the covariance between the averaged fractional frequency deviation samples  $\bar{y}_{k,X}$  as a function of the intervening time  $j\tau$  (with lag  $j$ ). It can be expressed as

$$C_{\bar{y},X}(j, \tau) = \langle (\bar{y}_{k+j,X} - \mu)(\bar{y}_{k,X} - \mu) \rangle, \quad (7)$$

with the expectation value  $\mu = \langle \bar{y}_{k,X} \rangle$ .  $\langle a \rangle$  denotes the infinite average of  $a$ . With eq. 4, the autocovariance function can be written as

$$C_{\bar{y},X}(j, \tau) = \left\langle \left[ \int_{-\infty}^{\infty} y(t)w_X(t - t_{k+j})dt - \mu \right] \left[ \int_{-\infty}^{\infty} y(t)w_X(t - t_k)dt - \mu \right] \right\rangle. \quad (8)$$

The standard variance  $s_{\bar{y},X}^2(\tau)$  is a special case of the autocovariance with lag  $j = 0$ :

$$s_{\bar{y},X}^2(\tau) = \langle (\bar{y}_{k,X} - \mu)^2 \rangle = \left\langle \left[ \int_{-\infty}^{\infty} y(t)w_X(t - t_k)dt - \mu \right]^2 \right\rangle. \quad (9)$$

## 1.2.2 Two-sample Variances

A practical measure of frequency stability is the N-sample variance. To enable comparisons between oscillators, the used sample size  $N$  has to be fixed and the averaging time  $\tau$  needs to be specified, because the N-sample variance does not converge for all noise types. The recommended sample size  $N = 2$  leads to the two-sample variances. The generalized two-sample variance  $N = 2$  can be expressed as

$$\sigma_X^2(\tau) = \frac{1}{2} \langle (\bar{y}_{k+1,X} - \bar{y}_{k,X})^2 \rangle = \left\langle \left[ \int_{-\infty}^{\infty} y(t)w_{\sigma_X}(t - t_k)dt \right]^2 \right\rangle, \quad (10)$$

with the generalized two-sample weighting function

$$w_{\sigma_X}(t) = \frac{1}{\sqrt{2}} [w_X(t - \tau/2) - w_X(t + \tau/2)]. \quad (11)$$

For  $\Pi$ -averaged samples this results in the so-called Allan Variance (AVAR) (Allan, 1966):

$$\sigma_A^2(\tau) = \left\langle \left[ \int_{-\infty}^{\infty} y(t)w_{\sigma_A}(t - t_k)dt \right]^2 \right\rangle, \quad (12)$$

with the two-sample weighting function

$$w_{\sigma_A}(t) = \begin{cases} -1/\sqrt{2}\tau, & \text{for } -\tau < t \leq 0, \\ 1/\sqrt{2}\tau, & \text{for } 0 < t \leq 2\tau, \\ 0, & \text{elsewhere.} \end{cases} \quad (13)$$

For  $\Lambda$ -averaged samples, the two-sample variance is the so-called Modified Allan Variance (MVAR) (Allan et al., 1981):

$$\sigma_M^2(\tau) = \left\langle \left[ \int_{-\infty}^{\infty} y(t)w_{\sigma_M}(t - t_k)dt \right]^2 \right\rangle \quad (14)$$

with the two-sample weighting function:

$$w_{\sigma_M}(t) = \begin{cases} -t/\sqrt{2}\tau^2, & \text{for } -3/2\tau < t \leq -1/2\tau, \\ (2t - 3\tau)/\sqrt{2}\tau^2, & \text{for } -1/2\tau < t \leq 1/2\tau, \\ -(t - 2\tau)/\sqrt{2}\tau^2, & \text{for } 1/2\tau < t \leq 3/2\tau, \\ 0, & \text{elsewhere.} \end{cases} \quad (15)$$

The two-sample weighting functions for the AVAR and MVAR are illustrated in fig. 1b.

Another useful quantity is the Time Variance (TVAR)  $\sigma_T^2$  that is used to characterize the time error of a clock, it is defined in relation to the MVAR as

$$\sigma_T^2(\tau) = \frac{\tau^2}{3} \sigma_M^2(\tau). \quad (16)$$

### 1.3 Fourier Frequency Domain Stability

In the Fourier frequency domain, the measure of the frequency stability is the spectral density  $S_y(f)$  of the instantaneous fractional frequency deviations  $y(t)$  with the Fourier frequency  $f$ , not to be confused with the instantaneous frequency  $\nu(t)$  of the oscillator. The spectral density of oscillators can be approximated by a linear combination of five independent power-law noise types (Barnes et al., 1971; Rutman, 1978)

$$S_y(f) = \sum_{\alpha=-2}^2 h_\alpha f^\alpha, \quad (17)$$

with the integer exponent  $\alpha$  and the constant intensities  $h_\alpha$  for corresponding noise types. The five noise types are random walk frequency modulation (RWFM) ( $\alpha = -2$ ), flicker frequency modulation (FFM) ( $\alpha = -1$ ), white frequency modulation (WFM) ( $\alpha = 0$ ), flicker phase modulation (FPM) ( $\alpha = 1$ ), and white phase modulation (WPM) ( $\alpha = 2$ ). The relation between the spectral density of the phase time  $x(t)$  and the spectral density of the fractional frequency deviations  $y(t)$  is given by:

$$S_x(f) = \frac{1}{(2\pi f)^2} S_y(f) = \sum_{\alpha=-2}^2 \frac{h_\alpha}{(2\pi)^2} f^{\alpha-2} = \sum_{\beta=-4}^0 g_\beta f^\beta, \quad (18)$$

with  $\beta = \alpha - 2$  and  $g_\beta = h_\alpha / (2\pi)^2$ . WPM has a constant spectral density of the phase time  $S_x(f) = g_0$ , while WFM has a constant spectral density of the fractional frequency deviations  $S_y(f) = h_0$ . Noise types that do not have a constant spectral density, are called colored noise. In fig. 2 examples of white, flicker and random walk frequency modulations are shown.

#### 1.3.1 Autocovariance and Standard Variance

In the frequency domain, the autocovariance can be expressed as a function of the spectral density  $S_y(f)$  and the Fourier transform of the weighting function  $W_X(f) = \int_{-\infty}^{\infty} \exp(2\pi i f t) w_X(t) dt$  as

$$C_{\bar{y},X}(j, \tau) = \int_0^\infty \cos(2\pi f j \tau) S_y(f) |W_X(f)|^2 df \quad (19)$$

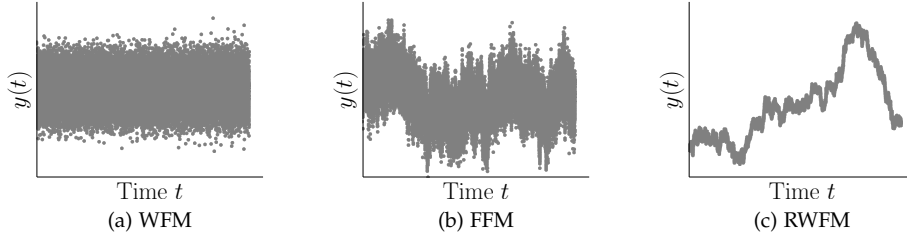


Figure 2: Fractional frequency deviations for power-law noise types: white frequency modulation (WFM) (a), flicker frequency modulation (FFM) (b) and random walk frequency modulation (RWFM) (c). The simulations are based on the algorithm described in sec. 1.8 (Kasdin et al., 1992).

as shown in Benkler et al., 2015 using the Wiener-Khinchin theorem and Parseval's theorem. The standard variance with  $j = 0$  is then given as:

$$s_{\bar{y},X}^2(\tau) = \int_0^\infty S_y(f) |W_X(f)|^2 df \quad (20)$$

with the transfer functions

$$|W_\Pi(f)| = \frac{|\sin(\pi f \tau)|}{\pi f \tau} \text{ for } \Pi\text{-averaging and} \quad (21)$$

$$|W_\Lambda(f)| = \frac{\sin^2(\pi f \tau)}{(\pi f \tau)^2} \text{ for } \Lambda\text{-averaging.} \quad (22)$$

Another useful quantity is the generalized autocorrelation, which is the autocovariance for lag  $j$  divided by the autocovariance for lag  $j = 0$  (standard variance):

$$\rho_{\bar{y},X}(j, \tau) = \frac{C_{\bar{y},X}(j, \tau)}{s_{\bar{y},X}^2(\tau)}. \quad (23)$$

### 1.3.2 Two-sample Variances

Similarly to the standard variance, the generalized two-sample variance (eq. 10) can be expressed using Parseval's theorem as

$$\sigma_X^2(\tau) = \int_0^\infty S_y(f) |W_{\sigma_X}(f)|^2 df, \quad (24)$$

in which the transfer function  $W_{\sigma_X}(f) = \int_{-\infty}^\infty \exp(2\pi i f t) w_{\sigma_X}(t) dt$  is the Fourier transform of  $w_{\sigma_X}(t)$ . This results in

$$\sigma_\Lambda^2(\tau) = \int_0^\infty S_y(f) |W_{\sigma_\Lambda}(f)|^2 df = 2 \int_0^\infty S_y(f) \frac{\sin^4(\pi f \tau)}{(\pi f \tau)^2} df \quad (25)$$

for the AVAR, and

$$\sigma_M^2(\tau) = \int_0^\infty S_y(f) |W_{\sigma_M}(f)|^2 df = 2 \int_0^\infty S_y(f) \frac{\sin^6(\pi f \tau)}{(\pi f \tau)^4} df \quad (26)$$

for the MVAR. This expressions establishes a relationship between the measures of frequency stability in the time and Fourier frequency domain, but it has been shown in Greenhall, 1998 that the mapping between the AVAR and the spectral

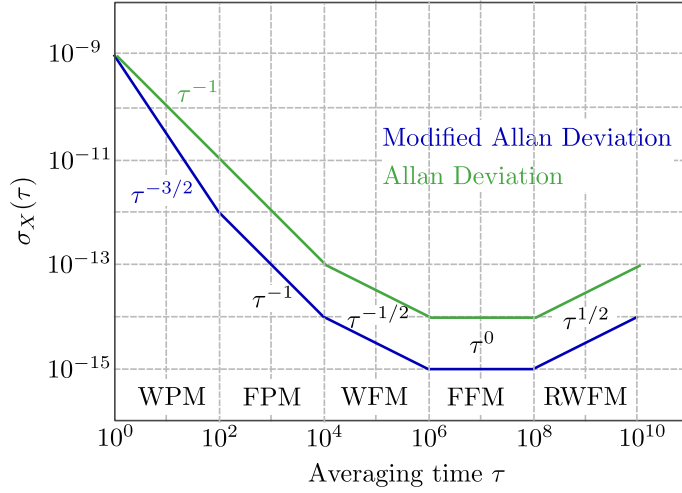


Figure 3: Sigma-tau plot for the ADEV and the MDEV for the five power-law noise types WPM (with  $\mu = -2$  for the ADEV and  $\mu = -3$  for the MDEV), WFM ( $\mu = -2$ ), WFM ( $\mu = -1$ ), FFM ( $\mu = 0$ ), and RWFM ( $\mu = 1$ ).

density is not unique. The two-sample variances can be calculated based on a measured spectral density, but not the other way around.

The AVAR and MVAR as well as the corresponding standard variances for the five power-law noise types are listed in tab. 1. For the calculation of the standard variance in the case of FFM and RWFM a low-frequency cutoff  $f_l$  is necessary, because  $|W_{\Pi,\Lambda}(f)|^2$  tends to 1 for  $f \rightarrow 0$ , whereas for the two-sample variances the additional factor of  $\sin(\pi f \tau)^2 \approx (\pi f \tau)^2$  (Taylor series at  $f = 0$ ) in the integral kernel acts as a high-pass filter that ensures the convergence for noise types with a spectral exponent  $\alpha \geq -2$  (Makdissi et al., 2010). For this reason, the two-sample variances are the preferred measures of frequency stability in the time domain.

For the AVAR a high-frequency cutoff  $f_h$  is necessary for WPM and FPM to ensure convergence of the integral in eq. 25, because the envelope of  $|W_{\sigma_\Lambda}(f)|^2 \propto f^{-2}$  and the integral of  $f^{\alpha-2}$  converges only for  $\alpha \leq 0$  for  $f \rightarrow \infty$ . For the MVAR the additional factor of  $(\pi f \tau)^{-2}$  in the integral kernel of eq. 26 ensures the convergence of the integral for  $\alpha \leq 2$ .

From the eqs. 25 and 26 it is possible to deduce the dependence of the Allan Deviation (ADEV) and Modified Allan Deviation (MDEV) on the averaging time  $\sigma_X \propto \tau^{\mu/2}$  in which  $\mu$  is an integer that depends on the noise type. The  $\tau$ -dependence of the ADEV and MDEV is depicted in fig. 3. It is noted that the MDEV, but not the ADEV, can properly distinguish between WPM and WFM due to the distinct  $\tau$ -dependence.

## 1.4 Conversion between Standard and Two-sample Variances

The two-sample variances are in general biased estimators of the standard variance. The AVAR for example is a biased estimator of the standard variance for all noise types except for WFM.

The Fourier transform of the generalized form of the weighting function  $w_{\sigma_X}(t)$  (eq. 11) is given by:

$$|W_{\sigma_X}(f)| = \sqrt{2} |\sin(\pi f \tau) W_X(f)|. \quad (27)$$

	WPM	FPM	WFM
$S_y(f)$	$h_2 f^2$	$h_1 f$	$h_0$
$\sigma_{\Lambda}^2(\tau)$	$\frac{3f_h}{4\pi^2} h_2 \tau^{-2}$	$\frac{3\ln(2\pi f_h \tau) - \ln(2) + 3\gamma}{4\pi^2} h_1 \tau^{-2}$	$\frac{1}{2} h_0 \tau^{-1}$
$s_{\bar{y},\Pi}^2(\tau)$	$\frac{f_h}{2\pi^2} h_2 \tau^{-2} = \frac{2}{3} \sigma_{\Lambda}^2$	$\frac{\gamma + \ln(2\pi f_h \tau)}{2\pi^2} h_1 \tau^{-2} \approx \frac{2}{3} \sigma_{\Lambda}^2$	$\frac{1}{2} h_0 \tau^{-1} = \sigma_{\Lambda}^2$
$\sigma_M^2(\tau)$	$\frac{3}{8\pi^2} h_2 \tau^{-3}$	$\frac{24\ln(2) - 9\ln(3)}{8\pi^2} h_1 \tau^{-2}$	$\frac{1}{4} h_0$
$s_{\bar{y},\Lambda}^2(\tau)$	$\frac{1}{4\pi^2} h_2 \tau^{-3} = \frac{2}{3} \sigma_M^2$	$\frac{\ln(2)}{\pi^2} h_1 \tau^{-2} \approx 0.82 \sigma_M^2$	$\frac{1}{3} h_0 \tau^{-1} = \frac{4}{3} \sigma_M^2$
	FFM	RWFMM	
	$h_{-1} f^{-1}$	$h_{-2} f^{-2}$	
	$2\ln(2) h_{-1}$	$\frac{2}{3} \pi^2 h_{-2} \tau$	
	$(1.5 - \gamma - \ln(2\pi f_1 \tau)) h_{-1}$	$\left(\frac{1}{f_1} - \frac{\pi^2 \tau}{3}\right) h_{-2}$	
	$2\ln\left(\frac{3 \times 3^{11/16}}{4}\right) h_{-1}$	$\frac{11}{20} \pi^2 h_{-2} \tau$	
	$\left[\frac{25}{12} - \gamma - \frac{4}{3} \ln(2) - \ln(2\pi f_1 \tau)\right] h_{-1}$	$\left(\frac{1}{f_1} - \frac{7\pi^2 \tau}{15}\right) h_{-2}$	

Table 1: Two-sample and standard variances for common noise types for  $\Pi$ - and  $\Lambda$ -weighted averages as a function of the averaging time  $\tau$ . If necessary a high-frequency cut-off  $f_h$  or a low-frequency cutoff  $f_1$  was introduced to ensure convergence with  $2\pi f_h \tau \gg 1$  and  $2\pi f_1 \tau \ll 1$ .  $\gamma$  is the Euler-Mascheroni constant.

Therefore, the generalized form of the two-sample variance (eq. 24) can be written as

$$\begin{aligned}
\sigma_X^2(\tau) &= 2 \int_0^\infty S_y(f) |W_X(f) \sin(\pi f \tau)|^2 df \\
&= \int_0^\infty S_y(f) |W_X(f)|^2 (1 - \cos(2\pi f \tau)) df \\
&= s_{\bar{y},X}^2(\tau) - C_{\bar{y},X}(1, \tau) \\
&= s_{\bar{y},X}^2(\tau) [1 - \rho_{\bar{y},X}(1, \tau)].
\end{aligned} \tag{28}$$

From eq. 28 it can be concluded that the bias of the two-sample variances stems from the autocorrelation of the adjacent weighted fractional frequency deviation samples. Even for uncorrelated WFM, some weighting functions, e. g. the  $\Lambda$ -averaging of the MVAR result in a non-zero autocorrelation term ( $\rho_{\bar{y},\Lambda}(1, \tau) = \frac{1}{4}$ ) and therefore a biased estimate of the standard variance (tab. 1). By calculating the autocorrelation for  $j = 1$  for a given weighting function and noise type the conversion factors between the standard and two-sample variances can be determined. The two-sample and standard variances and their conversion factors for the five power-law noise types are listed in tab. 1.

The knowledge of the conversion factors between the two-sample variances and the corresponding standard variances is a handy tool to estimate statistical uncertainties based on the two-sample variances. In general, the conversion between the standard and two-sample variances depends on the dominant noise type and the averaging method. The averaging method might be chosen depending on the noise type in order to reduce the uncertainty (Benkler et al., 2015; Rubiola, 2005; Vernotte et al., 2016), e. g. for WPM a linear regression weighting will lead to a smaller uncertainty compared to  $\Lambda$ - or  $\Pi$ -averaging, whereas for WFM  $\Pi$ -averaging is the preferred weighting method.

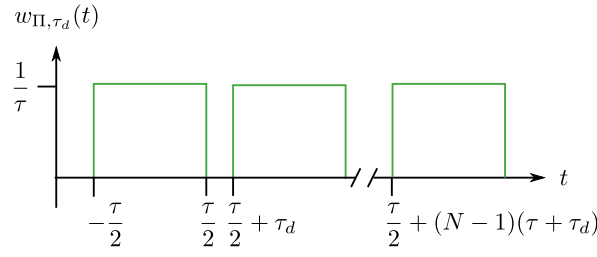


Figure 4: Weighting function  $w_{\Pi, \tau_d}(t)$  for the sample mean with dead time  $\tau_d$  and  $\Pi$ -averaging of the individual samples of length  $\tau$ .

## 1.5 Effect of Dead Time on the Variances

Up to this point a continuous measurement with a frequency counter was assumed, whereas in real world scenarios there will be some dead time inherent to the counter and sometimes even longer dead time due to a deliberately chosen measurement schedule or unexpected failure of equipment.

To study the effect of an arbitrary dead time on the variances, the dead time can be incorporated into the corresponding weighting function  $w_X(t)$ , which might not lead to an analytic solution. To investigate the effect of dead time on the variances depending on the noise type, regularly distributed dead time can be studied.

In Lee et al., 2010 the effect of dead time on the variance of the sample mean in the case of WPM is studied. In the following sections, this discussion will be extended to FPM and additionally the effect of dead time on the AVAR will be studied.

### 1.5.1 Standard Variance with Dead Time

In the following the special case of  $\Pi$ -averaging will be considered. The  $\Pi$  weighting function for the standard variance with regularly distributed dead time  $\tau_d$  can be written as

$$w_{\Pi, \tau_d, N}(t) = \frac{1}{N} \sum_{j=1}^N w_{\Pi}(t - (j-1)(\tau + \tau_d)), \quad (29)$$

and is depicted in fig. 4. The correspondingly weighted fractional frequency deviation

$$\bar{y}_{w, \Pi}(\tau_d, \tau, N) = \frac{1}{N} \sum_{j=1}^N \bar{y}_{k, \Pi}((j-1)(\tau + \tau_d)) \quad (30)$$

can be interpreted as a weighted sample mean with regularly distributed dead time. In Lee et al., 2010 the corresponding variance is calculated using the equation for the variance of the sample mean for autocorrelated data (Witt, 2009; Zhang, 2006). In this work, in the spirit of the derivation of the standard and two-sample variances, the variance of the sample mean will be derived based on its weighting function. This weighting function can then be used for the derivation of the AVAR with regularly distributed dead time.

Making use of the basic properties of the Fourier transform (linearity and time shift), the Fourier transform of  $w_{\Pi, \tau_d}(t)$  (eq. 29) can be written as

$$\begin{aligned} |W_{\Pi, \tau_d, N}(f)| &= \left| \frac{1}{N} \sum_{j=1}^N e^{-i2\pi f(j-1)(\tau + \tau_d)} W_{\Pi}(f) \right| \\ &= |W_{\Pi}(f)| \left| \frac{1}{N} \frac{\sin(N\pi f(\tau + \tau_d))}{\sin(\pi f(\tau + \tau_d))} \right|. \end{aligned} \quad (31)$$

For the calculation of the variance with regularly distributed dead time eq. 31 is inserted into eq. 20 leading to

$$s_{\bar{y}_{w,\Pi}}^2(\tau_d, \tau, N) = \frac{1}{N^2} \int_0^\infty S_y(f) |W_\Pi(f)|^2 \frac{\sin^2(\pi f N(\tau + \tau_d))}{\sin^2(\pi f(\tau + \tau_d))} df. \quad (32)$$

In the case without dead time this reduces to  $s_{\bar{y}_{w,\Pi}}^2(0, \tau, N) = s_{\bar{y},\Pi}^2(N\tau)$ , which results in

$$\begin{aligned} s_{\bar{y}_{w,\Pi}}^2(0, \tau, N) &= \frac{f_h}{2\pi^2} h_2(N\tau)^{-2} = \frac{s_{\bar{y},\Pi}^2(\tau)}{N^2} \text{ (WPM)}, \\ s_{\bar{y}_{w,\Pi}}^2(0, \tau, N) &= \frac{\gamma + \ln(2\pi f_h N\tau)}{2\pi^2} h_1(N\tau)^{-2} \approx \frac{s_{\bar{y},\Pi}^2(\tau)}{N^2} \text{ (FPM)}, \\ s_{\bar{y}_{w,\Pi}}^2(0, \tau, N) &= \frac{1}{2} h_0(N\tau)^{-1} = \frac{s_{\bar{y},\Pi}^2(\tau)}{N} \text{ (WFM)}, \end{aligned} \quad (33)$$

and demonstrates that the uncertainty associated with the  $\Pi$ -weighted mean frequency of a signal dominated by WPM or FPM scales more favorably than the uncertainty of a signal dominated by WFM.

In the case with dead time some approximations are necessary. The Fejér kernel

$$F_N(x) = \frac{1}{N} \frac{\sin^2(Nx)}{\sin^2(x)} = \sum_{|j| \leq N} \left(1 - \frac{|j|}{N}\right) e^{2ijx} = 1 + \frac{2}{N} \sum_{j=1}^{N-1} (N-j) \cos(2xj) \quad (34)$$

can be used to express eq. 32 as

$$\begin{aligned} s_{\bar{y}_{w,\Pi}}^2(\tau_d, \tau, N) &= \frac{1}{N} \int_0^\infty S_y(f) |W_\Pi(f)|^2 df \\ &+ \frac{2}{N^2} \int_0^\infty S_y(f) |W_\Pi(f)|^2 \sum_{j=1}^{N-1} (N-j) \cos(2\pi f j(\tau + \tau_d)) df \\ &= \frac{s_{\bar{y},\Pi}^2(\tau)}{N} + \frac{2}{N^2} \sum_{j=1}^{N-1} (N-j) C_{\bar{y},\Pi}(j, \tau, \tau_d) \\ &= s_{\bar{y},\Pi}^2(\tau) \left[ \frac{1}{N} + \frac{2}{N^2} \sum_{j=1}^{N-1} (N-j) \rho_{\bar{y},\Pi}(j, \tau, \tau_d) \right], \end{aligned} \quad (35)$$

in which  $C_{\bar{y},\Pi}(j, \tau, \tau_d) = \int_0^\infty S_y(f) |W_\Pi(f)|^2 \cos(2\pi f j(\tau + \tau_d)) df$  is the autocovariance function (eq. 19) with dead time and  $\rho_{\bar{y},\Pi}(j, \tau, \tau_d)$  is the autocorrelation (eq. 23) with dead time. The interchange of summation and integration is justified. From this equation it is apparent that the deviation from the  $1/N$  scaling for WPM is due to the autocorrelation of the data.

The autocorrelation with dead time for WPM and  $\Pi$ -averaging can be calculated, assuming  $2\pi f_h \tau \gg 1$ , as:

$$\rho_{\bar{y},\Pi}(j, \tau, \tau_d) = -\frac{1}{2} \frac{\sin(2f_h \pi(\tau(j-1) + j\tau_d))}{2f_h \pi(\tau(j-1) + j\tau_d)} \text{ (WPM)}. \quad (36)$$

For  $2\pi f_h \tau \gg 1$ ,  $\rho_{\bar{y},\Pi}(j, \tau, \tau_d) \approx 0$  for all  $j > 1$ , therefore

$$s_{\bar{y}_{w,\Pi}}^2(\tau_d, \tau, N) = s_{\bar{y},\Pi}^2(\tau) \left[ \frac{1}{N} - \frac{N-1}{N^2} \frac{\sin(2f_h \pi \tau_d)}{2f_h \pi \tau_d} \right] \text{ (WPM)}. \quad (37)$$



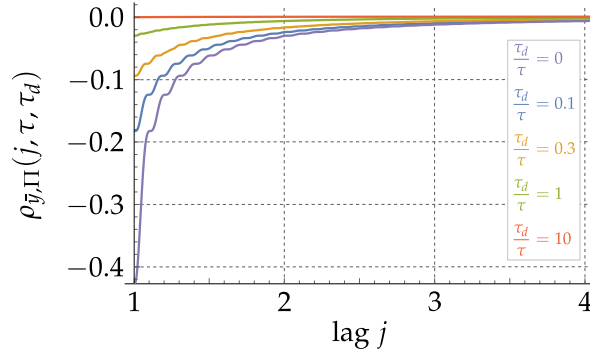


Figure 5: Autocorrelation with dead time for FPM for  $\tau_d/\tau = 0$  (violet),  $\tau_d/\tau = 0.1$  (blue),  $\tau_d/\tau = 0.3$  (orange),  $\tau_d/\tau = 1$  (green), and  $\tau_d/\tau = 10$  (red) (with  $f_h = 1$  and  $\tau = 10$  s).

For  $2f_h\pi\tau_d \gg 1$ , the autocorrelation term vanishes and the variance of the sample mean with dead time scales with  $1/N$  instead of  $1/N^2$ , which is in agreement with results from Lee et al., 2010.

The autocovariance for FPM and  $\Pi$ -averaging is non-zero even for  $j > 1$

$$C_{\bar{y},\Pi}(j, \tau, \tau_d) \cdot \frac{4\pi^2\tau^2}{h_1} = -2(-\text{Ci}(2f_h\pi j(\tau + \tau_d)) + \ln(j[\tau + \tau_d])) \\ - \text{Ci}(2f_h\pi[(j-1)\tau + j\tau_d]) + \ln(j\tau_d + [j-1]\tau) \\ - \text{Ci}(2f_h\pi[(j+1)\tau + j\tau_d]) + \ln(j\tau_d + [j+1]\tau), \quad (38)$$

with the cosine integral  $\text{Ci}(x) = -\int_x^\infty \frac{\cos(t)}{t} dt$ . The  $\text{Ci}(x)$ -terms vanish for  $x \gg 1$ , which is the case for  $2f_h\pi\tau_d \gg 1$ . The remaining logarithmic terms can be rearranged so that with  $2f_h\pi\tau \gg 1$  the autocorrelation can be written as

$$\rho_{\bar{y},\Pi}(j, \tau, \tau_d) \approx \frac{1}{2(\gamma + \ln(2\pi f_h\tau))} \ln\left(1 - \left[j\left(1 + \frac{\tau_d}{\tau}\right)\right]^{-2}\right) \quad (\text{FPM}). \quad (39)$$

Apparently, the autocorrelation with dead time for lag  $j$  depends on the ratio of the dead time  $\tau_d$  and the sample length  $\tau$  as depicted in fig. 5. For  $\tau_d \gg \tau$  the autocorrelation vanishes for all  $j$  and the variance of the sample mean with dead time (eq. 35) scales with  $1/N$  for FPM.

For WFM and  $\Pi$ -averaging the autocorrelation is zero for all  $j$ , so that the dead time does not affect the scaling of the variance of the sample mean.

These are important results that have to be considered when measurements of signals dominated by WPM or FPM are scheduled.

### 1.5.2 Allan Variance (AVAR) with Dead Time

Similarly, the effect of regularly distributed dead time on the two-sample variances can be studied by making use of the two-sample  $\Pi$  weighting function with regularly distributed dead time

$$w_{\sigma_{\Pi,\tau_d,N}}(t) = \frac{1}{\sqrt{2}} [w_{\Pi,\tau_d,N}(t - 1/2(\tau + \tau_d)) - w_{\Pi,\tau_d,N}(t + (N - 1/2)(\tau + \tau_d))], \quad (40)$$

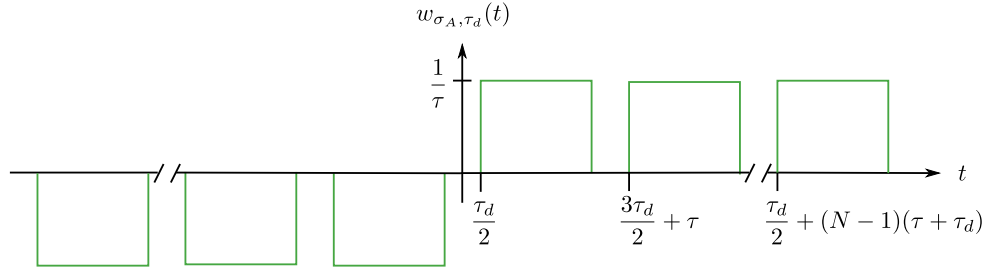


Figure 6: Weighting function  $w_{\sigma_A, \tau_d}(t)$  for the AVAR with regularly distributed dead time  $\tau_d$  between measurements of length  $\tau$ .

and its Fourier transform

$$\begin{aligned} |W_{\Pi, \tau_d}(f)| &= \sqrt{2} |\sin(N\pi f(\tau + \tau_d)) W_{\Pi, \tau_d}(f)| \\ &= \frac{\sqrt{2}}{N} |W_{\Pi}(f)| \frac{\sin^2(N\pi f(\tau + \tau_d))}{|\sin(\pi f(\tau + \tau_d))|}. \end{aligned} \quad (41)$$

For  $N = 1$  this agrees with the results reported in Dawkins et al., 2007. The AVAR with dead time is then given as:

$$\sigma_{\lambda}^2(\tau_d, \tau, N) = \frac{2}{N^2} \int_0^{\infty} S_y(f) |W_{\Pi}(f)|^2 \frac{\sin^4(N\pi f(\tau + \tau_d))}{\sin^2(\pi f(\tau + \tau_d))} df. \quad (42)$$

This reduces to  $\sigma_{\lambda}^2(0, \tau, N) = \sigma_{\lambda}^2(N\tau)$  in the case without dead time  $\tau_d = 0$ , which results in

$$\begin{aligned} \sigma_{\lambda}^2(0, \tau, N) &= \frac{3f_h}{4\pi^2} h_2(N\tau)^{-2} = \frac{\sigma_{\lambda}^2(\tau)}{N^2} \quad (\text{WPM}), \\ \sigma_{\lambda}^2(0, \tau, N) &= \frac{3\ln(2\pi f_h N\tau) - \ln(2) + 3\gamma}{4\pi^2} h_1(N\tau)^{-2} \approx \frac{\sigma_{\lambda}^2(\tau)}{N^2} \quad (\text{FPM}), \\ \sigma_{\lambda}^2(0, \tau, N) &= \frac{1}{2} h_0(N\tau)^{-1} = \frac{\sigma_{\lambda}^2(\tau)}{N} \quad (\text{WFM}). \end{aligned} \quad (43)$$

In the case with dead time, the Fejér kernel equality (eq. 34) is used again to express the AVAR with dead time as:

$$\begin{aligned} \sigma_{\lambda}^2(\tau_d, \tau, N) &= \frac{2}{N} \int_0^{\infty} S_y(f) |W_{\Pi}(f)|^2 \sin^2(N\pi f(\tau + \tau_d)) df \\ &\quad + \frac{4}{N^2} \int_0^{\infty} S_y(f) |W_{\Pi}(f)|^2 \sin^2(N\pi f(\tau + \tau_d)) \sum_{j=1}^{N-1} (N-j) \cos(2\pi f j(\tau + \tau_d)) df \\ &= s_{\bar{y}, \Pi}^2(\tau) \left[ \frac{1}{N} (1 - \rho_{\bar{y}, \Pi}(N, \tau, \tau_d)) \right. \\ &\quad \left. + \frac{1}{N^2} \sum_{j=1}^{N-1} (N-j) (2\rho_{\bar{y}, \Pi}(j, \tau, \tau_d) - \rho_{\bar{y}, \Pi}(N+j, \tau, \tau_d) - \rho_{\bar{y}, \Pi}(N-j, \tau, \tau_d)) \right]. \end{aligned} \quad (44)$$

The AVAR with regularly distributed dead time (eq. 44) for WPM, and  $2f_h\pi\tau \gg 1$  using eq. 36 and  $\rho_{\bar{y}, \Pi}(i, \tau, \tau_d) \approx 0$  for all  $i > 1$  can be expressed as:

$$\sigma_{\lambda}^2(\tau_d, \tau, N) = s_{\bar{y}, \Pi}^2(\tau) \left[ \frac{1}{N} + \frac{1}{N^2} \left( \frac{3}{2} - N \right) \frac{\sin(2\pi f_h \tau_d)}{2\pi f_h \tau_d} \right] \quad (\text{WPM}). \quad (45)$$

	WPM	WFM
$\sigma_{\lambda}^2(0, \tau, N)$	$\frac{\sigma_{\lambda}^2(\tau)}{N^2}$	$\frac{\sigma_{\lambda}^2(\tau)}{N}$
$\sigma_{\lambda}^2(\tau_d, \tau, N)$	$\frac{2\sigma_{\lambda}^2(\tau)}{3N}$	$\frac{\sigma_{\lambda}^2(\tau)}{N}$
$s_{\bar{y}_{w,\Pi}}^2(0, \tau, N)$	$\frac{s_{\bar{y}_{w,\Pi}}^2(\tau)}{N^2} = \frac{2}{3}\sigma_{\lambda}^2(0, \tau, N)$	$\frac{s_{\bar{y}_{w,\Pi}}^2(\tau)}{N} = \sigma_{\lambda}^2(0, \tau, N)$
$s_{\bar{y}_{w,\Pi}}^2(\tau_d, \tau, N)$	$\frac{s_{\bar{y}_{w,\Pi}}^2(\tau)}{N} = \sigma_{\lambda}^2(\tau_d, \tau, N)$	$\frac{s_{\bar{y}_{w,\Pi}}^2(\tau)}{N} = \sigma_{\lambda}^2(\tau_d, \tau, N)$

Table 2: N-scaling for the standard and two-sample variance with  $\Pi$ -averaging for WPM and WFM for  $2f_h\pi\tau_d \gg 1$  and without dead time  $\tau_d = 0$ .

The AVAR with regularly distributed dead time for WPM scales with  $1/N$  instead of  $1/N^2$  and is an unbiased estimator for the variance of the sample mean with dead time for  $2f_h\pi\tau_d \gg 1$ .

Substituting  $\tau^* = N\tau$ , the  $\tau^*$ -dependence of  $\sigma_{\lambda}^2(\tau^*, \tau, \tau_d)$  can be evaluated. For  $2f_h\pi\tau_d \gg 1$  and  $\tau^* \gg \tau$  the ADEV with dead time is  $\sigma_{\lambda}(\tau^*, \tau, \tau_d) \propto \sqrt{\tau/\tau^*}$ . Regularly distributed dead time changes the slope in the double-logarithmic sigma-tau plot as demonstrated in fig. 7 for WPM, potentially leading to a misidentification of the noise type. A similar change of the slope of the ADEV with regularly distributed dead time in the sigma-tau plot can be observed for FPM, but in general the autocovariance with dead time (eq. 38) and therefore the ADEV with dead time (eq. 44) depends on the ratio of the dead time  $\tau_d$  and the sample length  $\tau$ . If the

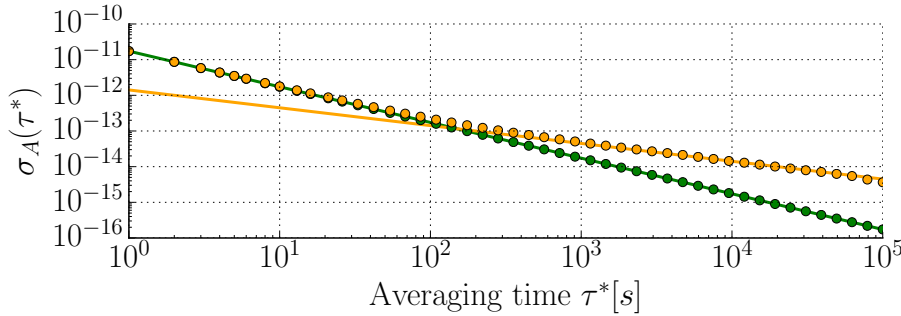


Figure 7: Effect of regularly distributed dead time on the ADEV for WPM. Plotted is the ADEV over  $\tau^* = N\tau$  for a simulated data set without dead time (green dots) and with dead time (orange dots) with  $\tau = 100\text{s}$  and  $\tau_d = 1\text{s}$ , the solid orange line was calculated using eq. 45. For  $\tau^* \gg \tau$  the slope in the simulated data set with dead time changes from  $-1$  to  $-1/2$ . The simulation is based on the algorithm described in sec. 1.8 (Kasdin et al., 1992).

purpose of the AVAR calculations is not to estimate the variance of the sample mean, but to characterize the noise types of an oscillator, strategies have to be applied to circumvent this problem. For this purpose, dead time resistant algorithms for the estimation of the ADEV can be used (e. g. Sesia et al., 2008).

Tab. 2 summarizes the findings about the N-scaling of the AVAR and the variance of the sample mean with and without dead time.

The equations of the variance of the  $\Pi$ -weighted sample mean with dead time (eq. 35) and the AVAR with regularly distributed dead time (eq. 44) for  $\Pi$ -averaged samples can easily be generalized to samples averaged with other weighting func-

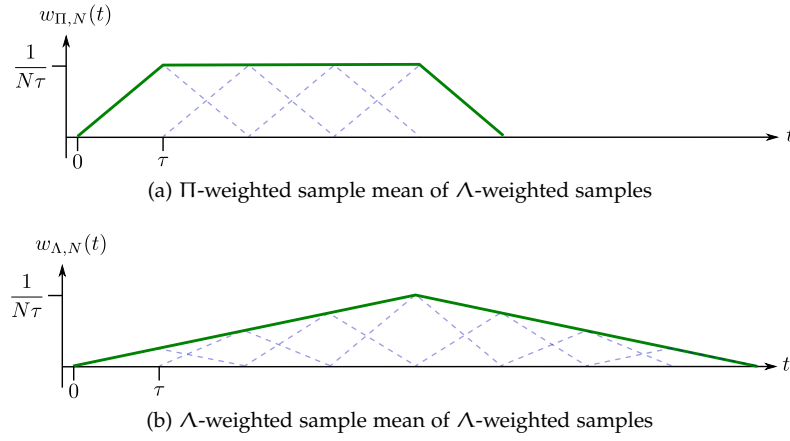


Figure 8: Weighting function for the  $\Pi$ -weighted sample mean (a) and the  $\Lambda$ -weighted sample mean (b) of  $\Lambda$ -averaged samples described in eq. 6 for  $N = 4$ . The blue dashed line represents the weighted individual overlapping  $\Lambda$ -averaged samples.

tions, by replacing  $W_{\Pi}(f)$  with  $W_{\chi}(f)$ . In the case of dead time and with overlapping weighting functions special attention has to be paid to the interaction of the dead time and the overlap of the weighting function depending on the actual implementation.

### 1.6 $\Lambda$ -Weighted Sample Mean and its Variance

In the previous section the  $\Pi$ -weighted sample mean of  $\Pi$ -averaged samples was considered (eq. 30). If fractional frequency differences have been recorded with a  $\Lambda$ -counter and are subsequently  $\Pi$ -averaged, the resulting weighting function for the variance of the sample mean does not resemble a  $\Lambda$  weighting function, but a trapezoidal weighting function instead that approximates a  $\Pi$  weighting function for large  $N$  (Rubiola, 2005) as shown in fig. 8a. The corresponding variance of the sample mean scales with  $1/N^2$  for WPM (Benkler et al., 2015), the standard variance with  $\Lambda$ -averaging on the other hand scales with  $1/\tau^3$  (tab. 1).

In order to preserve the statistical properties of the  $\Lambda$ -averaging in post processing averaging a strategy of „numerically increasing“ the  $\Lambda$ -averaging interval was applied in Raupach et al., 2015 and in Rubiola et al., 2016, a recursive formula for the decimation of  $\Lambda$ -averaged samples is introduced. In the following, a non-recursive formulation of the  $\Lambda$ -weighted sample mean will be given and the transfer function concept will then be used to proof the validity of this concept by showing that the statistical properties of the corresponding variance are in fact preserved. The weighting function for a  $\Lambda$ -weighted sample mean

$$w_{\Lambda,N}(\tau) = \frac{1}{N} \sum_{j=1}^{2N-1} \left(1 - \frac{|j-N|}{N}\right) w_{\chi}(t-j\tau) \quad (46)$$

is depicted in fig. 8b for  $N = 4$  and  $\Lambda$ -averaged samples. In order to imitate the overlapping nature of the  $\Lambda$ -averaging, eq. 46 averages over  $2N - 1$  samples. The  $\Lambda$ -weighted sample mean without dead time is

$$\bar{y}_{w,\Lambda}(\tau, N) = \frac{1}{N} \sum_{j=1}^{2N-1} \left(1 - \frac{|j-N|}{N}\right) \bar{y}_{k,\chi}(j\tau). \quad (47)$$

The corresponding transfer function using the basic properties of the Fourier transform and the Fejér identity (eq. 34) can be expressed as

$$\begin{aligned} |W_{\Lambda, N}(f)| &= \left| \frac{1}{N} \sum_{|j| \leq N} \left(1 - \frac{|j|}{N}\right) e^{-i2\pi f j \tau} W_X(f) \right| \\ &= |W_X(f)| \frac{1}{N^2} \frac{\sin^2(N\pi f \tau)}{\sin^2(\pi f \tau)}. \end{aligned} \quad (48)$$

The variance of the  $\Lambda$ -weighted sample mean is

$$s_{\bar{y}_{w, \Lambda}}^2(\tau, N) = \frac{1}{N^4} \int_0^\infty S_y(f) |W_X(f)|^2 \frac{\sin^4(N\pi f \tau)}{\sin^4(\pi f \tau)} df. \quad (49)$$

For  $\Lambda$ -averaged samples this reduces to  $s_{\bar{y}_{w, \Lambda}}^2(\tau, N) = s_{\bar{y}_{k, \Lambda}}^2(N\tau)$  and therefore

$$s_{\bar{y}_{w, \Lambda}}^2(\tau, N) = \frac{1}{4\pi^2} h_2(N\tau)^{-3} = \frac{s_{\bar{y}_{k, \Lambda}}^2(\tau)}{N^3} \text{ (WPM)}. \quad (50)$$

This shows that the  $\Lambda$ -weighted sample mean (eq. 47) leads to the desired  $N$ -scaling of the corresponding variance of the sample mean. In fig. 9 the  $N$ -dependence of the deviation of  $\Lambda$ -weighted and the  $\Pi$ -weighted sample mean for  $\Lambda$ -averaged samples is shown based on a Monte Carlo simulation (Kasdin et al., 1992) of WPM, which confirms the above calculations. The variance of the  $\Lambda$ -weighted sam-

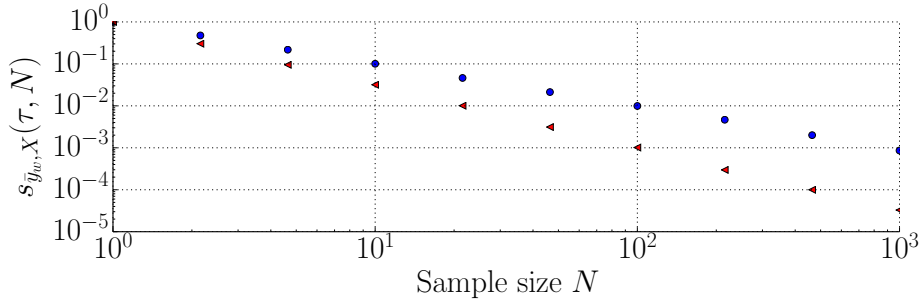


Figure 9:  $N$ -dependence of the  $\Lambda$ -weighted deviation of the sample mean (red triangles)  $\bar{y}_{w, \Lambda}(\tau, N)$  and the  $\Pi$ -weighted deviation of the sample mean  $\bar{y}_{w, \Pi}(\tau, N)$  (blue dots) for  $\Lambda$ -averaged samples based on Monte Carlo simulations of WPM using the algorithm by Kasdin et al., 1992.

ple mean can be expressed in terms of the autocorrelation function of the individual samples by using the Fourier series representation of the Jackson kernel  $\frac{\sin^4(Nx)}{\sin^4(x)} = \sum_{|j| \leq N} a(j) \exp(2ijx)$  with

$$a(j) = \begin{cases} N(2N^2 + 1)/3 - \frac{1}{2}(|j| + 2Nj^2 - |j|^3), & \text{for } |j/n| \leq 1 \\ \frac{1}{6}(2N - |j|) [(2N - |j|)^2 - 1], & \text{for } 1 \leq |j/n| \leq 2 \end{cases} \quad (51)$$

leading to

$$\begin{aligned}
s_{\bar{y}_{w,\Lambda}}^2(\tau, N) = s_{\bar{y},X}^2(\tau) & \left[ \frac{1 + 2N^2}{3N^3} \right. \\
& + \frac{1}{3N^4} \sum_{j=1}^{N-1} \left[ 2(2N^2 + 1)N - 3j(1 + j(2N - j)) \right] \rho_{\bar{y},X}(j, \tau) \\
& \left. + \frac{1}{3N^4} \sum_{j=N+1}^{2N-1} (2N - j) \left[ (2N - j)^2 - 1 \right] \rho_{\bar{y},X}(j, \tau) \right].
\end{aligned} \tag{52}$$

This expression can be used to calculate the variance of the  $\Lambda$ -weighted sample mean for all types of weighted samples, e. g.  $\Pi$ -averaged samples. For WPM the autocorrelation is zero for all  $j > 1$  and  $\rho_{\bar{y},\Lambda}(1, \tau) = \rho_{\bar{y},\Pi}(1, \tau) = -1/2$  for  $\Lambda$ - and for  $\Pi$ -averaging. Therefore, the variance of the  $\Lambda$ -weighted sample mean scales with  $1/N^3$  for WPM for both  $\Lambda$ - and  $\Pi$ -averaged samples, which means that even if the samples have been counted with a  $\Pi$ -counter, one can profit from the  $1/N^3$  scaling in post processing by using the  $\Lambda$ -weighted sample mean.

## 1.7 Discrimination of Additional Power-Law Noise Types

The standard noise model with five power-law noise types does not always describe the observed noise in time and frequency metrology, e. g. in Calonico et al., 2014; Droste et al., 2013 power-law noise with  $\alpha \geq 3$  was observed. While the MVAR can discriminate power-law noise types up to  $\alpha = 2$ , the discrimination power gets lost for larger spectral exponents and  $\sigma_M^2 \propto \tau^{-4}$  for all  $\alpha \geq 3$ .

In Vernotte et al., 2000 the  $n$ -th difference structure functions (Lindsey et al., 1976) are generalized to families with different smoothness. The noise discrimination power depends on the smoothness of the weighting function, higher smoothness results in a discrimination power for higher spectral exponents. In the following, the  $n$ -th difference structure functions of smoothness  $k$  will be described in terms of wavelets with a B-spline basis and the properties of the B-spline basis functions will be used to derive the B-spline weighted sample mean, a generalization of the  $\Pi$ - and  $\Lambda$ -weighted sample mean.

### 1.7.1 B-spline Basis Functions and Wavelets

The rectangular weighting function ( $\Pi$ -averaging) and the triangular weighting function ( $\Lambda$ -averaging) belong to the same class of weighting functions, based on the B-spline basis functions (Schoenberg, 1946), which are the  $k$ -fold self-convolutions of the rectangular window  $\beta_0(t)$

$$\beta_k(t) = \underbrace{(\beta_0 * \beta_0 * \dots * \beta_0)}_{(k+1)\text{-times}}(t) \tag{53}$$

with

$$\beta_0(t) = \begin{cases} 1, & \text{for } -1/2 < t \leq 1/2, \\ 0, & \text{elsewhere.} \end{cases} \tag{54}$$

The B-splines converge to the Gaussian function for large  $k$  (Unser et al., 1992). The weighting functions for the standard variance can be expressed as

$$w_k(t) = \frac{1}{\tau} \beta_k\left(\frac{t}{\tau}\right) \tag{55}$$

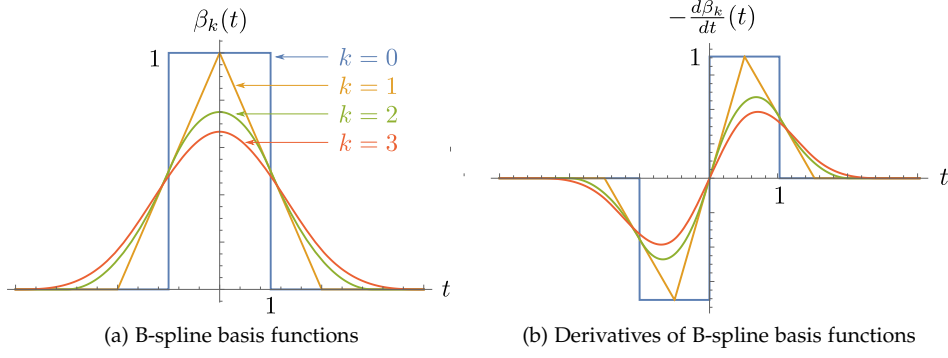


Figure 10: B-spline basis functions for  $k = \{0, \dots, 3\}$  (a) and first order derivatives (b).

with  $k = 0$  for  $\Pi$ -averaging and  $k = 1$  for  $\Lambda$ -averaging.

The corresponding transfer functions are  $|W_k(f)| = |\text{sinc}^{k+1}(\pi f \tau)| \propto |\pi f \tau|^{-k-1}$ . The two-sample variance for the  $k$ -th order B-spline weighting function is

$$\sigma_k^2(\tau) \propto \int_0^\infty f^\alpha \frac{\sin^{2k+4}(\pi f \tau)}{(\pi f \tau)^{2k+2}} df \propto \frac{1}{(\pi \tau)^{\alpha+1}} \int_0^\infty u^{\alpha-2k-2} \sin^{2k+4}(u) du, \quad (56)$$

in which  $u = \pi f \tau$  is substituted. The two-sample variance is  $\propto \tau^{-\alpha-1}$ , and therefore able to discriminate properly between different  $\alpha$ , as long as the integral converges, which is the case for  $\alpha - 2k - 2 \leq -2$ . For every  $\alpha$  a minimum  $k$ -th order  $k_{\min} = \lceil \alpha/2 \rceil$  can be determined that is necessary to discriminate the corresponding noise type from  $\alpha + 1$ . In fig. 10 the B-spline weighting functions and the

	$\alpha = 6$	$\alpha = 5$	$\alpha = 4$	$\alpha = 3$	WPM	FPM	WFM	FFM	RWFM
$S_y(f)$	$h_6 f^6$	$h_5 f^5$	$h_4 f^4$	$h_3 f^3$	$h_2 f^2$	$h_1 f$	$h_0$	$h_{-1} f^{-1}$	$h_{-2} f^{-2}$
$k = 0$	$\tau^{-2}$	$\tau^{-2}$	$\tau^{-2}$	$\tau^{-2}$	$\tau^{-2}$	$\tau^{-2}$	$\tau^{-1}$	$\tau^0$	$\tau^1$
$k = 1$	$\tau^{-4}$	$\tau^{-4}$	$\tau^{-4}$	$\tau^{-4}$	$\tau^{-3}$	$\tau^{-2}$	$\tau^{-1}$	$\tau^0$	$\tau^1$
$k = 2$	$\tau^{-6}$	$\tau^{-6}$	$\tau^{-5}$	$\tau^{-4}$	$\tau^{-3}$	$\tau^{-2}$	$\tau^{-1}$	$\tau^0$	$\tau^1$
$k = 3$	$\tau^{-7}$	$\tau^{-6}$	$\tau^{-5}$	$\tau^{-4}$	$\tau^{-3}$	$\tau^{-2}$	$\tau^{-1}$	$\tau^0$	$\tau^1$

Table 3: Dependence of the two-sample variance for  $k$ -th order B-spline weighting functions on  $\tau$  depending on the noise type for  $k = \{0, \dots, 3\}$  ( $\ln(\tau)$ -terms are omitted for simplicity.).

corresponding two-sample weighting functions are plotted for  $k = \{0, \dots, 3\}$  and in tab. 3 the  $\tau$ -dependence of the two-sample variances  $\sigma_k^2(\tau)$  are summarized for noise types with  $\alpha \leq 6$ . For the  $k$ -th order B-spline, the averaging time is  $(k + 1)\tau$  so that the area under the weighting function equals one. The increased discrimination power comes at the prize of longer measurement times. Interestingly, the  $k$ -th order two-sample weighting function is the negative first derivative of the B-spline with order  $k + 1$

$$w_{\sigma_k}(t) = \frac{1}{c_k} (w_k(t - \tau/2) - w_k(t + \tau/2)) = -\frac{1}{c_k} \frac{dw_{k+1}(t)}{dt} \quad (57)$$

in which  $c_k$  is usually set to  $\sqrt{2}$ , which was chosen to ensure that the AVAR is an unbiased estimator for the standard variance for WFM and  $\Pi$ -averaging. For other  $k$  a different factor has to be chosen to ensure an unbiased estimate, e. g. for  $k = 1$  ( $\Lambda$ -averaging):  $c_1 = \sqrt{3/2}$ .

This B-spline two-sample weighting functions are the first order difference structure functions of the families with different 'smoothness' qualitatively described in Vernotte et al., 2000. The higher order  $n$ -th difference structure functions (Lindsey et al., 1976; Makdissi et al., 2010; Vernotte et al., 2000) can be expressed as

$$w_{\sigma_{k,n}}(t) = -\frac{1}{c_{k,n}} \frac{d^n w_{k+n}(t)}{d^n t} = -\frac{1}{c_{k,n}} \sum_{j=0}^n (-1)^j \binom{n}{j} w_k(t - j\tau) \quad (58)$$

The  $n$ -th derivative of  $w_{k,n}$  corresponds to a  $(n + 1)$ -sample variance. The set of the  $n$ -th derivatives of  $w_{k+n}$  have the same smoothness and discrimination properties for high frequency noise for constant  $k$ . In fig. 11 higher order differences up to  $n = 3$  are depicted for  $k = \{0, \dots, 2\}$ . A well-known example of a three-sample

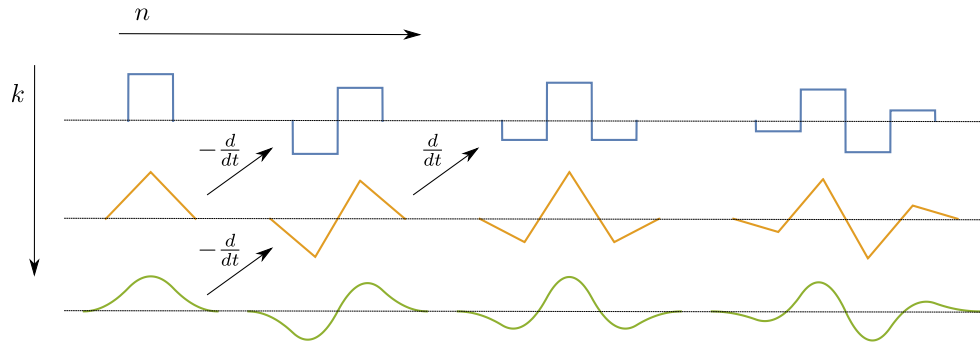


Figure 11: Weighting functions  $w_{\sigma_{k,n}}$  with  $n$ -th order differences of smoothness  $k$  and their relationship described by  $n$ -th order derivatives.

variance is the Hadamard variance with  $k = 0$  (Baugh, 1971).

The Fourier transform for the  $(n + 1)$ -sample variance

$$|W_{\sigma_{k,n}}| = \frac{1}{c_{k,n}} |(2\pi f\tau)^n \text{sinc}^{k+n+1}(\pi f\tau)| = \frac{2^n}{c_{k,n}} |\sin^n(\pi f\tau) \text{sinc}^{k+1}(\pi f\tau)|. \quad (59)$$

For  $k = 0$  this agrees with the filter variance described in Makdissi et al., 2010. The variances of higher order derivatives have the advantage of converging for low frequency noise from  $f^{-2n}$  and of being insensitive to phase drifts up to order  $n$  (Lindsey et al., 1976; Makdissi et al., 2010; Vernotte et al., 2000). The two parameters  $k$  and  $n$  can now be chosen independently to determine a weighting function with the desired convergence properties for high as well as low frequency noise. The parameter  $k$  determines the order of the low-pass filter and the parameter  $n$  the order of the high-pass filter.

The  $(n + 1)$ -sample variances can be normalized using the same criteria as for the two-sample variances. To ensure that the  $(n + 1)$ -sample variance leads to an unbiased estimate of the corresponding standard variance with the same  $k$  for WFM, the following equation must be fulfilled

$$\frac{2^{2n}}{c_{k,n}^2} \int_0^\infty \frac{\sin^{2(n+k+1)}(\pi f\tau)}{(\pi f\tau)^{2(k+1)}} df = \int_0^\infty \text{sinc}^{2(k+1)}(\pi f\tau) df. \quad (60)$$



The integral on the left side can be written as an analytic expression (Weissstein, 2017)

$$\begin{aligned} f(k, n) &= \int_0^\infty \frac{\sin^{2(n+k+1)}(\pi x)}{(\pi x)^{2(k+1)}} dx \\ &= \frac{(-1)^{n+4-k-1-n}}{\Gamma(2+2k)} \sum_{j=0}^{k+1+n} (-1)^j \binom{2+2k+2n}{j} (2-2j+2k+2n)^{1+2k+2n}. \end{aligned} \quad (61)$$

The coefficients can then be calculated with  $c_{n,k}^2 = 2^{2n} f(k, n) / f(k, 0)$ . This leads to  $c_{0,n}^2 = \binom{2n}{n}$  for  $k = 0$  and  $c_{1,n}^2 = \frac{2+n}{2+2n} \binom{2n}{n}$  for  $k = 1$ .

The  $(n+1)$ -sample weighting functions of smoothness  $k$  can be understood as wavelets with a B-spline basis. Wavelet theory has been used before (Percival et al., 2006) to describe the AVAR as a wavelet variance of the Haar wavelet, which is the first derivative of the 1st order B-spline or the lowest order Daubechies wavelet (Daubechies, 1992). The application of higher order Daubechies wavelets for frequency stability analysis has been studied e. g. in Howe et al., 1994; Percival, 2016.

### 1.7.2 Parzen Weighting Function

An example of a weighting function with increased discrimination power is the Parzen window (Harris, 1978) with  $k = 3$ , which can discriminate power-law noise up to  $\alpha = 6$ :

$$w_{\text{Parzen}}(t) = \begin{cases} \frac{2}{3\tau} \left( 1 - 6 \left( \frac{|t|}{2\tau} \right)^2 + 6 \left( \frac{|t|}{2\tau} \right)^3 \right) & 0 \leq |t| \leq \tau \\ \frac{2}{3\tau} \left( 1 - \frac{|t|}{2\tau} \right)^3 & \tau < |t| \leq 2\tau. \end{cases} \quad (62)$$

The corresponding Fourier transform is

$$|W_{\text{Parzen}}(f)| = \text{sinc}^4(\pi f \tau). \quad (63)$$

In fig. 12 the sigma-tau plot for the two-sample variance with  $k = 3$  is plotted for

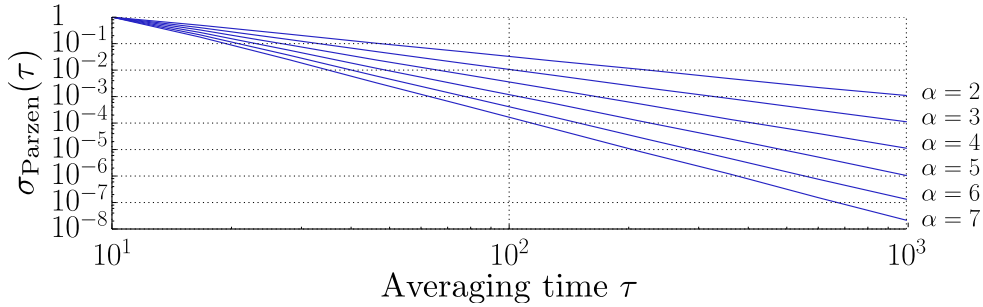


Figure 12: Dependence of the two-sample variance for the  $k = 3$  B-spline weighting function on  $\tau$  for noise types with  $\alpha = \{2, \dots, 7\}$  demonstrated based on simulated power-law noise (Kasdin et al., 1992).

noise types from  $\alpha = \{2, \dots, 7\}$  based on simulated power-law noise (Kasdin et al., 1992). The results agree with the calculations reported in tab. 3.

## 1.7.3 B-spline Weighted Sample Mean

An interesting property of the B-splines is the two-scale relation that states that the B-spline of order  $k$  can be expressed as a linear combination of  $k + 1$  scaled and time shifted B-splines of order  $k$ . This property is relevant for the decimation of samples weighted with a B-spline basis function as discussed in sec. 1.6 for  $\Lambda$ -averaged samples. The two-scale relation for B-spline basis functions is given as (Rioul et al., 1992):

$$\beta_k(t) = \sum_{j=0}^{k+1} 2^{-k} \binom{k+1}{j} \beta_k(2t - j), \quad (64)$$

and therefore

$$w_k(t/2) = \sum_{j=0}^{k+1} 2^{-k-1} \binom{k+1}{j} w_k(t - j\tau). \quad (65)$$

This equation can be used recursively to decimate samples weighted with a  $k$ -th order B-spline basis function. In fig. 13 the two-scale relation is demonstrated for the Parzen window.

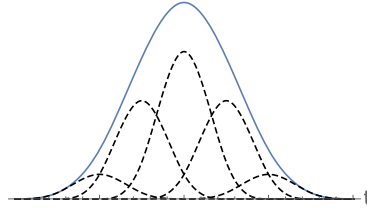


Figure 13: Demonstration of the two-scale relation for the 3rd order B-spline (Parzen window). The blue solid line represents a linear combination (eq. 64) of the scaled 3rd order B-splines depicted as black dashed lines.

The generalization of the two-scale relation, the  $N$ -scale relation is given as (Unser et al., 1994):

$$\beta_k(t/N) = \sum_{j \in \mathbb{Z}} h_N^k(j) \beta_k(t - j), \quad (66)$$

and therefore

$$w_k(t/N) = \frac{1}{N} \sum_{j \in \mathbb{Z}} h_N^k(j) w_k(t - j\tau), \quad (67)$$

with the  $Z$ -transform of the sequence  $h_N^k(j)$

$$H_N^k(z) = \frac{1}{N^k} \left( \sum_{j=0}^{N-1} z^{-j} \right)^{k+1}. \quad (68)$$

The Fourier transform of the  $k$ -th order B-spline sample mean weighting function  $w_{k,N}(t) = w_k(t/N)$

$$|W_{k,N}| = \left( \frac{1}{N} \frac{\sin(N\pi f\tau)}{\sin(\pi f\tau)} \right)^{k+1} |W_k(f)|. \quad (69)$$

For  $k = 0$  this agrees with eq. 31 and for  $k = 1$  with eq. 48. It can be concluded that for all B-spline weighting functions the statistical properties of the averaging

method are preserved, if the  $k$ -th order B-spline sample mean is formed on  $k$ -th order B-spline weighted samples.

## 1.8 Noise Simulation

In this work power-law noise simulations are performed using the algorithm from Kasdin et al., 1992. The algorithm is based on the convolution of a discrete time series with white noise  $w_k$  and the noise type dependent pulse response coefficients  $h_k$ . In the discrete case:

$$x_k = \sum_{l=0}^{k-1} h_{k-l} w_l. \quad (70)$$

Instead of a direct convolution in the time domain, the algorithm performs a multiplication in the Fourier domain. The Fourier transform of  $w_k$  is multiplied with the Fourier transform of  $h_k$  and then an inverse Fourier transform of this product leads to a time series  $x_k$  with the desired noise type.

The coefficients  $h_k$  are chosen based on a generalized discrete transfer function:

$$H(z) = (1 - z^{-1})^{\beta/2}, \quad (71)$$

in which  $\beta$  is the integer value defining the noise type in the phase time spectral density  $S_x(f)$  (eq. 18). The corresponding impulse response coefficients can be calculated based on the recursive relation:

$$h_k = (k - 1 - \beta/2) \frac{h_{k-1}}{k}. \quad (72)$$

The relation between the variance of the white noise time series  $s_w^2$  and the spectral intensity  $g_\beta$  is given by:

$$s_w^2 = \frac{g_\beta}{2(2\pi)^\beta \tau_0^{\beta+1}}. \quad (73)$$

The spectral intensities  $g_\beta$ , together with the equations from tab. 1 can be used to relate the two-sample variances with the simulation input parameter  $s_w^2$ . Fig. 14 shows the spectral density and MDEV for simulated power-law noise for  $\beta = -4$  to  $0$  and the calculated predictions. The simulation agrees well with the predictions. The Python (Python Software Foundation, <http://www.python.org>) implementation of this algorithm used in this work is available online (Leute et al., 2017).

## 1.9 Summary

The spectral density of oscillator noise can be expressed as a linear combination of five independent power-law noise types: white phase modulation (WPM), flicker phase modulation (FPM), white frequency modulation (WFM), flicker frequency modulation (FFM) and random walk frequency modulation (RWFM) with spectral exponents from  $\alpha = 2$  to  $-2$ . Two-sample variances, for example the Allan Variance (AVAR) and Modified Allan Variance (MVAR), are the preferred measures of frequency stability in the time domain, due to their convergence for noise types with spectral exponent  $\alpha \leq 0$ . The Modified Allan Deviation (MDEV) has the advantage over the Allan Deviation (ADEV) of being able to discriminate properly between WPM and FPM.

In general, the two-sample variances are biased estimators of the standard variance, due to the autocorrelation of adjacent weighted fractional frequency deviations. The uncertainty of a frequency measurement can still be estimated based

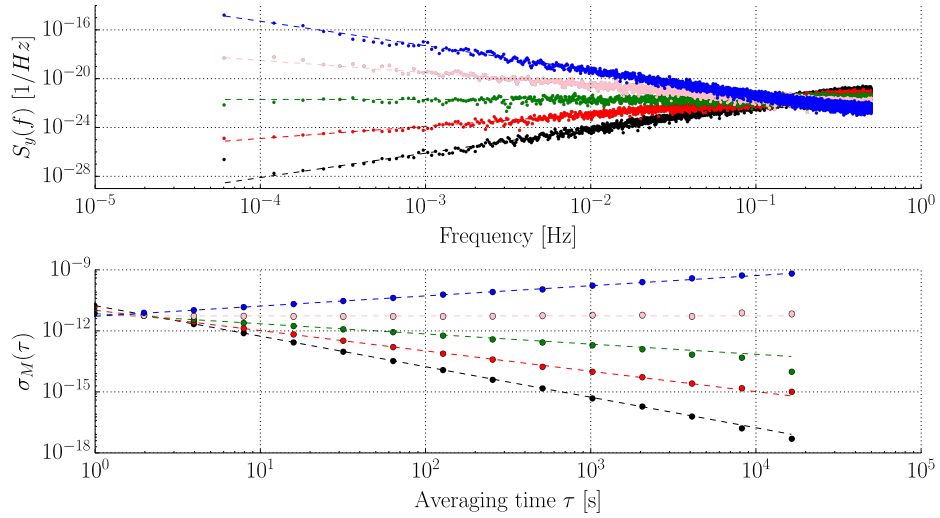


Figure 14: Spectral density  $S_y(f)$  and MDEV  $\sigma_M(\tau)$  for simulated power-law noise types: WPM (black), FPM (red), WFM (green), FFM (pink) and RWFM (blue) using the algorithm from Kasdin et al., 1992. The dashed lines are calculated using the eqs. from tab. 1 and eq. 73.

on the corresponding two-sample variance, if conversion factors depending on the noise type and the weighting of the fractional frequency deviations are taken into account. The weighting method might be chosen depending on the dominant noise type, in order to optimize the uncertainty of the frequency measurement.

The scaling with the sample size  $N$  for the variance of the sample mean and the AVAR is different for WPM, FPM and WFM. The variance of the sample mean and the AVAR scale with  $1/N^2$  for WPM and FPM, and with  $1/N$  for WFM, due to the autocorrelation of the samples for WPM and FPM. The variance of the sample mean and the AVAR with regularly distributed dead time was derived and it was demonstrated that the autocorrelation of WPM and FPM can vanish due to regularly distributed dead time leading to a  $1/N$  scaling of the variance of the sample mean and an altered  $\tau$ -dependence of the  $\text{ADEV} \propto \tau^{-1/2}$  for WPM.

It was shown that with regularly distributed dead time, the AVAR is an unbiased estimator of the variance of the sample mean for WPM. The effect of regularly distributed dead time on the variance of the sample mean and the two-sample variances should be taken into account if measurements with WPM or FPM are scheduled.

Additionally, a  $\Lambda$ -averaged sample mean was constructed and the transfer function concept was used to prove that the corresponding variance of the  $\Lambda$ -averaged sample mean scales with  $1/N^3$  for WPM and  $\Lambda$ -averaged as well as  $\Pi$ -averaged samples. The  $\Lambda$ -averaged sample mean can therefore be used in post-processing of  $\Lambda$ - or  $\Pi$ -averaged samples without dead time to profit from the faster decrease of the uncertainty with the sample size.

The  $\Pi$  and  $\Lambda$  weighting functions belong to the same class of weighting functions, the B-spline basis functions, which are piecewise polynomial functions derived by  $k$ -fold self-convolutions of the rectangular weighting function. It was shown that additional noise types with  $\alpha > 2$  can be discriminated using a two-sample variance based on a higher order B-spline basis weighting function and the minimum order  $k_{\min} = \lceil \alpha/2 \rceil$  of the B-spline for proper discrimination depending on the spectral exponent  $\alpha$  was derived.

GPS time and frequency transfer is a receive-only method: The GPS satellites send signals that are received by the user. Receive-only methods are easy to implement and inexpensive for the user, but since the signals travel only one-way from the satellite to the receiver through the atmosphere, physical influences on the signal have to be carefully corrected or modeled, depending on the required precision. In a two-way method like TWSTFT, the signal is sent from ground station to ground station repeated by the satellite in both directions, so that many of the error contributions are eliminated, because they are common to both paths.

In this chapter the GPS observations and the physical influences on the signals will be shortly reviewed. Some linear combinations of observations that are used in GPS time and frequency transfer techniques will be introduced, before the time and frequency transfer techniques used in this work for frequency comparison of optical clocks, Precise Point Positioning (PPP) and Integer Precise Point Positioning (IPPP), will be discussed in detail.

## 2.1 GPS Observations

All GPS satellites broadcast on at least two frequencies, and every satellite has its own pseudo random noise code that is modulated onto the carrier wave. The frequency of the atomic clock on board the satellites is  $f_0 = 10.23$  MHz and the legacy GPS signals are transmitted on  $f_1 = 154 \times f_0$  (Link 1: L1) and  $f_2 = 120 \times f_0$  (Link 2: L2), which corresponds to wavelengths of  $\lambda_1 = 19.03$  cm for L1 and  $\lambda_2 = 24.42$  cm for L2.

Two observations, the code pseudorange and the carrier-phase are considered. The code measurements have a chipping rate corresponding to a wavelength of 29.31 m for the Precision code (P code) and 293.1 m for the Coarse / Acquisition code (C/A code). The more than 100 times smaller wavelength of the carrier-phase compared to the P code, results in a 100 times higher precision of the carrier-phase observations.

The code observations in meter of the two frequencies  $f_i$  ( $i = 1, 2$ ) are given as

$$P_i = c(t_r - t_s), \quad (74)$$

with the speed of light in vacuum  $c$  and the satellite time in the satellite time scale  $t_s$  and the receiver time in the receiver time scale  $t_r$ . The carrier-phase observations in meter are

$$L_i = c(t_r - t_s) + \lambda_i N_i, \quad (75)$$

with the wavelength  $\lambda_i$  and the integer number of ambiguity cycles  $N_i$ . The carrier-phase measurement, while having a higher precision than the code measurement, is ambiguous and the ambiguity changes whenever the lock on the signal is lost.

To synchronize the satellite and receiver clocks a reference time scale  $\bar{t}$  is introduced. The receiver time is expressed in the reference time scale as  $\bar{t}_r = t_r + \delta t_r$  in which  $\delta t_r$  is the receiver clock error. The satellite time in the reference time scale can be expressed analogously as  $\bar{t}_s = t_s + \delta t_s$  with the satellite clock error  $\delta t_s$ . For time and frequency transfer using GPS the receiver clock error is the parameter of interest.

Using the reference time scale and introducing additional corrections the code and phase observations can be written as

$$P_i = \rho + c(\delta t_r - \delta t_s) + T + I_i + \delta t_{\text{rel}} + b_r^{P_i} - b_s^{P_i} + \epsilon^{P_i}, \quad (76)$$

$$L_i = \rho + c(\delta t_r - \delta t_s) + T - I_i + \delta_{\text{pwu}}^{L_i} + \lambda_i N_i + \delta t_{\text{rel}} + b_r^{L_i} - b_s^{L_i} + \epsilon^{L_i}, \quad (77)$$

in which

$P_i$  is the code measurement of the frequency  $f_i$  in meter,

$L_i$  is the carrier-phase measurement of the frequency  $f_i$  in meter,

$\rho = \|\vec{x}_s(\bar{t}_s) - \vec{x}_r(\bar{t}_r)\|$  is the geometrical range between the satellite ( $\vec{x}_s$ ) and receiver position ( $\vec{x}_r$ ),

$c$  is the speed of light in vacuum,

$\delta t_r$  is the receiver clock error in seconds,

$\delta t_s$  is the satellite clock error in seconds,

$T$  is the tropospheric propagation delay,

$I_i$  are the frequency-dependent ionospheric propagation delays,

$\delta_{\text{pwu}}^{L_i}$  is the carrier-phase wind-up,

$\delta t_{\text{rel}}$  are the relativistic corrections,

$N_i$  is the integer carrier-phase ambiguity,

$\lambda_i$  is the wavelength,

$b_r^{P_i}$  is the frequency-dependent receiver code hardware delay,

$b_s^{P_i}$  is the frequency-dependent satellite code hardware delay,

$b_r^{L_i}$  is the frequency-dependent receiver carrier-phase hardware delay,

$b_s^{L_i}$  is the frequency-dependent satellite carrier-phase hardware delay,

$\epsilon^{P_i}$  is the code observation noise including multipath effects,

$\epsilon^{L_i}$  is the carrier-phase observation noise including multipath effects.

The geometric range in eqs. 76 and 77 already takes into account effects of site displacement, e. g. solid Earth tides, polar tides and ocean loading. Additionally, the phase center offset (PCO) and phase center variation (PCV) of the receiver and satellite antennas have to be applied to the geometric range so that it relates to the center of mass of the satellite and a physical reference point of the ground antenna instead of the electric phase centers of the antennas (Schmid et al., 2007).

Some of the error contributions to the code and carrier-phase observations can be canceled by observation differencing. Forming single differences of simultaneous observations between two GPS stations with respect to the same satellite eliminates the satellite clock error and attenuates other errors, e. g. the satellite orbit errors and common-mode atmospheric propagation delays depending on the geometry. Differences of single differences (double differences) can be used to eliminate the receiver clock error and hardware delays, which is useful for carrier-phase ambiguity fixing. For time and frequency transfer, the difference of the receiver clock errors is the parameter of interest, therefore only undifferenced or single differenced observations are considered.

## 2.2 Linear Combinations of Observations

Linear combinations of the code and carrier-phase observations can be used to eliminate or reduce common biases, geometric effects or to produce observations with different wavelengths. The linear combinations of carrier-phase and code observations  $\{L_i, P_i\}_{i=1}^2$  on the frequencies  $f_1$  and  $f_2$  is

$$LC = \sum_{i=1}^2 \alpha_i^{LC} L_i + \beta_i^{LC} P_i, \quad (78)$$

in which the coefficients  $\alpha_i^{LC}$  and  $\beta_i^{LC}$  are specific for the linear combination.

Assuming that the observations are uncorrelated, the standard variance of the linear combination is

$$\sigma_{LC}^2 = \sum_{i=1}^2 (\alpha_i^{LC} \sigma_{L_i})^2 + (\beta_i^{LC} \sigma_{P_i})^2, \quad (79)$$

with  $\sigma_{L_i}$  and  $\sigma_{P_i}$  being the standard deviations of the carrier-phase and code observations respectively. For the dual-frequency case and assuming the noise levels are the same on both frequencies this results in

$$\sigma_{LC}^2 = [(\alpha_1^{LC})^2 + (\alpha_2^{LC})^2] \sigma_{L_1}^2 + [(\beta_1^{LC})^2 + (\beta_2^{LC})^2] \sigma_{P_1}^2. \quad (80)$$

In the following some linear combinations will be discussed that are used in GPS time and frequency transfer techniques. The relativistic corrections will be omitted and only first-order ionospheric delay will be considered with  $I_2 = f_1^2/f_2^2 I_1$ .

### 2.2.1 Wide-lane (WL) Linear Combination

The wide-lane (WL) carrier-phase linear combination is used to create an observation with a larger wavelength. The coefficients for the WL linear combination are

$$\alpha_1^{WL} = \frac{f_1}{f_1 - f_2}, \quad \alpha_2^{WL} = -\frac{f_2}{f_1 - f_2}, \quad \text{and} \quad \beta_1^{WL} = \beta_2^{WL} = 0, \quad (81)$$

which results in the WL carrier-phase linear combination

$$L_{WL} = \rho + c(\delta t_r - \delta t_s) + \frac{f_1}{f_2} I_1 + T + \lambda_{WL} N_{WL} + b_r^{LWL} - b_s^{LWL} + \epsilon^{LWL}, \quad (82)$$

with the WL receiver and satellite carrier-phase hardware biases

$$b_r^{LWL} = \alpha_1^{WL} b_r^{L1} + \alpha_2^{WL} b_r^{L2},$$

$$b_s^{LWL} = \alpha_1^{WL} b_s^{L1} + \alpha_2^{WL} b_s^{L2},$$

and the WL integer ambiguity  $N_{WL} = N_1 - N_2$ . The wavelength of the WL linear combination  $\lambda_{WL} = c/(f_1 - f_2) \approx 86$  cm is 4.5 times larger than the uncombined wavelength  $\lambda_1$ .

The standard variance of the WL carrier-phase linear combination derived using eq. 80 is

$$\sigma_{L_{WL}}^2 = [(\alpha_1^{WL})^2 + (\alpha_2^{WL})^2] \sigma_{L_1}^2 = \frac{f_1^2 + f_2^2}{(f_1 - f_2)^2} \sigma_{L_1}^2 \approx 33 \sigma_{L_1}^2. \quad (83)$$

This standard deviation increases by a factor of six for the WL carrier-phase linear observation compared to the uncombined carrier-phase measurements.

### 2.2.2 Narrow-lane (NL) Linear Combination

The narrow-lane (NL) linear combination of code observations is used to create a signal with a reduced code noise level. The coefficients of the NL linear combination are

$$\beta_1^{\text{NL}} = \frac{f_1}{f_1 + f_2}, \quad \beta_2^{\text{NL}} = \frac{f_2}{f_1 + f_2}, \quad \text{and} \quad \alpha_1^{\text{WL}} = \alpha_2^{\text{WL}} = 0. \quad (84)$$

which results in the NL linear code combination

$$P_{\text{NL}} = \rho + c(\delta t_r - \delta t_s) + \frac{f_1}{f_2} I_1 + T + b_r^{\text{P}_{\text{NL}}} - b_s^{\text{P}_{\text{NL}}} + \epsilon^{\text{P}_{\text{NL}}}, \quad (85)$$

with the NL receiver and satellite code hardware biases

$$\begin{aligned} b_r^{\text{P}_{\text{NL}}} &= \beta_1^{\text{NL}} b_r^{\text{P}_1} + \beta_2^{\text{NL}} b_r^{\text{P}_2}, \\ b_s^{\text{P}_{\text{NL}}} &= \beta_1^{\text{NL}} b_s^{\text{P}_1} + \beta_2^{\text{NL}} b_s^{\text{P}_2}. \end{aligned}$$

The standard variance of the NL code linear combination derived using eq. 80 is

$$\sigma_{\text{P}_{\text{NL}}}^2 = [(\beta_1^{\text{NL}})^2 + (\beta_2^{\text{NL}})^2] \sigma_{\text{P}_1}^2 = \frac{f_1^2 + f_2^2}{(f_1 + f_2)^2} \sigma_{\text{P}_1}^2 \approx 0.5 \sigma_{\text{P}_1}^2. \quad (86)$$

The noise level of the NL linear combination of code observations has a decreased noise level compared to the uncombined code observations with  $\sigma_{\text{P}_{\text{NL}}} \approx 0.7 \sigma_{\text{P}_1}$ .

### 2.2.3 Melbourne-Wübbena (MW) Linear Combination

The Melbourne-Wübbena (MW) linear combination (Hatch, 1983, Melbourne, 1985, Wübbena, 1985) is a combination of the WL carrier-phase and NL code linear combinations, with the coefficients

$$\alpha_1^{\text{MW}} = \alpha_1^{\text{WL}}, \quad \alpha_2^{\text{MW}} = \alpha_1^{\text{WL}}, \quad \beta_1^{\text{MW}} = -\beta_1^{\text{NL}}, \quad \text{and} \quad \beta_2^{\text{MW}} = -\beta_2^{\text{NL}}. \quad (87)$$

This results in the MW linear combination

$$L_{\text{MW}} = \lambda_{\text{WL}} N_{\text{WL}} + (b_r^{\text{L}_{\text{MW}}} - b_s^{\text{L}_{\text{MW}}}) + \epsilon_{\text{L}_{\text{MW}}}, \quad (88)$$

with the wide-lane receiver bias (WRB)

$$b_r^{\text{L}_{\text{MW}}} = (\alpha_1^{\text{WL}} b_r^{\text{L}_1} + \alpha_2^{\text{WL}} b_r^{\text{L}_2}) - (\beta_1^{\text{NL}} b_r^{\text{P}_1} + \beta_2^{\text{NL}} b_r^{\text{P}_2}) \quad (89)$$

that is a combination of the receiver NL code and WL carrier-phase hardware biases, and the wide-lane satellite bias (WSB)

$$b_s^{\text{L}_{\text{MW}}} = (\alpha_1^{\text{WL}} b_s^{\text{L}_1} + \alpha_2^{\text{WL}} b_s^{\text{L}_2}) + (\beta_1^{\text{NL}} b_s^{\text{P}_1} + \beta_2^{\text{NL}} b_s^{\text{P}_2}) \quad (90)$$

that is a combination of the satellite NL code and WL carrier-phase hardware biases. This combination of code and carrier-phase observations removes the geometry, the receiver and satellite clock errors, and the tropospheric and first-order ionospheric propagation delays.

The standard variance of the MW linear combination derived using eq. 80 is

$$\sigma_{\text{L}_{\text{MW}}}^2 = \sigma_{\text{L}_{\text{WL}}}^2 + \sigma_{\text{P}_{\text{NL}}}^2 = \frac{f_1^2 + f_2^2}{(f_1 - f_2)^2} \sigma_{\text{L}_1}^2 + \frac{f_1^2 + f_2^2}{(f_1 + f_2)^2} \sigma_{\text{P}_1}^2 \approx 33 \sigma_{\text{L}_1}^2 + 0.5 \sigma_{\text{P}_1}^2. \quad (91)$$

The noise level of the MW linear combination is dominated by the NL code noise. The MW linear combination therefore combines the decreased noise level of the



NL code linear combination and the increased wavelength of the WL carrier-phase linear combination, which makes it useful for cycle slip detection and ambiguity fixing.

#### 2.2.4 Ionosphere-free Linear Combinations

The ionosphere is a dispersive medium, therefore the ionospheric propagation delay depends on the frequency and can be removed to first order by forming the so-called ionosphere-free linear combination. The coefficients for the ionosphere-free carrier-phase linear combination are

$$\alpha_1^{\text{IF}} = \frac{f_1^2}{f_1^2 - f_2^2}, \quad \alpha_2^{\text{IF}} = -\frac{f_2^2}{f_1^2 - f_2^2}, \quad \text{and} \quad \beta_1^{\text{IF}} = \beta_2^{\text{IF}} = 0. \quad (92)$$

This results in the ionosphere-free carrier-phase linear combination

$$L_{\text{IF}} = \rho + c(\delta t_r - \delta t_s) + (b_r^{\text{LIF}} - b_s^{\text{LIF}}) + T + \delta_{\text{pwu}}^{\text{LIF}} + \lambda_{\text{IF}} N_{\text{IF}} + \epsilon^{\text{LIF}}, \quad (93)$$

with

$$b_r^{\text{LIF}} = \alpha_1^{\text{IF}} b_r^{\text{L1}} + \alpha_2^{\text{IF}} b_r^{\text{L2}}, \quad \text{the ionosphere-free receiver carrier-phase bias,}$$

$$b_s^{\text{LIF}} = \alpha_1^{\text{IF}} b_s^{\text{L1}} + \alpha_2^{\text{IF}} b_s^{\text{L2}}, \quad \text{the ionosphere-free satellite carrier-phase bias.}$$

The ionosphere-free integer ambiguity  $N_{\text{IF}} = 77N_1 - 60N_2$  and the ionosphere-free wavelength  $\lambda_{\text{IF}} = (2cf_0)/(f_1^2 - f_2^2) \approx 6.3\text{mm}$ , which is 30 times smaller than the uncombined wavelength  $\lambda_1$ .

Likewise, for the ionosphere-free code linear combination, the coefficients are given as

$$\beta_1^{\text{IF}} = \frac{f_1^2}{f_1^2 - f_2^2}, \quad \beta_2^{\text{IF}} = -\frac{f_2^2}{f_1^2 - f_2^2}, \quad \text{and} \quad \alpha_1^{\text{IF}} = \alpha_2^{\text{IF}} = 0. \quad (94)$$

This results in

$$P_{\text{IF}} = \rho + c(\delta t_r - \delta t_s) + (b_r^{\text{PIF}} - b_s^{\text{PIF}}) + T + \epsilon^{\text{PIF}}, \quad (95)$$

with

$$b_r^{\text{PIF}} = \beta_1^{\text{IF}} b_r^{\text{P1}} + \beta_2^{\text{IF}} b_r^{\text{P2}}, \quad \text{the ionosphere-free receiver code bias,}$$

$$b_s^{\text{PIF}} = \beta_1^{\text{IF}} b_s^{\text{P1}} + \beta_2^{\text{IF}} b_s^{\text{P2}}, \quad \text{the ionosphere-free satellite code bias.}$$

The standard variance of the ionosphere-free carrier-phase linear combination derived using eq. 80 is

$$\sigma_{L_{\text{IF}}}^2 = [(\alpha_1^{\text{IF}})^2 + (\alpha_2^{\text{IF}})^2] \sigma_{L_1}^2 = \frac{f_1^4 + f_2^4}{(f_1^2 - f_2^2)^2} \sigma_{L_1}^2 \approx 9\sigma_{L_1}^2. \quad (96)$$

This is an increase of a factor three compared to the standard deviation of the corresponding uncombined observations for the ionosphere-free carrier-phase linear combination and likewise for the ionosphere-free code linear combination  $\sigma_{P_{\text{IF}}} \approx 3\sigma_{P_1}$ .

### 2.3 International GNSS Service (IGS)

The International GNSS Service (IGS) is a voluntary confederation of more than 200 research institutions and government agencies that provide high precision Global

Navigation Satellite System (GNSS) products for applications, that require a higher precision than provided by the broadcasted information (Dow et al., 2009). This includes precise satellite clock and orbit products and Earth rotation parameters. In this work, unless specified otherwise, the final products are used that provide clock products on a sample interval of 30 s. The final products have a latency of 13 d, which is not an obstruction for this work, but for other applications products with a lower latency are provided as well, the rapid and ultra-rapid products with a latency of 17 h and 3 h respectively. The accuracy of the final and the rapid products is 2.5 cm for the satellite orbits and  $< 0.1$  ns for the satellite clocks (*IGS Products 2017*) compared to 5 ns for the broadcasted clock corrections (Senior et al., 2008).

The satellite clock products are referenced to a reference time scale, the IGS Time (IGST). The IGST is an ensemble of satellite clocks and atomic station clocks and is steered to align the time scale with Coordinated Universal Time (UTC), its stability is below  $1 \times 10^{-15}$  for an averaging time of 1 d and above.

## 2.4 Common-View (CV) and All-in-View (AV)

A simple approach to compare clocks using GNSS is the Common-View (CV) method (Allan et al., 1980). In a CV analysis single differences between the observations of two stations with respect to the same satellite are formed. The clocks under study serve as the time and frequency reference of the receiver, replacing the internal receiver clocks. For dual-frequency receivers the ionosphere-free linear combination is used. The Code-CV single difference of the ionosphere-free linear combination of code observations between two stations is

$$\Delta P_{IF} = \Delta \rho + c \Delta t_r + \Delta T + \Delta b_r^{P_{IF}} + \epsilon^{\Delta P_{IF}}, \quad (97)$$

in which  $\Delta t_r$  is the difference of the receiver clock errors of the GPS stations. This single differences removes the satellite clock error and attenuates other error sources that are partly common for both observations, e. g. satellite position errors. The constant component of the relative code hardware delays  $\Delta b_r^{P_{IF}}$  can be calibrated, but the time variable part of the code hardware delays is indistinguishable from the clock difference. The range difference can be calculated using the known antenna station coordinates and the broadcasted orbit information or the precise orbit products, e. g. IGS orbit products. Additionally, a tropospheric delay correction and relativistic corrections have to be applied. If a single frequency receiver is used, ionospheric corrections e. g. from broadcasted parameters and the L1-L2 broadcast corrections have to be used.

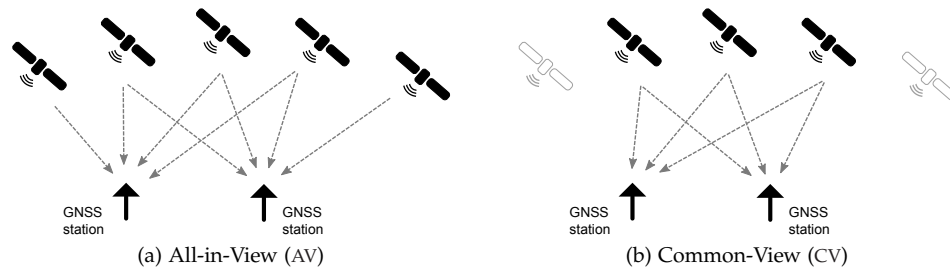


Figure 15: Schematic depiction of the AV and CV methods.

For long baselines, the number of satellites that are in common view decreases, and the elevation of the satellites in common view is lower. For lower elevations

the signal-to-noise ratio is lower and the corrections of the propagation delays in the atmosphere are less precise. It has been shown that for baselines longer than 2500 km, an All-in-View (AV) approach that averages the clock difference between the receiver clock and the satellite reference time scale over all satellites in view independently for each station, leads to an improvement of the link instability (Petit et al., 2008a; Weiss et al., 2005). Since the satellite clock errors do not cancel in this approach, they should be taken from precise clock products instead of the broadcasted information. The stability of Code-CV links based on the ionosphere-free linear code combination is below 1 ns for averaging times of 1 d and above.

In this work a Code-CV software was implemented based on the CGGTTS data format (Allan et al., 1994) that contains the time difference between the receiver clock and the satellite reference time scale averaged over 13 min intervals and corrected with the above mentioned corrections and the broadcasted satellite orbits and clocks.

## 2.5 Precise Point Positioning (PPP)

Precise Point Positioning (PPP) is a geodetic positioning method (Kouba et al., 2001a; Zumberge et al., 1997) that does not require a reference station, it can be classified as an AV method. This AV method is based on the undifferenced ionosphere-free code and carrier-phase linear combinations, which drastically improves the precision compared to code-only techniques like Code-CV and Code-AV, but also requires more refined corrections and models. All effects that surpass the noise level of the carrier-phase of a few mm have to be corrected.

For undifferenced processing, the precision of the broadcasted satellite clock and orbit information is not sufficient. Precise satellite clock and orbit information, e. g. from the IGS, are necessary. The estimated receiver clock error for a single GPS station is then relative to the reference time scale of the precise satellite products, e. g. IGST.

The application of the PPP technique for time and frequency transfer has been studied, e. g. in Defraigne et al., 2007; Guyennon et al., 2009; Orgiazzi et al., 2005; Weiss et al., 2004, and since 2008 it is used for time links in TAI computation (Petit et al., 2008b).

After a brief discussion of the standard observation model with the corrections and models that have to be applied, the application of PPP for time and frequency transfer will be discussed. A special focus will be on the phenomenon of batch-boundary discontinuities, their origin and possible solutions for continuous PPP clock solutions and their pitfalls.

### 2.5.1 Standard Observation Model

The following corrections and models are used for PPP:

**Site Displacement:** The coordinates of the GPS station are affected by tidal motions due to the deformation of the Earth's crust. The main effects are solid Earth tides due to gravitational forces of the Sun and Moon, ocean loading due to the elastic response of the Earth's crust to ocean tides, and solid Earth pole tides due to shifts of the Earth's rotation axis. The software used in this work models these effects according to the IERS Conventions 2010 (Petit et al., 2010).

**Antenna Phase Center Variations:** The observed signals are referred to the electric phase center of the transmitter and receiver antenna, in order to refer the measurements to the center of mass of the satellite and a physical reference point of

the receiver antenna phase center offset (PCO) and phase center variation (PCV) corrections have to be applied. The frequency-dependent PCO and PCV are taken from the IGS ANTEX file (Rothacher et al., 2010). More information on the correction models can be found e. g. in Schmid et al., 2007.

**Carrier-Phase Wind-Up:** The GPS signals are right circularly polarized waves, and the carrier-phase observation therefore depends on the relative orientation of the satellite and receiver antenna. During the pass of a satellite this orientation changes. This effect can reach several cm and is corrected based on the expressions derived in Wu et al., 1993.

**Relativistic Corrections:** Relativistic clock and path range corrections have to be applied. The receiver and the satellite clock experience different gravitational potentials (general relativity) and move at a relative velocity (special relativity). A constant component of the relativistic clock correction is covered by adjustment of the frequency of the clocks on board the satellites. A periodic component, that depends mainly on the orbital eccentricity of the satellite has to be applied as a correction by the user. Additionally, the Shapiro effect, a propagation delay due to the curvature of the space-time caused by the gravitational field of the Earth has to be considered. A review of relativistic effects relevant for GPS can be found in Ashby, 2003.

**Troposphere:** The tropospheric propagation delay is separated into two parts, a hydrostatic component that can be predicted and applied as correction and a wet component that has to be estimated. The hydrostatic tropospheric delay is caused by dry gases in the troposphere and depends on the atmospheric pressure and temperature. The wet component is caused by water vapor in the troposphere and depends on the local weather. The tropospheric delays depend on the elevation angle  $e$  of the satellite:

$$T(e) = T_h(e) + T_w(e) = mf_h(e) \cdot zhd + mf_w(e) \cdot zwd. \quad (98)$$

The wet and hydrostatic component are expressed in terms of elevation dependent mapping functions  $mf_h$  and  $mf_w$  and the propagation delays at the zenith, the zenith hydrostatic delay ( $zhd$ ) and zenith wet delay ( $zwd$ ). For IPPP processing using the Géodésie par Intégrations Numériques Simultanées (GINS) (Marty, 2013) software, the Global Mapping Function (GMF) (Boehm et al., 2006) is used for the mapping of the hydrostatic and wet component and the meteorological data from the Global Pressure and Temperature (GPT) model (Boehm et al., 2007) is used for the determination of the  $zhd$ . For the National Resources Canada (NRCan) PPP (Kouba et al., 2001b) processing in this work, unless indicated otherwise, the updated GPT2 model (Lagler et al., 2013) is used that includes the meteorological data and the mapping coefficients.

#### 2.5.1.1 Ionosphere-free Code Clocks

The above mentioned corrections and models are applied to the ionosphere-free linear combinations (eq. 93 and 95), leading to

$$P_{IF}^C = \rho + c(\delta t_r - \delta t_s) + b_r^{P_{IF}} - b_s^{P_{IF}} + T_w + \epsilon^{P_{IF}}, \quad (99)$$

$$L_{IF}^C = \rho + c(\delta t_r - \delta t_s) + b_r^{L_{IF}} - b_s^{L_{IF}} + T_w + \lambda_{IF} N_{IF} + \epsilon^{L_{IF}}. \quad (100)$$

The equation system based on eqs. 99 and 100 is still under-determined, even if the satellite clock error  $\delta t_s$  is provided. Every satellite adds two equations to the

equation system, but at the same time two more hardware biases that have to be estimated. To overcome the singularity of the equation system, ionosphere-free clock errors are defined that absorb the corresponding ionosphere-free biases. The ionosphere-free code clock error is given as

$$c\delta t_r^{\text{P}_{\text{IF}}} = c\delta t_r + b_r^{\text{P}_{\text{IF}}} \quad (101)$$

for the receiver, and

$$c\delta t_s^{\text{P}_{\text{IF}}} = c\delta t_s + b_s^{\text{P}_{\text{IF}}} \quad (102)$$

for the satellite.

The ionosphere-free code satellite clock errors  $\delta t_s^{\text{P}_{\text{IF}}}$  are provided by the precise satellite clock products, e. g. IGS products, and used as corrections. With eqs. 101 and 102 the ionosphere-free linear combinations of code (eq. 95) and carrier-phase observations (eq. 93) with the remaining parameters can be written as:

$$P_{\text{IF}}^c + c\delta t_s^{\text{P}_{\text{IF}}} = \rho + c\delta t_r^{\text{P}_{\text{IF}}} + T_w + \epsilon^{\text{P}_{\text{IF}}}, \quad (103)$$

$$\begin{aligned} L_{\text{IF}}^c + c\delta t_s^{\text{P}_{\text{IF}}} &= \rho + c\delta t_r^{\text{P}_{\text{IF}}} + (b_r^{\text{L}_{\text{IF}}} - b_s^{\text{L}_{\text{IF}}} - b_r^{\text{P}_{\text{IF}}} + b_s^{\text{P}_{\text{IF}}}) + T_w + \lambda_{\text{IF}}N_{\text{IF}} + \epsilon^{\text{L}_{\text{IF}}} \\ &= \rho + c\delta t_r^{\text{P}_{\text{IF}}} + a^{\text{P}_{\text{IF}}} + T_w + \epsilon^{\text{L}_{\text{IF}}}. \end{aligned} \quad (104)$$

The code and carrier-phase satellite and receiver biases are combined to one ambiguity parameter  $a^{\text{P}_{\text{IF}}} = \lambda_{\text{IF}}N_{\text{IF}} + b_r^{\text{L}_{\text{IF}}} - b_s^{\text{L}_{\text{IF}}} - b_r^{\text{P}_{\text{IF}}} + b_s^{\text{P}_{\text{IF}}}$  together with the integer carrier-phase ambiguity. This combined ambiguity  $a^{\text{P}_{\text{IF}}}$  is a floating number and therefore the integer nature of the carrier-phase ambiguity  $N_{\text{IF}}$  can not be preserved. The code observations are necessary in this model to decorrelate the receiver code clock error  $\delta t_r^{\text{P}_{\text{IF}}}$  and the ambiguity parameter  $a^{\text{P}_{\text{IF}}}$ . Other parameters that are correlated with the receiver clock error are the height component of the coordinates and the wet tropospheric propagation delay  $T_w$ , especially for high elevation satellites (Rothacher et al., 1998).

It is noted that in this model, from now on referred to as the standard model, the true receiver clock error  $\delta t_r$  can not be accessed, but only the code receiver clock error  $\delta t_r^{\text{P}_{\text{IF}}}$  that contains the receiver code bias (eq. 101). The receiver code and carrier-phase biases are not constant in general and especially the receiver code biases can show significant time variability leading to code-phase inconsistencies.

### 2.5.2 Code-Phase Inconsistencies

Since the standard model for PPP processes code and carrier-phase observations together, attention has to be paid to their consistency. Some causes for time variable code-phase inconsistencies have been identified in the literature.

**Environmental effects:** One source for code-phase inconsistencies is multipath that has a larger effect on the code compared to the carrier-phase observation. Multipath interference occurs, when a signal arrives at the receiver by different paths, due to reflections in the environment of or in the GPS station. The effect depends on the frequency of the signal and the observation type. Multipath on the carrier-phase observation is limited to one-fourth of the wavelength (Seeber, 2003), which is  $\approx 90$  ps for  $L_{\text{IF}}$ , while the theoretical limit for the code observation is 1.5 times the chip wavelength with typical values up to a few ns for the P code. One can distinguish between satellite-specific multipath that only affects one satellite and common-mode multipath that affects all satellites in a similar way. Common-mode multipath originates either in the station hardware or in the near-field of the antenna (Defraigne et al., 2007). Similarly, the code observations are more sensitive to temperature

induced hardware delay variations (Overney et al., 1997; Powers et al., 1998). Effects that affect all code observations, e.g. receiver hardware delay variations and common-mode multipath, are more difficult to distinguish from the receiver clock than satellite-specific events.

**Asynchronous Measurements:** Another source of code-phase inconsistencies are imperfections in the receiver design, in the measurement process or in the subsequent data processing in the receiver software that lead to asynchronous measurements of the code and carrier-phase observations. As demonstrated in Defraigne et al., 2016, an asynchronous measurement leads to a frequency offset between the code and the carrier-phase clock solutions. The resulting drift of the PPP clock solution is proportional to the time offset between the carrier-phase and the code measurements (30 ps per day per 1  $\mu$ s time offset). If the time offset is known the drift can be corrected using the measured carrier-phase Doppler frequency. This problem was observed in several receivers used for time and frequency applications, e.g. Dach et al., 2006; Matsakis et al., 2015.

The impact of the code-phase inconsistencies on the PPP clock solution depends on the type of inconsistency, especially whether the inconsistency is a common-mode effect, as well as the details of the algorithmic implementation of the PPP parameter adjustment. One manifestation of code-phase inconsistencies in the standard PPP model are large batch-boundary discontinuities, which will be discussed in subsec. 2.5.4.

### 2.5.3 Parameter Adjustment

The standard model (eq. 104 and eq. 103) needs to be linearized for the adjustment process. The geometric range  $\rho$  is linearized using a Taylor series expansion around an approximate receiver position  $\vec{x}_0 = (x_0, y_0, z_0)$ :

$$\rho = \rho_0 + \frac{x_0 - x_s}{\rho_0} dx + \frac{y_0 - y_s}{\rho_0} dy + \frac{z_0 - z_s}{\rho_0} dz. \quad (105)$$

The linear observation model is then given as

$$\mathbf{y} = \mathbf{A}\mathbf{x} + \mathbf{v}, \quad (106)$$

with the  $n \times 1$  vector  $\mathbf{y}$  of the code and carrier-phase observation prefit residuals  $P_{\text{IF}}^c - \rho_0 + c\delta t_s^{\text{PIF}}$  and  $L_{\text{IF}}^c - \rho_0 + c\delta t_s^{\text{PIF}}$  for each observation epoch and satellite. The  $p \times 1$  vector of unknown parameters

$$\mathbf{x} = \left[ dx, dy, dz, (c\delta t_r^{\text{PIF}})_1, \dots, (c\delta t_r^{\text{PIF}})_j, (zwd)_1, \dots, (zwd)_k, (a_{\text{PIF}})_1, \dots, (a_{\text{PIF}})_l \right] \quad (107)$$

contains the corrections to the station coordinates (static coordinates), the receiver clock errors, the  $zwd$ s, and the ambiguities. The  $n \times p$  design matrix  $\mathbf{A}$  contains the partial derivatives of the observations with respect to the unknown parameters  $\mathbf{x}$  and the  $n \times 1$  vector of residual errors or postfit residuals  $\mathbf{v}$ .

The least-square parameter adjustments aims to find the parameters that minimize the quadratic form of the postfit residual with the condition  $\min(\mathbf{v}^T \mathbf{v})$ . The quality of the observations depend on the elevation angle of the satellite. To take into account the varying quality of the observations, a weighted least-squares solutions can be used, introducing a  $n \times n$  weighting matrix  $\mathbf{P}$  and redefining the least-squares condition as  $\min(\mathbf{v}^T \mathbf{P} \mathbf{v})$ . The parameters that fulfill this condition

are found by multiplying the linear observation model (eq. 106) on both sides with  $\mathbf{A}^T \mathbf{P}$  leading to the normal equations  $\mathbf{A}^T \mathbf{P} \mathbf{A} \mathbf{x} = \mathbf{A}^T \mathbf{P} \mathbf{y}$  and the parameter solution

$$\mathbf{x} = (\mathbf{A}^T \mathbf{P} \mathbf{A})^{-1} \mathbf{A}^T \mathbf{P} \mathbf{y}. \quad (108)$$

The least-square adjustment can be performed either in a single batch or using a sequential filter, e. g. Kalman filter (Kalman, 1960). The GINS software used for IPPP processing in this work uses a single batch solution, whereas the NRCAN software used for PPP processing uses a Kalman filter.

If a batch processing is used, the parameters are estimated with a certain rate that should reflect the typical rate of change of the corresponding parameter depending on the user dynamic. Typical estimation rates for time and frequency transfer applications with a batch length of one day are every epoch for the receiver clock error, every satellite pass for the ambiguity, daily for the coordinates and every hour for the troposphere.

If a Kalman filter is used, assumptions have to be made about the 'process noise' of the parameters. The receiver clock error is often modeled as an almost unconstrained white-noise process. For time and frequency transfer applications, the reference clocks are highly stable oscillators, so that the short-term instability can profit from more constrained clock models (Cerretto et al., 2008, 2010). In the NRCAN software, the tropospheric  $zwd$  is modeled as a random walk process constrained with 2 to 5 mm/ $\sqrt{h}$ . The estimated parameters, especially the unconstrained parameters like the receiver clock error, require a certain time to converge after initialization. In order to achieve optimal solutions for the whole data batch, the final clock errors and  $zwd$ s can be recovered in a backward substitution, in which the station coordinates and the converged ambiguities are held fixed.

#### 2.5.4 Batch-Boundary Discontinuities

The PPP computations are usually performed in batches, e. g. daily batches. The clock solutions from consecutive batches are not necessarily continuous at the batch-boundary. This day-boundary discontinuities have been studied in detail in Senior et al., 2001 and Defraigne et al., 2007. Batch-boundary discontinuities occur because in the standard PPP model the code measurements are used to decorrelate the floating carrier-phase ambiguities  $a^{PIF}$  and the receiver code clock error  $\delta t_r^{PIF}$ . The details depend on the implemented algorithm, but it is fair to say that as long as code measurements are used for this purpose, code noise in the clock solution is inevitable and will eventually lead to batch-boundary discontinuities. For the same reason discontinuities occur if all carrier-phase ambiguities have to be reinitialized at the same time within a batch, e. g. due to a loss of lock, a data gap or a change in the time and frequency reference of the receiver.

For some stations, day-boundary discontinuities of more than 1 ns in clock comparisons have been observed, with a Root Mean Square (RMS) value between 170 ps and 1200 ps for selected IGS stations (Ray et al., 2003, 2005). As discussed in Defraigne et al., 2007, day-boundary discontinuities up to 150 ps can be explained by short-term white code noise and satellite-specific multipath while larger discontinuities are probably a result of long-term common-mode colored code noise. The size of the batch-boundary discontinuities is therefore station-dependent and large batch-boundary discontinuities as well as a non-zero average of the discontinuities can be a sign of a problem with the station equipment or antenna near-field environment.

### 2.5.5 Continuous PPP solutions

For time and frequency transfer a continuous clock solution would be favorable, e. g. because the batch-boundary discontinuities affect the estimated frequency instability, therefore several methods have been proposed to create continuous clock solutions:

**Longer batches:** Longer batches can be used to reduce the number of batch-boundary discontinuities. Depending on the dominant code noise type, longer batches and therefore longer averaging of the code measurements does not necessarily reduce the size of the discontinuities. Due to long-term systematic effects in the station hardware or multipath the dominant code noise type might be non-white (Defraigne et al., 2007) in which case longer averaging times might even lead to larger discontinuities as discussed in Petit et al., 2008b.

This method is especially useful to create continuous clock solutions for time and frequency transfer campaigns of shorter length. The NRCan PPP software used in this work allows currently for batch lengths up to 45 days (Orgiazzi et al., 2005). This software is used regularly for TAI PPP computations with monthly batches (Petit et al., 2008b). A median batch-boundary discontinuity size of 170 ps for stations contributing to TAI was reported in Petit et al., 2011.

**Continuous processing:** In principle the batch length could be extended infinitely, but this is computationally expensive and might be unpractical for many applications. Furthermore various error effects might accumulate over long time-spans (Dach et al., 2003).

**Ambiguity stacking and clock handover:** In Dach et al., 2006 two approaches are discussed that stack information from independent daily batches to form a continuous clock solution. In the more sophisticated ambiguity stacking approach the carrier-phase ambiguities are stored for later use, while in the clock handover method only the clock solution at the batch-boundary is stored. This approach requires a lot of book keeping and the information to create continuous solutions is not available for external users.

**Concatenation of overlapping batches:** Another method that has been proposed by various authors (Bruyninx et al., 1999, Larson et al., 2000, Dach et al., 2002) is the concatenation of batches using overlapping batches to correct the batch-boundary discontinuities. The main critique of this approach is that even if the discontinuities stem from a white noise process, the remaining error of this correction introduces a random walk noise component which can accumulate over time (Ray et al., 2005).

**Sliding batches:** In this method a multi-day batch is processed and only the day in the middle of the batch interval contributes to the final clock solution, then the batch is slided by one day to generate the final clock solution for the following day (Guyennon et al., 2009). This method can reduce the size of the day-boundary discontinuities, but does not avoid them. The reported mean day-boundary discontinuity size is below 100 ps for most stations.

**Revised Rinex Shift (RRS):** A similar approach to the sliding batches is used in the RRS method (Yao et al., 2013, 2014, 2015), but here only the middle epoch instead of the middle day is extracted from the clock solution of the sliding batch, which results in a more continuous solution, but is also even more computationally expensive. Some of the claims in Yao et al., 2015 about RRS having a better stability than a long continuous batch solution have been refuted in Petit et al., 2016.



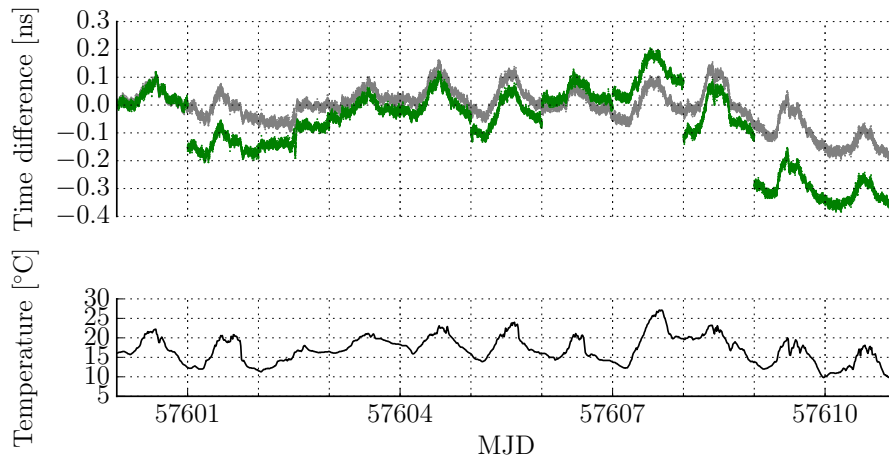


Figure 16: Top: Daily (green) and continuous (grey) batch PPP clock comparison using the NRCan software for a local common-clock baseline at PTB; Bottom: Outside temperature.

An example of a long continuous batch and a daily batches PPP clock comparison for a local common-clock baseline at PTB is shown in fig. 16. The sub-daily variations and the long-term drift are likely due to temperature-induced hardware delay variations in the outdoor equipment of one of the stations which might contribute to the large day-boundary discontinuities of up to 200 ps. The Pearson correlation coefficient between the size of the day-boundary discontinuities and the difference in the mean daily temperature is 0.5. The Pearson correlation coefficient is a measure of the correlation between two variables, it is defined as the ratio of the autocovariance of two variables and the product of the deviations of the individual variables, and it is 1 for a perfect linear correlation and 0 for no correlation (Pearson, 1895).

If methods to create a continuous clock solution are used it is good practice to compare the continuous clock solution to clock solutions from shorter batches to detect potential problems that might be hidden in a continuous solution. A potential pitfall is that a sudden change in the code measurements, e.g. due to near-field multipath or receiver hardware problems, might not translate to a sudden and therefore easily detectable change in the clock solution, but might have a more subtle effect, e.g. a drift over several days. This undetected frequency offset would lead to a systematic error in a clock frequency comparison. The effect of an overlooked change in the station hardware on a continuous NRCan PPP clock solution was reported in Defraigne et al., 2008 on a baseline between PTB and United States Naval Observatory (USNO), in which it led to a drift of  $\approx 5$  ns over 10 days, which corresponds to a systematic relative frequency offset of  $6 \times 10^{-15}$ .

As pointed out in Ray et al., 2005, large batch-boundary discontinuities and their causes should be „identified and ameliorated, not hidden from view by post-analysis manipulations“. Furthermore, while some of the discussed methods (e.g. ambiguity stacking) intervene in the PPP processing, most are post-processing methods that use standard PPP software with the standard observation model to create clock solutions. This standard clock solutions are then the base for further processing that aims to reduce the batch-boundary discontinuities. This methods reduce the size or frequency of the batch-boundary discontinuities, but they do not address the underlying issue of code noise in the clock solution and code-phase inconsistencies.

## 2.6 Integer Precise Point Positioning (IPPP)

Several methods have been proposed to overcome the problems of the standard PPP model introduced in sec. 2.5.1 (Bertiger et al., 2010; Collins, 2008; Ge et al., 2007; Geng et al., 2012; Lannes et al., 2013; Laurichesse et al., 2007; Mervart et al., 2008; Teunissen et al., 2010; Wübbena et al., 2005). In one way or the other, they separate the phase and code hardware biases and preserve the integer nature of the phase ambiguity. It has been shown that the proposed models are in principle equivalent in terms of the integer ambiguity recovery and the number of additional satellite corrections and the minimum number of satellites that are needed in the user solution (Geng et al., 2010, Shi et al., 2014, Teunissen et al., 2015) and that transformations exist that allow to mix the different methods on the user and network side (Teunissen et al., 2015). In the following the focus will be on the integer recovery clock (IRC) model described in Laurichesse et al., 2007, 2009; Loyer et al., 2012, which is implemented in the GINS software (Marty, 2013) that is used in this work for IPPP processing.

### 2.6.1 Decoupled Clock Model

In sec. 2.5.1 the ionosphere-free code clock errors (eq. 101, 102) were defined. Analogously carrier-phase clock errors can be defined that absorb the corresponding carrier-phase biases

$$c\delta t_r^{\text{LIF}} = c\delta t_r + b_r^{\text{LIF}}, \quad (109)$$

for the receiver, and

$$c\delta t_s^{\text{LIF}} = c\delta t_s + b_s^{\text{LIF}} \quad (110)$$

for the satellite. With eq. 109 and 110 the ionosphere-free carrier-phase observation model (eq. 93) can be written as

$$L_{\text{IF}}^c + c\delta t_s^{\text{LIF}} = \rho + c\delta t_r^{\text{LIF}} + T_w + \lambda_{\text{IF}} N_{\text{IF}} + \epsilon^{\text{LIF}}. \quad (111)$$

The ionosphere-free carrier-phase clock errors  $\delta t_s^{\text{LIF}}$  have to be provided by the precise satellite products and used as corrections.

This observation model (eq. 103, 111), also called the 'decoupled clock model' (Collins et al., 2010), uses separate code and carrier-phase clock errors, taking into account the time variability of the code and carrier-phase hardware biases. This model still does not give access to the true receiver clock error  $\delta t_r$ , but instead to the ionosphere-free carrier-phase clock error  $\delta t_r^{\text{LIF}}$  that contains the ionosphere-free carrier-phase receiver hardware bias. But since the carrier-phase observations not only have a lower noise level than the code observations but are also less sensitive to systematic environmental effects like multipath and temperature-induced hardware delay variations, the carrier-phase clock error  $\delta t_r^{\text{LIF}}$  can be expected to be closer to the true receiver clock error  $\delta t_r$  than the code clock error  $\delta t_r^{\text{P}}^{\text{LIF}}$ .

### 2.6.2 User Ambiguity Resolution

In eq. 111 the integer nature of the phase ambiguity is preserved, but due to the high measurement noise  $\sigma_{\text{LIF}} \approx 3\sigma_{\text{L}_1}$  (eq. 96) with  $\sigma_{\text{L}_1}$  typically being a few mm and the small ionosphere-free wavelength  $\lambda_{\text{IF}} \approx 6$  mm the integer ambiguity  $N_{\text{IF}}$  can not be resolved. Instead the ambiguity resolution is performed in two steps:

1. WL ambiguity fixing:

First, the MW linear combination (eq. 88) is used to fix the integer WL ambiguity  $N_{WL}$ . With a typical noise level of 30 cm for the P code, the noise level  $\sigma_{L_{MW}} \approx \sigma_{P_{NL}} \approx 21$  cm (eq. 86) is sufficiently small compared to the WL wavelength  $\lambda_{WL} \approx 86$  cm to allow the use of the MW linear combination to determine the integer WL ambiguity  $N_{WL}$ :

$$L_{MW} - \overline{b_r^{L_{WM}}} + b_s^{L_{MW}} = \lambda_{WL} N_{WL}, \quad (112)$$

with the WSB  $b_s^{L_{MW}}$ , that have to be provided by the precise satellite products. The WSBs are sufficiently stable to use daily averages for the WL ambiguity fixing (Mercier et al., 2008).

A byproduct of the WL ambiguity fixing are the WRBs  $\overline{b_r^{L_{WM}}}$ , which are determined by averaging the fractional part of the floating ambiguity  $\lambda_{WL} \alpha_{WL} = L_{MW} + b_s^{L_{MW}}$  from all observations. The WRBs can vary up to one WL cycle in a few minutes for certain receivers (Mercier et al., 2008), so they have to be calculated at every epoch. Cycle slips can occur in the WRBs at the day-boundaries, if their value is close to 0.5 WL cycles, leading to a cycle slip in the set of WL ambiguities for all  $n$  observations  $\{N_{WL}\}_{i=1}^n$ .

Since the WRB is the difference between the weighted carrier-phase and code receiver hardware delay biases (eq. 89), they are a noisy detector for code-phase inconsistencies and their stability is an indicator of the quality of the GPS station.

## 2. Ambiguity fixing in the undifferenced ionosphere-free phase equation:

Substituting  $N_{IF} = -17N_1 + 60N_{WL}$  in eq. 111 leads to

$$L_{IF}^c + c\delta t_s^{L_{IF}} - 60\lambda_{IF}N_{WL} = \rho + c\delta t_r^{L_{IF}} + T - 17\lambda_{IF}N_1 + \epsilon^{L_{IF}}. \quad (113)$$

After identifying the WL ambiguity  $N_{WL}$  in the first step, the integer ambiguity  $N_1$  can be resolved using eq. 113, due to the larger NL wavelength  $\lambda_{NL} = 17\lambda_{IF} \approx 10.7$  cm.

A cycle slip in the WL ambiguities  $\{N_{WL}\}_{i=1}^n$  determined in the previous step equates to a slip of  $60\lambda_{IF} \approx 3.5\lambda_{NL}$  on the left side of eq. 113, which will be partly compensated by the estimated ambiguity  $N_1$ , but the remaining  $0.5\lambda_{NL}$  will lead to a cycle slip in the carrier-phase receiver clock error. This cycle slip in the phase receiver clock error can be corrected in a post-processing step, if cycle steps in the WRB have been observed (Petit et al., 2016).

To provide the necessary satellite phase clocks and the WSBs the same decoupled clock model and estimators are used in the network solution for the precise satellite products. A reference network station is chosen, whose WRB is set to zero to eliminate the rank defect in the network solution. The discussed ambiguity resolution method is sometimes described as an undifferenced ambiguity resolution (e.g. Laurichesse et al., 2009), but it has been argued in Teunissen et al., 2015, that the necessary satellite corrections are not absolute, but relative to a reference network station, and therefore the user ambiguities  $N_{WL}$  and  $N_1$  can be considered double-differenced in respect to the reference network station, even though an undifferenced formulation is used in the user ambiguity resolution.

### 2.6.3 Precise Integer Satellite Products

At the moment, three IGS analysis centers (ACs) provide the additional information that is necessary to recover the integer nature of the carrier-phase ambiguity in

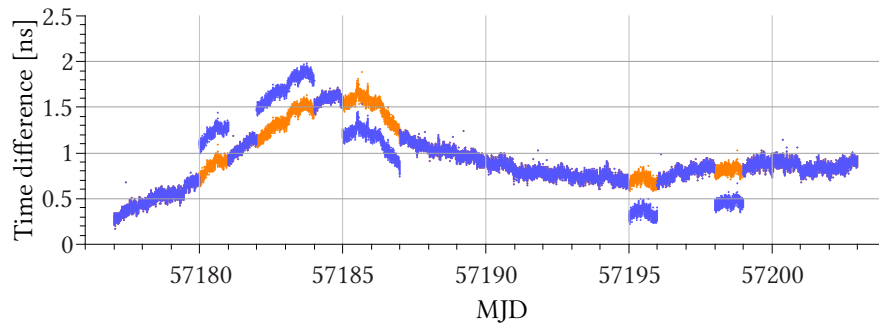


Figure 17: Example of day-boundary discontinuities in an IPPP link between two stations equipped with AHMs. The original link solution (blue) shows several day-boundary discontinuities of  $\lambda_{\text{NL}} = 0.357 \text{ ns}$  that have been corrected in a post-processing step (orange). A linear drift has been removed from both solutions.

the user IPPP solution. These are the Centre National d'Études Spatiales (CNES) AC (Loyer et al., 2012), the NRCan AC (Collins, 2008) and the Scripps Institution of Oceanography AC (Geng et al., 2013). In this work the GRG satellite products from CNES AC are used for IPPP processing.

At this point the user has to choose products from a single AC for IPPP and can not profit from the improved robustness of the combined standard products offered by the IGS (Kouba et al., 2001a). This situation might improve in the future, when combined products become available that offer the necessary satellite corrections and combine solutions from several ACs (Seepersad et al., 2016).

#### 2.6.4 Link Formation

In this work daily IPPP solutions are produced using the GINS software and GRG products. When solutions from two stations are combined to compare the reference clocks, this link solution may be discontinuous at the day-boundaries, due to the satellite clocks not being aligned between days. But since these discontinuities are an integer multiple of  $\lambda_{\text{NL}}$ , this discontinuity can be corrected.

In Petit et al., 2016 three methods are proposed to determine the integer multiple. Either overlapping products, a reference method (e.g. continuous batch PPP) or in the case of highly stable reference clocks extrapolation can be used. In this work the extrapolation method was used, because the reference clocks are sufficiently stable AHMs. The integer multiple of  $\lambda_{\text{NL}}$  is determined by a linear fit to the data at the end of a daily batch and at the beginning of the subsequent day. The same procedure is applied if a reset of all ambiguities occurs in the IPPP processing of one of the stations within a daily batch, e.g. due to a loss of lock or data gap. The difference between the linear fits at the discontinuity is then divided by  $\lambda_{\text{NL}}$  and rounded to the nearest integer to determine the integer multiple.

In this work, the linear fits were performed over a 4 h time period. At an averaging time of 4 h the instability of a IPPP link between stations equipped with AHMs is usually below 20 ps (Time Deviation (TDEV)), which is sufficiently small to detect and correct day-boundary discontinuities of  $0.5\lambda_{\text{NL}} = 178 \text{ ps}$ . An example of day-boundary discontinuities in an IPPP link solution between stations equipped with AHMs is shown in fig. 17.

## 2.7 Summary

The standard model of PPP and its drawbacks were discussed. The standard model mixes carrier-phase and code hardware biases in one parameter and is therefore not equipped to properly deal with code-phase inconsistencies, which can lead to large batch-boundary discontinuities in the PPP clock solution in the presence of code-phase inconsistencies. Various methods to reduce the effect of batch-boundary discontinuities were discussed. The discussed methods for continuous PPP processing based on the standard model do not solve the underlying problem and can potentially lead to systematic frequency offsets in frequency comparisons in the presence of code-phase inconsistencies.

A valid approach to overcome the limitations of the standard PPP model is the IPPP model, that separates the code and carrier-phase hardware biases in a decoupled clock model and is therefore not affected by code-phase inconsistencies. IPPP can be interpreted as a phase-only technique, because the code observations are used in the ambiguity fixing process without adding noise to the estimated parameters, due to the integer-nature of the fixed ambiguity. An alternative carrier-phase only method to IPPP would be carrier-phase CV, a method based on single-difference ambiguity fixing (Delporte et al., 2008). Carrier-phase CV suffers from the same limitations on long baselines as Code-CV, the declining number of satellites, a higher signal-to-noise ratio and less precise propagation delay corrections.

A drawback of phase-only techniques is that they do not provide absolute time information. For time transfer the IPPP links have to be calibrated, which adds an additional calibration uncertainty. The calibration of carrier-phase only method could be performed by using code-based techniques or by using an independent method like TWSTFT. For the frequency comparison of optical clocks, a time calibration is not necessary and the calibration issue will not be considered in this work.

The instability of a GNSS time and frequency link between two stations depends not just on the post-processing data analysis strategy discussed in chap. 2 but also on the hardware stability of the stations. In chap. 3.1, the hardware stability of GNSS stations will be reviewed and the implication for frequency comparisons using GNSS time and frequency transfer techniques will be discussed.

In the following, local common-clock baselines (ch. 3.2) between GNSS stations at PTB will be studied to test the stations suitability for frequency comparisons of optical clocks and to study the performance of PPP and IPPP links on short common-clock baselines. In a common-clock setup all stations are referenced to the same time and frequency reference, so that the difference of the clock solutions between the stations is dominated by instability of the link itself and not limited by the time and frequency reference.

In ch. 3.3 continental PPP and IPPP links on baselines between European NMIs that operate optical clocks will be studied. The long-term instability of the continental links is limited by the instability of the AHMs that are used as time and frequency reference. For the continental baseline between PTB and LNE-SYRTE a ground truth can be established by comparison with a 1415 km long optical fiber link. This optical fiber link will be used to characterize the PPP and IPPP links between LNE-SYRTE and PTB (ch. 3.4).

### 3.1 Station Hardware Stability

A GNSS station consists at least of a GNSS receiver, an antenna (including a pre-amplifier), an antenna cable, and indoor cables to connect the receiver to the time and frequency reference. If several receivers have to share an antenna, antenna signal splitters are used in addition. For time and frequency transfer applications, the receiver and time and frequency reference are usually located in air-conditioned laboratories, but the antenna and antenna cable are exposed to outdoor temperature variations. The outdoor temperature variations have long-term components that can introduce frequency offsets in a frequency comparison campaign spanning over several days to weeks by introducing long-term variations in the receiver hardware delays. The temperature stability of the outdoor equipment is therefore a critical aspect for frequency comparisons using GNSS time and frequency transfer.

**GNSS Receivers:** The impact of temperature variations in the receiver environment have been studied e.g. in Fonville et al., 2007; Overney et al., 1997. Large differences between different receiver units have been observed, with sensitivities ranging from a few to hundreds of  $\text{ps K}^{-1}$  for the carrier-phase observations L1 and L2. Furthermore, the temperature variations can impact the carrier-phase and code tracking differently, leading to code-phase inconsistencies.

It is therefore recommended to control the temperature of the receiver environment within 0.1 K (Ray et al., 2005). At PTB, the laboratory room temperature is controlled within 1 K.

**GNSS Antennas:** A few studies concerning the temperature sensitivity of GNSS antennas have been performed. The GNSS antenna consists of the antenna element, a low noise pre-amplifier and an antenna body, e.g. a choke ring. The temperature coefficient of the pre-amplifier can be studied by putting it in a climate chamber,

whereas the testing of the antenna element is more challenging, because it can not easily be done in a controlled environment. In Rieck et al., 2003 the temperature coefficient of an amplifier of an Ashtech Choke Ring antenna was found to be less than  $0.2 \text{ ps K}^{-1}$ .

To study the antenna element, the estimated receiver clock error can be compared with the outdoor temperature if a sufficiently stable oscillator is used as time and frequency reference and possible drifts are removed from the clock solution. This approach was used in Ray et al., 2001 and lead to an upper limit of  $2 \text{ ps K}^{-1}$  for the temperature sensitivity of a Dorne & Margolin antenna. This approach can only put a limit on short-term (diurnal) temperature induced delay variations, due to the removal of drifts from the clock solution. An upper limit for the long-term component of the temperature sensitivity of  $10 \text{ ps K}^{-1}$  was later found in Ray et al., 2003. One option to reduce the hardware delay variations due to the antenna is to use temperature-stabilized antennas (TSAs) (Lewandowski et al., 1997).

**Antenna Cables:** Temperature variations can impact the delay of a cable by causing thermal expansion and by changing the dielectric constant of the used dielectric. The effect of temperature variations therefore depends on the cable length that is exposed to the temperature variations, as well as its dielectric. Common dielectrics of cables that are used as antenna cables, are solid polyethylene (PE) and PE foam. The temperature coefficient for a solid PE cable is in the order of several tenth of  $\text{ps K}^{-1} \text{ m}^{-1}$ , e. g.  $-0.42 \text{ ps K}^{-1} \text{ m}^{-1}$  for the RG-58 cable (Overney et al., 1997). Much smaller temperature coefficients are observed in cables using a PE foam dielectric, e. g. Andrew's FSJ1-50A HELIAX™-type cable has a temperature coefficient of  $0.02 \text{ ps K}^{-1} \text{ m}^{-1}$  (Powers et al., 1998).

It is recommended to use an antenna cable with a temperature coefficient of around  $0.01 \text{ ps K}^{-1} \text{ m}^{-1}$  and to keep the part of the cable that is exposed to the outdoor temperature variations as short as possible.

Name	T&F Reference	Receiver	Antenna
PTBB	UTC(PTB)	Ashtech Z-XII <sub>3</sub> T	ASH700936E SNOW
PTBG	UTC(PTB)	Ashtech Z-XII <sub>3</sub> T	ASH701945E_M SNOW
PT10	UTC(PTB)	Dicom GTR51	NAX <sub>3</sub> G+C
KOP1	AHM H9	Septentrio PolaRx4TR	NOV750.R4 NOVS

Table 4: GNSS stations at PTB used in this work.

### 3.2 Local Common-Clock Baselines

In order to characterize the true GPS link instability, the time and frequency references should not add additional noise to the time and frequency comparison. This can be achieved by using the same clock as a reference (common-clock), which is often used for studies on local baselines, but poses a challenge for longer baselines, where the time and frequency signal needs to be transferred with a sufficient stability and uninterrupted over long distances. The experimental setup for local common-clock baselines at PTB is depicted in fig. 18. The pulse per second (PPS)

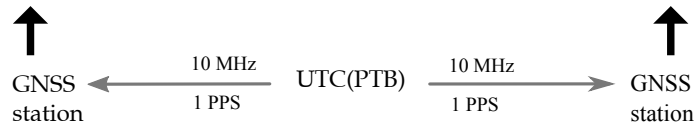


Figure 18: Experimental setup for local common-clock baseline for GPS link characterizations. Two GPS receivers are connected to the same time and frequency reference UTC(PTB) that provides a PPS and a 10 MHz signal.

and 10 MHz signals that serve as the time and frequency reference are split using pulse and frequency distribution amplifiers. The cables from the distribution amplifiers to the receivers are kept as short as possible.

The very short common-clock baseline between the GPS stations PTBB and PTBG of only a few meters was used before to characterize and compare GPS time and frequency transfer methods (e. g. Droste et al., 2015; Petit et al., 2016). The PTBB station is part of the IGS network and is used for GPS time and frequency comparisons contributing to the computation of TAI. In this work, further characterizations are performed, especially concerning the temperature sensitivity of the stations, to study their suitability for frequency comparisons of optical clocks.

In tab. 4 the details of the GNSS stations used in this work are summarized.

#### 3.2.1 Long-term Code-CV Analysis

In order to study the long-term stability of the GPS stations at PTB a Code-CV analysis was performed using software developed by the author based on the CGGTTS data format (Allan et al., 1994) and the broadcasted satellite orbit and clock information. A Code-CV analysis based on the ionosphere-free linear combination between three stations at PTB is presented in fig. 20 for a period of one year. Daily averages of the time difference between the stations are shown together with the daily mean outdoor temperature at PTB. The temperature sensor and the GPS stations are located at the rooftop of the Kopfermann building at PTB (fig. 19). A robust outlier detection algorithm based on the median absolute deviation (Mosteller et al., 1977) is applied to the receiver clock errors reported in the CGGTTS files. Days on which data from one station is only partly available, e. g. due to maintenance, have been removed from this analysis.





Figure 19: GNSS installations on the rooftop of the Kopfermann building at PTB.

The two common-clock baselines including PTBB show a visible correlation with the outdoor temperature. The Pearson correlation coefficient between the time difference and the outdoor temperature is 0.8 for the PTBG-PTBB baseline and only 0.2 for the PT10-PTBG baseline. This analysis is only able to determine relative temperature coefficients of the stations. All stations are exposed to the same outdoor temperature variations, therefore undetectable common-mode effects are possible. The temperature coefficient of PTBB relative to the other stations is  $(51 \pm 2) \text{ ps K}^{-1}$  for the link with PTBG, and  $(60 \pm 2) \text{ ps K}^{-1}$  for the link with PT10, as determined by taking the slope of a linear fit to the time difference over the outdoor temperature. The temperature coefficient of the link between PTBG and PT10 is only  $(7 \pm 1) \text{ ps K}^{-1}$ .

The most likely explanation for this large difference in the temperature coefficients of the stations is the antenna cable of PTBB, which is a cable of type RG-214 with a solid PE dielectric. The other stations use antenna cables with PE foam as dielectric that typically have a 10 times lower temperature sensitivity. The frequency instability of the GPS links are shown in fig. 21. The MDEV reaches a flicker floor of  $4 \times 10^{-17}$  for links including the PTBB station, the MDEV for the PT10-PTBG baseline reaches  $2 \times 10^{-17}$  for an averaging time of  $5 \times 10^6 \text{ s}$  and is dominated by FPM.

### 3.2.2 PPP and IPPP Analysis

In Petit et al., 2016, the very short baseline between PTBB and PTBG was used to demonstrate the improved instability of the IPPP technique compared to the standard PPP technique over a period of 95 d. An decrease of the instability for averaging times above 0.5 d was observed with an improvement of 30% for averaging times above 3.5 d.

The PPP and IPPP link results<sup>1</sup> from this 95 d period will be used in this work to investigate the effect of the relative temperature coefficients between the stations on the PPP and IPPP link instability.

The PPP clock solutions were calculated according to the standard PPP processing for TAI with the NRCan PPP software in continuous processing mode with batch

<sup>1</sup> The PPP and IPPP results processed by A. Kanj haven been kindly provided by G. Petit.

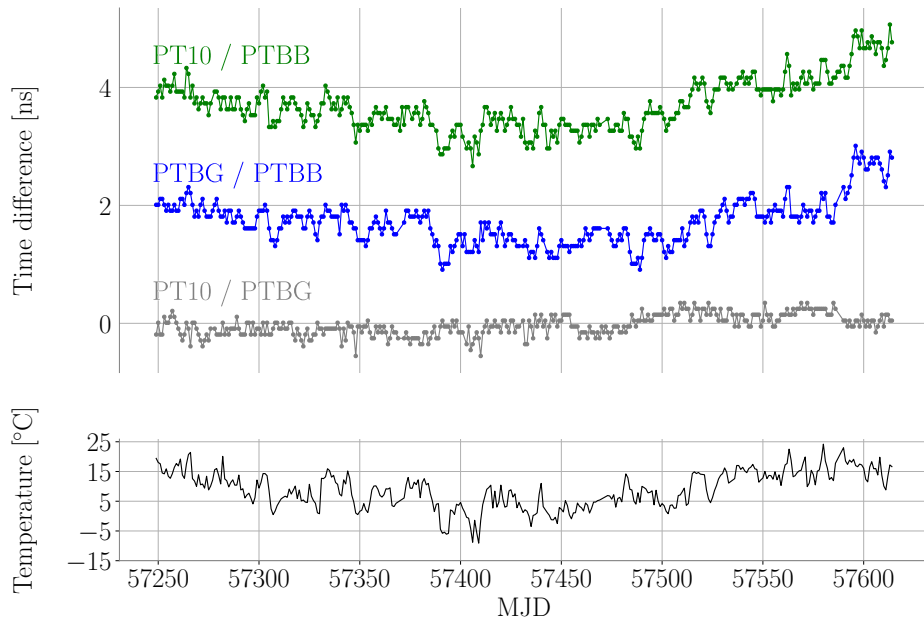


Figure 20: Daily mean time difference for Code-CV analysis of local common-clock baselines at PTB between stations PTBB, PTBG, and PT10 (upper) and daily mean outdoor temperature at PTB (lower). A time offset of 2 ns for the PTBG-PTBB baseline and 4 ns for the PT10-PTBB baseline was introduced for better visibility.

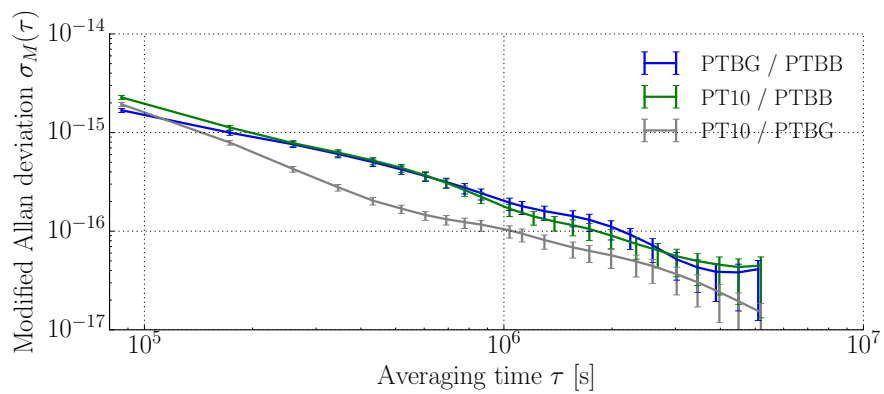


Figure 21: MDEV for long-term Code-CV analysis of common-clock baselines at PTB.

lengths of up to 40 d using IGS rapid products (300 s clock products) based on the ionosphere-free linear combination. An elevation cutoff of  $10^\circ$  was applied and the  $z_{wd}$  was modeled as random walk constrained with  $3 \text{ mm}/\sqrt{h}$  using the VMF1 mapping function. The IPPP clock solutions were calculated using the GINS software with GRG satellite products. An elevation cutoff of  $10^\circ$  was applied and the tropospheric  $z_{wd}$  was estimated every two hours. The link formation algorithm described in sec. 2.6.4 was applied.

The time difference for the PPP and IPPP link are depicted in fig. 22 together with the outdoor temperature (recorded every 15 min) and time difference that have been temperature corrected. For the temperature correction, the relative temperature coefficient was determined by a linear fit to the time difference over the outdoor temperature. During the first 15 d large sub-daily temperature variations are observed in the recorded outdoor temperature that are not present in the GPS link data. The temperature data was therefore smoothed using a running average with an averaging window of one day, in order to avoid the introduction of this high frequency fluctuations into the temperature corrected time difference. A drawback of this smoothing is that some sub-daily hardware delay variations that are present in the PPP and IPPP clock solution do not get corrected, and an improvement can only be expected for the long-term stability. The temperature recorded by the outdoor sensor does not necessarily represent the temperature variations integrated along the antenna cable, e.g. because several meters of the antenna cable of the PTBB station are routed under the rooftop of the building. That might explain some of the discrepancies on the sub-daily level between the recorded outdoor temperature and the GPS links.

The relative temperature coefficient for this baseline is  $(16.0 \pm 0.1) \text{ ps K}^{-1}$  for both PPP and IPPP. This temperature coefficient is close to the diurnal temperature coefficient for PTBB of  $(-13.1 \pm 0.5) \text{ ps K}^{-1}$  observed in Weinbach, 2013, based on a PPP clock solution relative to IGST.

The MDEV for the original and the temperature corrected PPP and IPPP links on the PTBB-PTBG common-clock baseline is shown in fig. 23. With the temperature correction, both the PPP and the IPPP link instabilities improve for averaging times above 1 d, but the IPPP profits even more and is at least 43% smaller for averaging times above 3.5 d compared to the PPP link. The temperature corrected IPPP link reaches an instability of  $1.6 \times 10^{-17}$  for an averaging time of  $1.4 \times 10^6 \text{ s}$ , and no systematic frequency offset is observed, whereas the frequency instability of the temperature corrected PPP link hits a flicker floor of  $6.1 \times 10^{-17}$ .

While it was reported that the carrier-phase observations are less sensitive to hardware delay variations due to temperature effects than code observations and the temperature coefficient for the PPP and IPPP links is in fact smaller than the coefficient for the Code-CV analysis, this example shows that IPPP links can still suffer from systematic frequency offsets due to long-term temperature induced hardware delay variations. If during a frequency comparison campaign that lasts 10 d, the mean daily temperature raises e.g. by 10 K, a temperature coefficient of  $16 \text{ ps K}^{-1}$  would lead to a fractional frequency offset of  $2 \times 10^{-16}$ . To fully profit from the improved instability of the IPPP technique for long averaging times, a good station hardware instability is required, ideally with a temperature coefficient of not more than a few  $\text{ps K}^{-1}$  for the outdoor equipment.

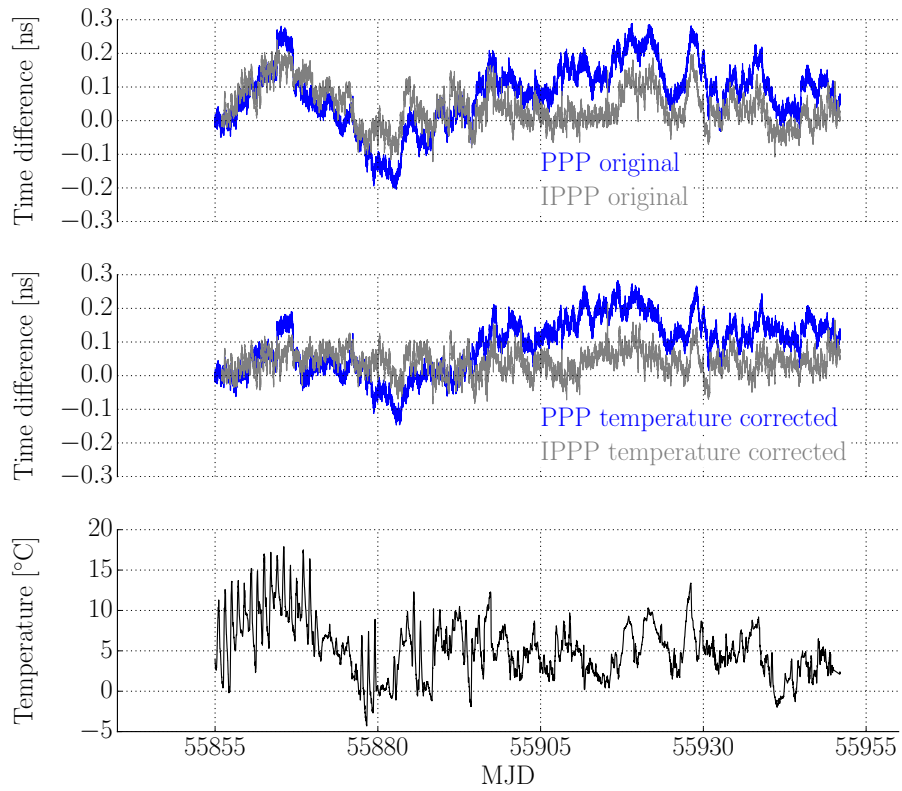


Figure 22: Time difference for PPP and IPPP clock solutions for a local common-clock baseline at PTB between stations PTBB and PTBG (upper), with temperature correction (middle) and the outdoor temperature at PTB (lower). The uncorrected PPP and IPPP data was published in Petit et al., 2016.

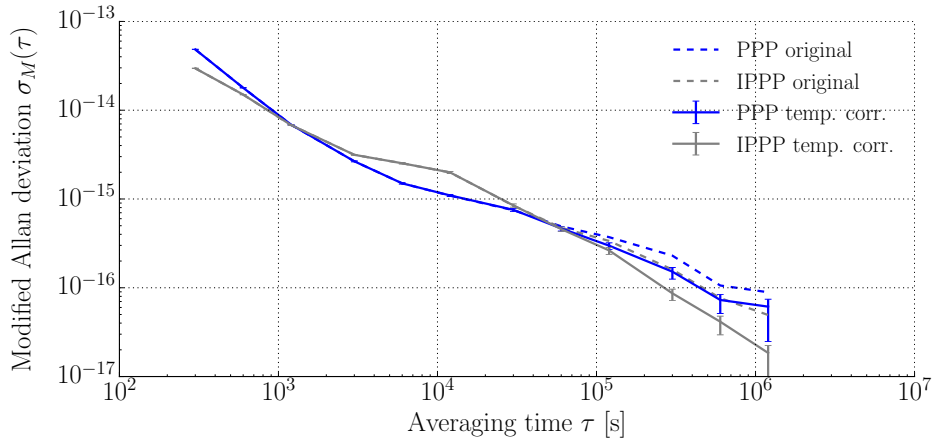


Figure 23: MDEV for PPP and IPPP links for a local common-clock baselines at PTB between stations PTBB and PTBG with temperature correction and for the uncorrected links. The uncorrected PPP and IPPP data was published in Petit et al., 2016.

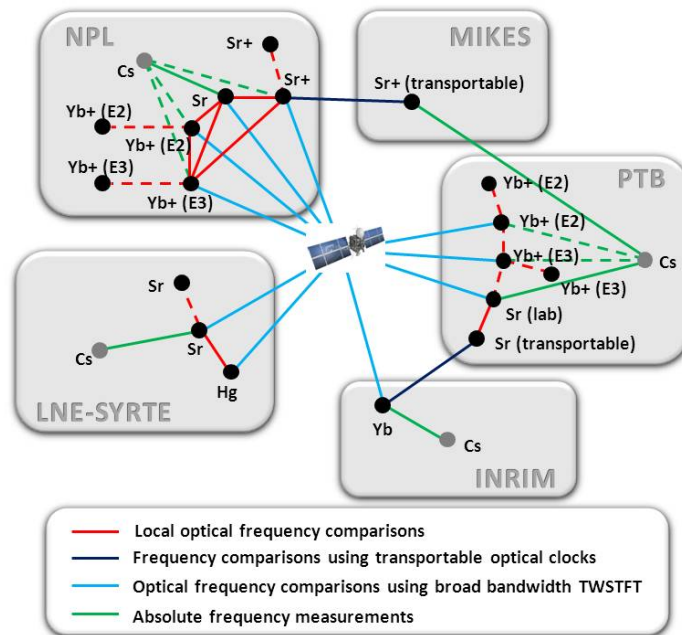


Figure 24: Frequency standards developed at the European NMIs involved in the ITOC measurement campaigns (from Margolis et al., 2013).

### 3.3 Continental Baselines

On local baselines some common mode errors cancel out. The GNSS signals travel on almost identical paths through the atmosphere and the local environment, especially the outdoor temperature, is the same for both stations. The performance of the GPS time and frequency transfer techniques on local baselines can not easily be extrapolated to longer baselines. It is therefore of interest to study the difference in performance between the PPP and IPPP technique on longer baselines.

#### 3.3.1 International Timescales with Optical Clocks (ITOC)

The ITOC project is a collaborative European project that aims at removing the obstacles for the redefinition of the SI second based on optical atomic clocks (Margolis et al., 2013). An important step towards the redefinition of the SI second based on optical clocks is the validation of their uncertainty budgets. Comparisons between optical clocks developed at different NMIs will help to verify those budgets.

Within this project, direct remote comparisons of optical clocks developed at European NMIs using microwave techniques, TWSTFT and GPS time and frequency transfer, were carried out. The involved institutes are Physikalisch-Technische Bundesanstalt (PTB) in Germany, National Physical Laboratory (NPL) in the United Kingdom, Laboratoire national de métrologie et d'essais - Système de Références Temps-Espace (LNE-SYRTE) in France and Istituto Nazionale di Ricerca Metrologica (INRIM) in Italy.

Two measurement campaigns took place, the first in autumn 2014 from Modified Julian Date (MJD) 56951 to 56960, and the second in July 2015 from MJD 57177 to 57202. During the first campaign only the  $\text{Yb}^+$  ion clocks at NPL and PTB were operated, during the second campaign Sr lattice clocks at LNE-SYRTE, PTB and NPL were operated additionally.

NMI	Name	T&F Reference	Receiver	Antenna
INRIM	INR3	AHM HM3	TPS E_GGD	Javad choke ring
LNE-SYRTE	OPMT	AHM H889	Ashtech Z-XII3T	3S-02-TSADM
LNE-SYRTE	OPM8	AHM H889	Septentrio PolaRx4TR	ASH701945E_M
NPL	NP11	AHM HM2	Dicom GTR50	NOV702
PTB	KOP1	AHM H9	Septentrio PolaRx4TR	NOV750.R4 NOVS

Table 5: GNSS stations at European NMIs used in this work.

In this work, PPP and IPPP analysis will be carried out for all GPS baselines between PTB, NPL, LNE-SYRTE and INRIM. The suitability of these techniques for the frequency comparisons of optical clocks will be studied.

In tab. 5 the details of the GNSS stations involved in this campaigns are summarized. At PTB a new dedicated GNSS station (KOP1) was installed, using state-of-the-art equipment to minimize the impact of temperature induced hardware delay variations on the frequency comparison results. This station was referenced directly to the AHM H9 instead of UTC(PTB), because the optical clocks at PTB are compared to the AHM H9 as well.

The NRCan software is used for continuous and daily batch PPP processing with final IGS 30s satellite clock products. An elevation cutoff of  $10^\circ$  is applied and the tropospheric  $zwd$  is constrained with  $5 \text{ mm}/\sqrt{h}$ . The Kalman filter backward substitution is used. The GINS software with GRG satellite products is used for IPPP processing. An elevation cutoff of  $10^\circ$  is applied and the tropospheric  $zwd$  is estimated every hour (every 30 min for all links with INRIM and the links with LNE-SYRTE using the OPM8 station). The link formation algorithm described in sec. 2.6.4 was used. IGS antenna corrections are used for PPP and IPPP processing.

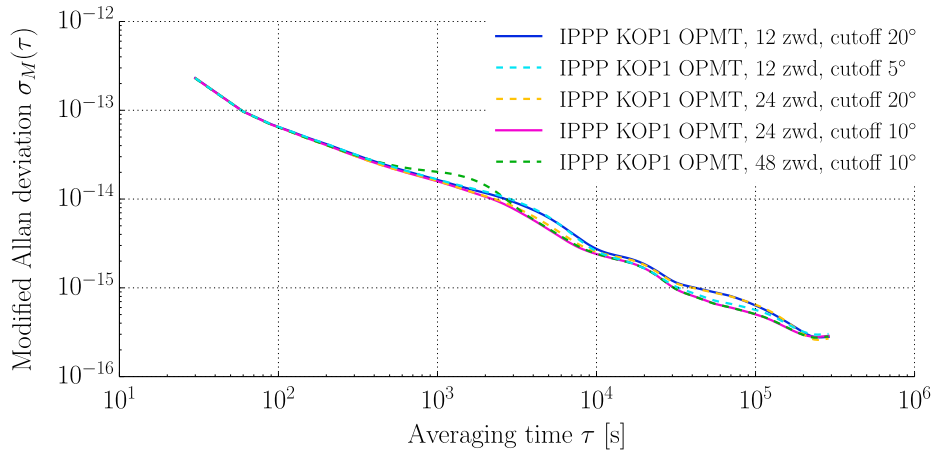


Figure 25: Impact of the number of estimated tropospheric  $zwd$  parameters and the elevation cutoff on the IPPP frequency instability for the PTB-LNE-SYRTE baseline. Results for 12, 24, and 48  $zwd$  parameters per day are shown for an elevation cutoff of  $5^\circ$ ,  $10^\circ$  or  $20^\circ$ .

The parameters for the IPPP processing were chosen based on a small study of the impact of the number of tropospheric  $zwd$  parameters and the elevation cutoff on the instability of the IPPP link on the PTB-LNE-SYRTE baseline. The results are shown in fig. 25 for 12, 24, and 48  $zwd$  parameters per day and elevation cutoffs of  $5^\circ$ ,  $10^\circ$  or  $20^\circ$ . The choice of the number of  $zwd$  parameters impacts the instabil-

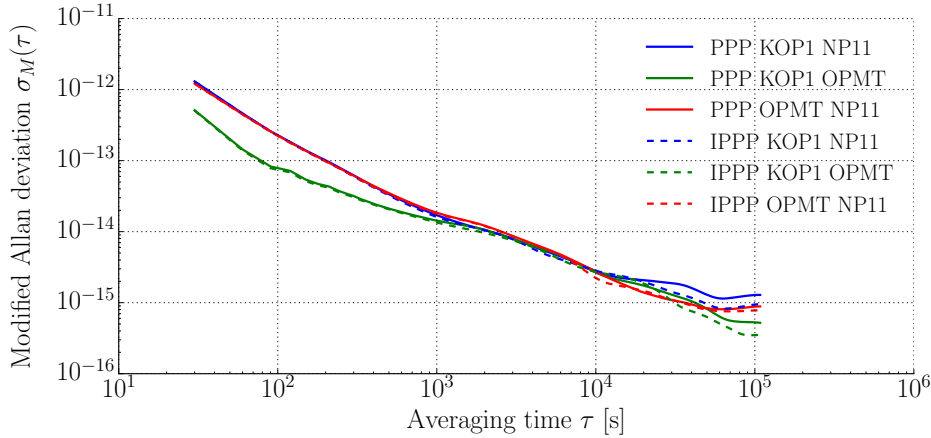


Figure 26: PPP and IPPP frequency instability for the European baselines between LNE-SYRTE, NPL and PTB.

ity for averaging times up to  $10^4$  s, the smallest instability is observed for 24  $z_{wd}$  parameters per day (one per hour). The choice of the elevation cutoff impacts the instability for averaging times above  $10^4$  s. For low satellite elevation angles the accuracy and the signal-to-noise ratio degrades, but on the other hand the correlation between the receiver clock error and the  $z_{wd}$  can be reduced by the inclusion of low elevation observations (Dach et al., 2003; Rothacher et al., 1998). For the IPPP link on the PTB-LNE-SYRTE baseline the lowest instability is observed for a cutoff of  $10^\circ$ , for an averaging time of 1 d the instability is 24 % smaller compared to the instability with a  $20^\circ$  cutoff.

### 3.3.1.1 2014 Measurement Campaign

In tab. 6 the results of the AHM comparisons via continuous PPP and IPPP links are summarized. The average fractional frequency differences between the AHMs are of minor importance, of interest are the differences between both techniques.

Link	PPP [ $10^{-13}$ ]	IPPP [ $10^{-13}$ ]	Difference [ $10^{-16}$ ]
KOP1-NP11	0.398 64	0.399 54	0.90
KOP1-OPMT	-2.162 34	-2.161 49	0.85
OPMT-NP11	-2.560 98	-2.561 04	0.06

Table 6: Average fractional frequency differences ( $\Pi$ -averaging) for AHMs comparisons via continuous PPP and IPPP links (MJD 56951-56960) for baselines between European NMIs.

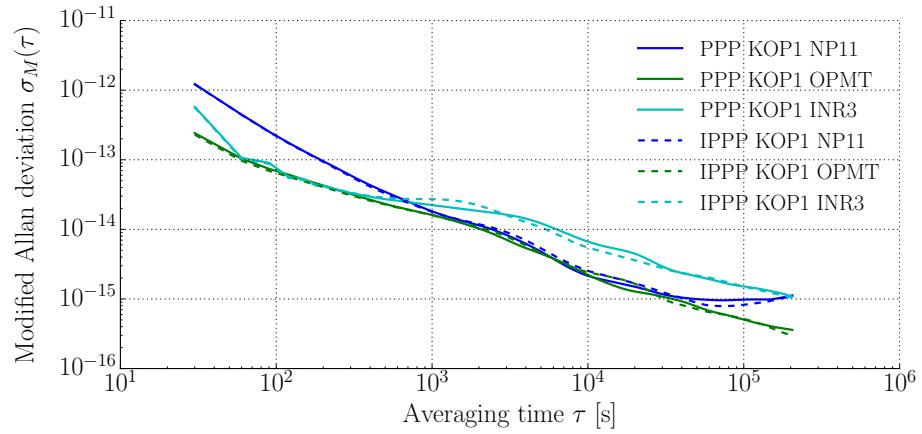
For the measurement campaign in 2014, the difference between the average fractional frequency differences of the PPP and IPPP is below  $1.0 \times 10^{-16}$  for all baselines for a measurement time of 10 d. The instabilities for the PPP and IPPP links on the three baselines are plotted in fig. 26. The increased short-term instability up to  $10^3$  s averaging time of the links with NPL,  $1.3 \times 10^{-12}$  vs.  $5 \times 10^{-13}$  for other GPS links for an averaging time of 30 s, is caused by the instability of the GPS receiver (DICOM GTR50) used in the NP11 station that contains a time interval counter that adds short-term noise dominated by WPM.

Link	PPP [ $10^{-13}$ ]	IPPP [ $10^{-13}$ ]	Difference [ $10^{-16}$ ]
KOP1-NP11	-0.752 26	-0.750 60	1.66
KOP1-OPMT	2.000 09	2.005 65	5.56
OPMT-NP11	-2.752 35	-2.756 25	3.90
KOP1-INR3	4.858 05	4.859 42	1.37
OPMT-INR3	2.857 95	2.853 65	4.30
INR3-NP11	-5.610 31	-5.609 83	0.47

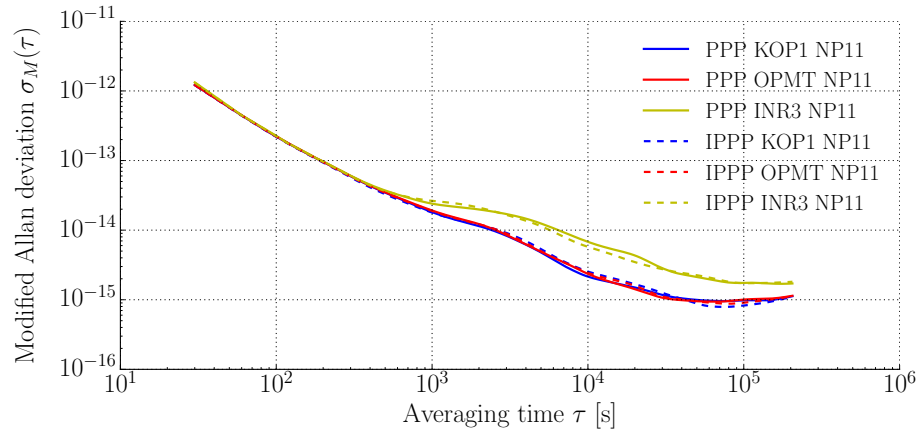
Table 7: Average fractional frequency deviations ( $\Pi$ -averaging) of the AHM comparison via PPP and IPPP links (MJD 57 177-57 196) for baselines between European NMIs.

### 3.3.1.2 2015 Measurement Campaign

In tab. 6 the results of the AHMs comparisons via continuous PPP and IPPP links are summarized. The agreement between the PPP and IPPP technique for the links between PTB, NPL and INRIM is similar to what was observed in the 2014 campaign (below  $2 \times 10^{-16}$  for a measurement time of 20d), but the links with LNE-SYRTE show differences in the average fractional frequency differences of up to  $6 \times 10^{-16}$ .

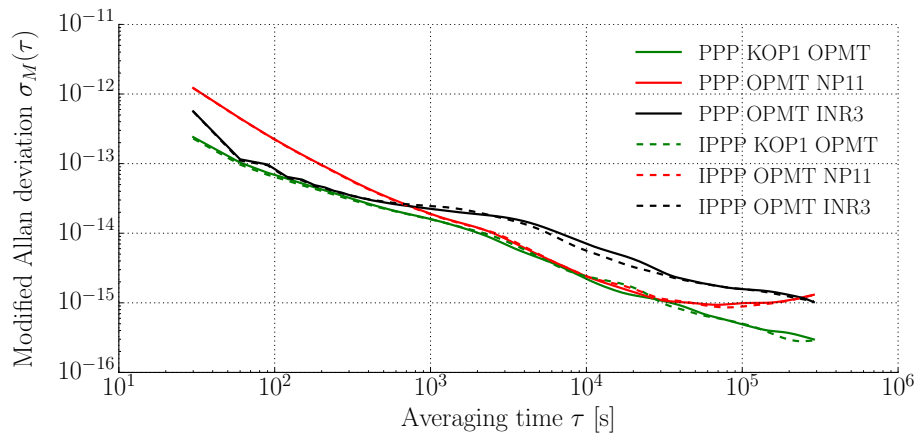


(a) PTB links

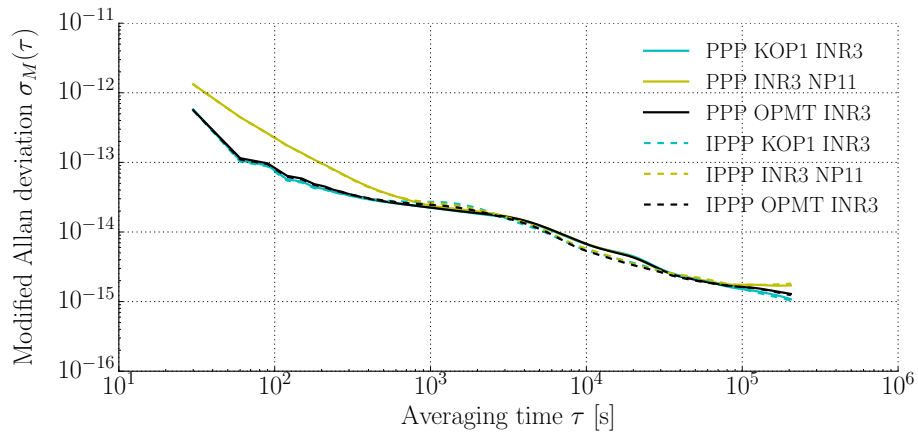


(b) NPL links





(c) LNE-SYRTE links



(d) INRIM links

Figure 27: Frequency instability for PPP and IPPP links on continental baselines between four European NMIs.

The frequency instability of the links during the 2015 measurement campaign are depicted in fig. 27. Differences in the short-term instability are again explained by the different hardware instabilities of the receivers used at the stations and the long-term instability is dominated by the AHMs, e.g. all links with NPL show a flicker floor of  $1 \times 10^{-15}$  for averaging times above 0.5 d. The instability of the PPP and IPPP links is comparable, which is expected, because the improved instability of the IPPP link for long averaging times is concealed by the instabilities of the AHMs. Small differences between the instability of the PPP and IPPP links might be explained by differences in the observation modeling and the parameter adjustment algorithm, the instability between  $10^3$  s to  $10^4$  s is especially sensitive to the troposphere modeling. The increased medium-term instability in the links with INRIM are possibly caused by temperature induced hardware delay variations in the antenna cable. Interestingly, the lowest long-term instability is observed for the PTB-LNE-SYRTE link ( $4 \times 10^{-16}$  at  $2 \times 10^5$  s averaging time) for both the PPP and IPPP link, even though both techniques do not agree about the average fractional frequency difference of the AHMs (tab. 7). This matter will be investigated in the next section.

### 3.3.2 PTB-LNE-SYRTE Baseline

One approach to validate continuous batch PPP solutions is to compare them to daily batch PPP solutions, similar to a geodetic repeatability test. In fig. 28 the time difference for the AHM comparison between LNE-SYRTE and PTB using continuous batch and daily batch PPP, IPPP and Code-CV are shown. The ionosphere-free Code-

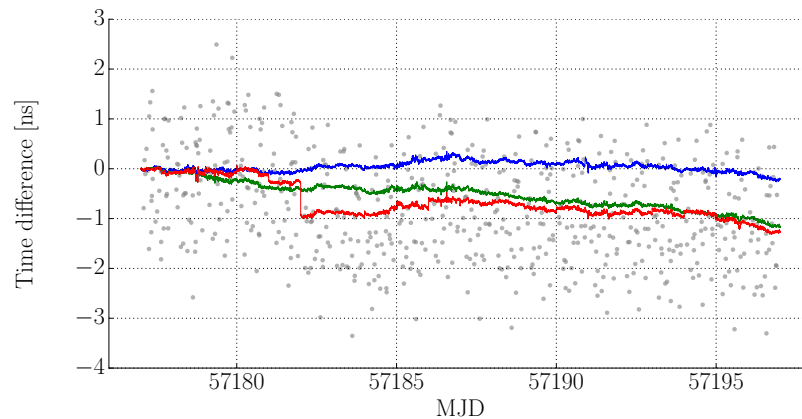


Figure 28: Time difference for AHM comparison with PTB station KOP1 and LNE-SYRTE station OPMT via continuous batch PPP (green), daily PPP (red), IPPP (blue) and Code-CV (grey dots). The same frequency offset has been removed from all results. A large day boundary jump of  $\approx 0.6$  ns is observed between MJD 57 181 and 57 182.

CV analysis shows daily averages for individual satellites with an elevation cutoff of  $30^\circ$ . A large day-boundary jump of  $\approx 0.6$  ns is observed between MJD 57 181 and 57 182, which hints to a code-phase inconsistency (see discussion in subsec. 2.5.2). The daily PPP solutions follow the mean Code-CV results from day to day as expected, while the continuous batch PPP solution follows the Code-CV solution via a long-term drift over several days and the IPPP solution seems to be less affected by the event around MJD 57 181.

The Wide-lane receiver bias (WRB), a byproduct of the IPPP processing, is a noisy detector of code-phase inconsistencies, because it is a linear combination of the WL phase receiver biases and the NL code receiver biases (subsec. 2.6.2). In fig. 29

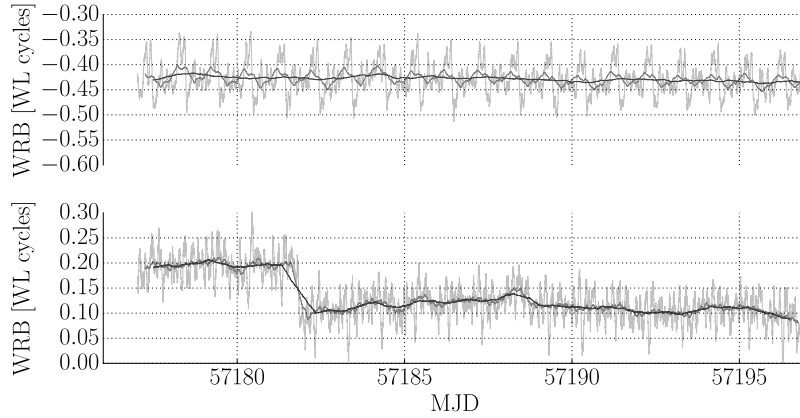


Figure 29: WRB for OPMT (bottom) and KOP<sub>1</sub> (top) station (running averages with window size 1 h, 12 h and 1 d from light to dark grey). A permanent step of 0.1 WL cycles in the WRB of the OPMT station is observed on MJD 57181.

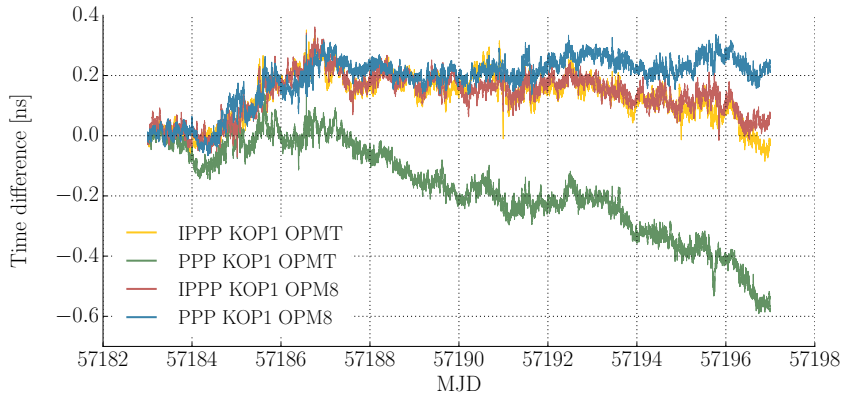


Figure 30: Time difference for PPP and IPPP AHM comparisons between PTB and LNE-SYRTE using two different stations at LNE-SYRTE: OPMT and OPM8. The same frequency offset has been removed from all results.

the WRB for the OPMT station and KOP<sub>1</sub> station during the 2015 measurement campaign are shown. A permanent step of 0.1 WL cycles ( $\approx 0.3\text{ns}$ ) is observed on MJD 57181, another hint for a code-phase inconsistency. The step is smaller than the  $0.6\text{ns}$  day boundary jump, which is expected for a frequency-dependent event affecting mainly the code observations like multipath, because the WRB contains the receiver NL hardware biases and the PPP solution is based on the ionosphere-free linear combinations and the corresponding observation weights  $\beta_{1,2}^{\text{NL}} < \beta_{1,2}^{\text{IF}}$  (see sec. 2.1).

Further validation of the results are performed by comparing the PPP and IPPP links between PTB and LNE-SYRTE using the OPMT station to links using an alternative station at LNE-SYRTE, the OPM8 station. Data from this stations is not available during the whole campaign, only starting from MJD 57183. In fig. 30 the time difference from the PPP and IPPP AHM comparison between PTB and LNE-SYRTE are shown, using either the OPMT or the OPM8 station.

For the baseline between PTB and LNE-SYRTE the IPPP and PPP results using the OPM8 station agree better with the IPPP than with the PPP result using OPMT. In fig. 31 the local common-clock results for the OPMT-OPM8 links for continuous batch PPP and IPPP are shown. The feature on MJD 57190 in the IPPP common-clock

link between OPM8 and OPMT is also present in the PTB-LNE-SYRTE IPPP link using OPMT, but not in the PPP links with OPMT, its origin is unclear. The average fractional frequency difference for the OPMT-OPM8 common-clock baseline (MJD 57183-57196) is  $6.7 \times 10^{-16}$  for the PPP link and  $8.5 \times 10^{-17}$  for the IPPP link.

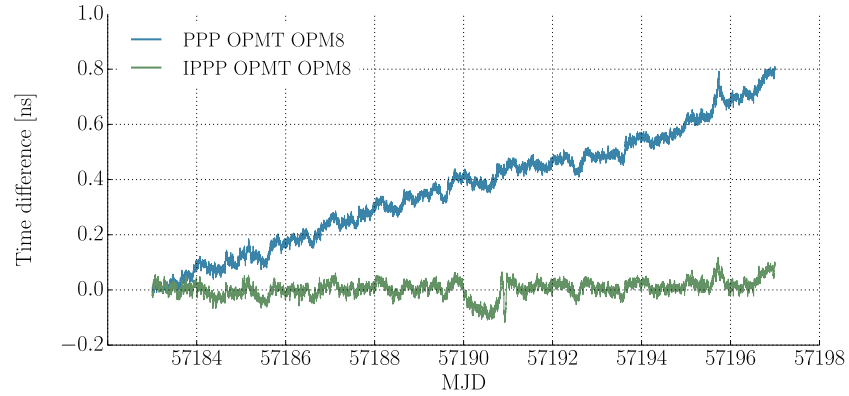


Figure 31: Time difference for PPP and IPPP common clock local baseline at LNE-SYRTE between OPMT and OPM8 station.

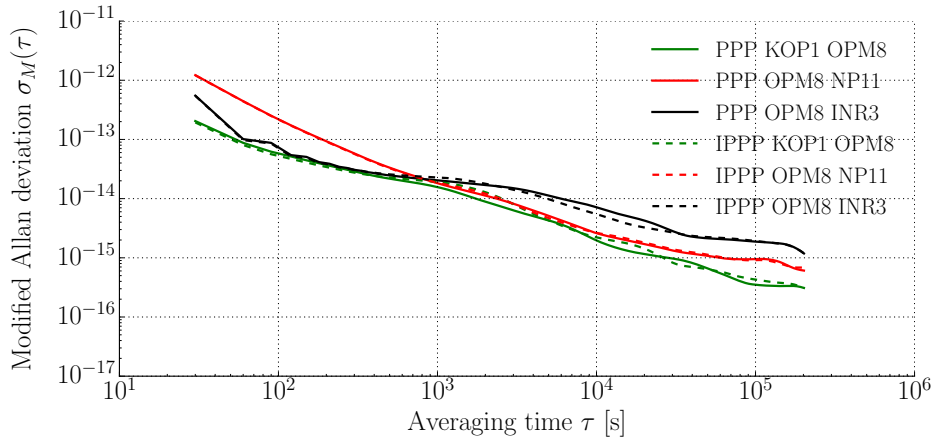


Figure 32: PPP and IPPP frequency stability for European baselines between four European NMIs with alternative LNE-SYRTE station OPM8.

The average fractional frequency differences for all baselines using OPM8 are reported in tab. 8 and the corresponding frequency instabilities are depicted in fig. 32. The agreement between the PPP and IPPP results using OPM8 improves for all baselines and the difference in the fractional frequency difference is similar to what was observed for other European baselines.

### 3.3.3 PTB-NPL Baseline

The PPP and IPPP links between PTB and NPL will be used in this work for the remote comparison of the  $\text{Yb}^+$  ion optical clocks operated at both institutes. A closer look at the GPS links will help to interpret the results of this frequency comparison campaigns.

In fig. 34 and fig. 35 the time difference for the daily and continuous batch PPP and the IPPP link between NPL and PTB during the 2014 and 2015 measurement cam-

Link	PPP [ $10^{-13}$ ]	IPPP [ $10^{-13}$ ]	Difference [ $10^{-16}$ ]
KOP <sub>1</sub> -OPM8	2.006 65	2.005 41	1.24
OPM8-NP <sub>11</sub>	-2.765 06	-2.763 24	1.82
OPM8-INR <sub>3</sub>	2.855 99	2.859 37	3.95

Table 8: AHM frequency comparison ( $\Pi$ -averaging) via PPP and IPPP links with LNE-SYRTE station OPM8 (MJD 57 183-57 196).

paing are shown. The WRB of the NP<sub>11</sub> and KOP<sub>1</sub> station during the campaigns are shown in fig. 33 and fig. 36.

During the 2014 measurement campaign, no large day-boundary discontinuities are observed. During the 2015 measurement campaign on the other hand, two large day boundary jumps of approx. 0.3 ns occur in the daily batch PPP solution, after MJD 57 179 and after MJD 57 187. The large day-boundary jump after MJD 57 187 is accompanied by a feature in the WRB of the NP<sub>11</sub> station (approx. 0.05 WL cycles) and might be caused by a coincident rise of the indoor temperature of 2 °C at NPL (fig. 36). The first large day-boundary discontinuity, while also associated with a rise in temperature of 1 °C at NPL does not lead to a detectable feature in the WRB of the NPL station.

In the case of the OPMT station at LNE-SYRTE, a permanent step in the WRB was observed, that was associated with a long-term disagreement between the IPPP solution and the continuous as well as daily batch PPP solutions and the Code-CV solution, between the phase-only technique and all techniques using code observations. In the case of the NP<sub>11</sub> station, a transient feature in the WRB is observed that is associated with a short-term disagreement between the daily batch PPP solution and the IPPP solution, but does not affect the long-term agreement between the daily batch PPP solution and the IPPP solution. Unfortunately, there is a permanent disagreement between the continuous batch PPP and the IPPP solution. In fig. 37 the difference between continuous and daily batch PPP links and the IPPP link is shown. The continuous PPP link without backward smoothing of the Kalman filter agrees better with the IPPP link than the continuous PPP link with backward smoothing enabled. The difference of the average fractional frequency deviations for the continuous batch PPP with backward smoothing and the IPPP link is  $2.6 \times 10^{-16}$  for an averaging time of 27 d. This example of a transient code-phase inconsistency shows that additional smoothing in the form of a continuous PPP solution with Kalman filter backward smoothing, does not just hide station problems, but can lead to long-term systematic frequency offsets even for transient code-phase inconsistencies.

The TDEV of the WRB of the PTB station KOP<sub>1</sub> is 2 ps for an averaging time of one week and 10 ps for the NPL station NP<sub>11</sub>. The new PTB station KOP<sub>1</sub> has the lowest long-term instability of the studied stations, and is therefore a good choice for frequency comparison campaigns spanning several days to weeks. The WRB of the NP<sub>11</sub> and KOP<sub>1</sub> station show sub-daily variations. It is not clear to what extend this variation is due to station-dependent effects, because the GINS software used for IPPP processing uses daily values for the WSB, therefore sub-daily variations of the WSB can be introduced to the WRB estimate.

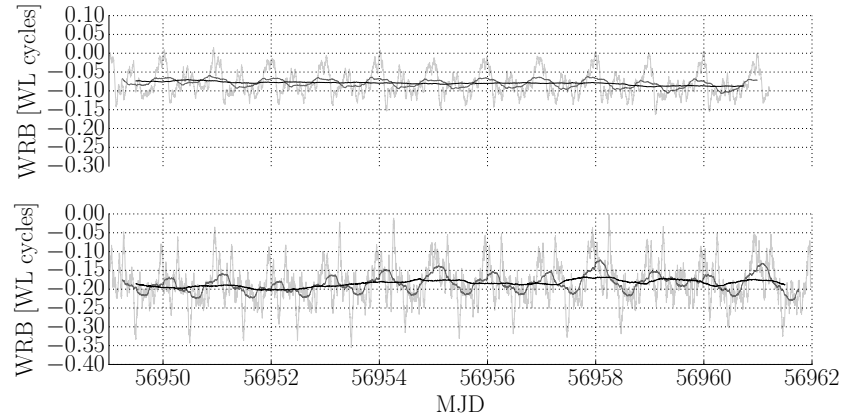


Figure 33: WRB for KOP1 (top) and NP11 (bottom) station during the campaign in 2014 (running averages with window size 1 h, 12 h and 1 d from bright to dark grey).

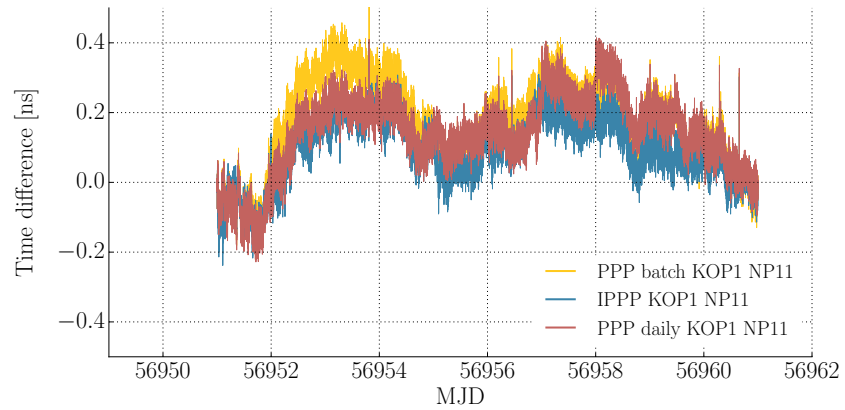


Figure 34: Time difference for the GPS links on the NPL-PTB baseline during the 2014 measurement campaign. A continuous batch PPP and a daily batch PPP link are shown together with the IPPP link. The same frequency offset has been removed from all results.

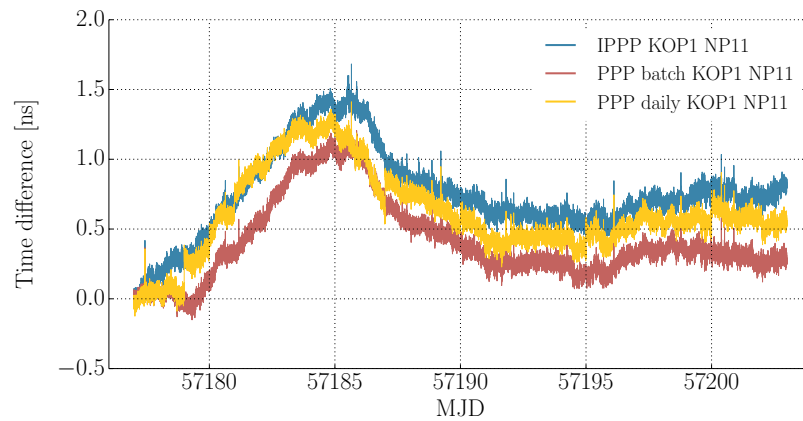


Figure 35: Time difference for the GPS links between NPL and PTB during the 2015 measurement campaign. A continuous batch PPP link with backward smoothing and a daily batch PPP link are shown together with the IPPP link. The same frequency offset has been removed from all results.

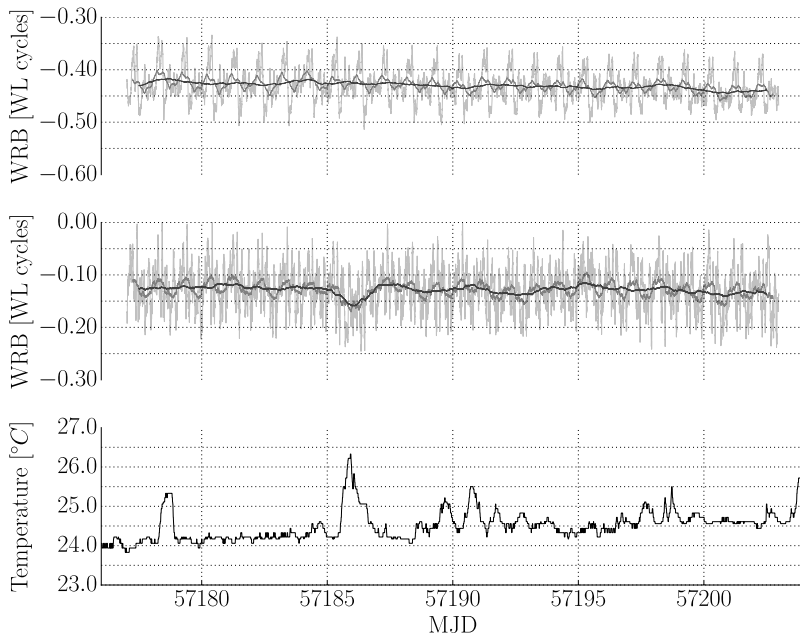


Figure 36: WRB for KOP1 (top) and NP11 (middle) station during the campaign in 2015 (running averages with window size 1h, 12h and 1d from light to dark grey). The bottom plot shows the indoor temperature at NPL.

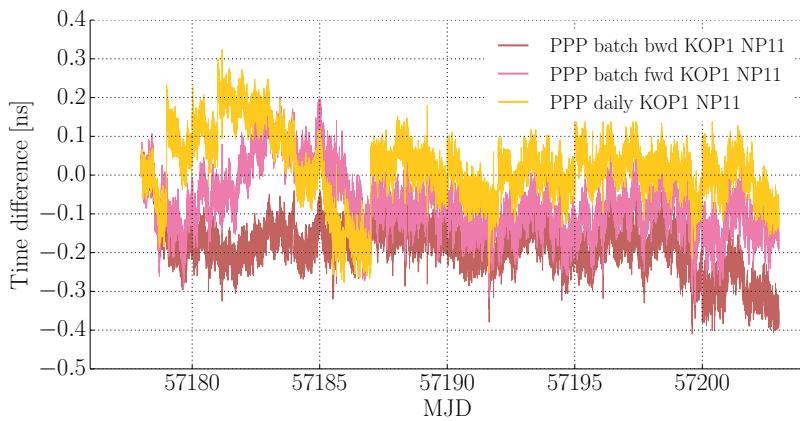


Figure 37: Difference between the PPP links and the IPPP link on the NPL-PTB baseline during the 2015 measurement campaign. Continuous batch PPP links with backward smoothing (batch bwd) and without backward smoothing (batch fwd) and a daily batch PPP link are shown.

### 3.4 Fiber Link Comparison on the PTB-LNE-SYRTE Baseline

Optical fiber links allow for the comparisons of frequency standards with an instability of  $1 \times 10^{-15}$  for an average time of 1 s and down to a few  $10^{-19}$  for long averaging times over continental distances (Lopez et al., 2012; Predehl et al., 2012). In a comparison between an optical fiber link of this quality and a GPS link, the optical fiber link can be considered the ground truth and can be used as a testbed for GPS link characterizations.

In 2014 the fiber link between PTB and Max Planck Institute for Quantum Optics (MPQ) was used to characterize a PPP link between the institutes (Droste et al., 2015). The reported difference of the average fractional frequency deviation was  $(2.1 \pm 6.0) \times 10^{-16}$  between the PPP and the optical fiber link.

In Petit et al., 2016 an 420 km fiber link between Astrogodynamic Observatory (AOS) in Borowiec and Central Office of Measures (GUM) in Warsaw (Śliwczyński et al., 2013) was used to characterize PPP and IPPP links between the institutes. With a measurement time of 41 d, the reported instability of the IPPP link is at least twice as good for averaging times above 2 d and reaches  $1 \times 10^{-16}$  at an averaging time of 6 d, whereas the PPP link reaches a flicker floor of a few  $10^{-16}$ . The average fractional frequency difference between the GPS link and the fiber link was  $-5 \times 10^{-17}$  for IPPP and  $-1.0 \times 10^{-16}$  for PPP.

In the meantime, a 1415 km optical fiber link connecting PTB with LNE-SYRTE over a connection point in Strasbourg has been established. The details of this optical fiber link are described in Chiodo et al., 2015; Lisdat et al., 2016; Raupach et al., 2015. This fiber link will be used in this chapter to characterize the PPP and IPPP links between PTB and LNE-SYRTE during the 2015 ITOC measurement campaign to further validate the results from sec. 3.3.2.

#### 3.4.1 Experimental Setup

The experimental setup for this GPS link characterization is depicted in fig. 38. At both institutes an AHM serves as time and frequency reference for the GPS stations and is linked via an optical femtosecond frequency comb (Diddams et al., 2000) to the ultrastable transfer laser at  $1.5 \mu\text{m}$  of the optical fiber link. At LNE-SYRTE the AHM H889 is used to phase-lock a cryogenic sapphire oscillator (Nand et al., 2011) with a time constant of 1000 s, which is linked to the transfer laser via the optical frequency comb.

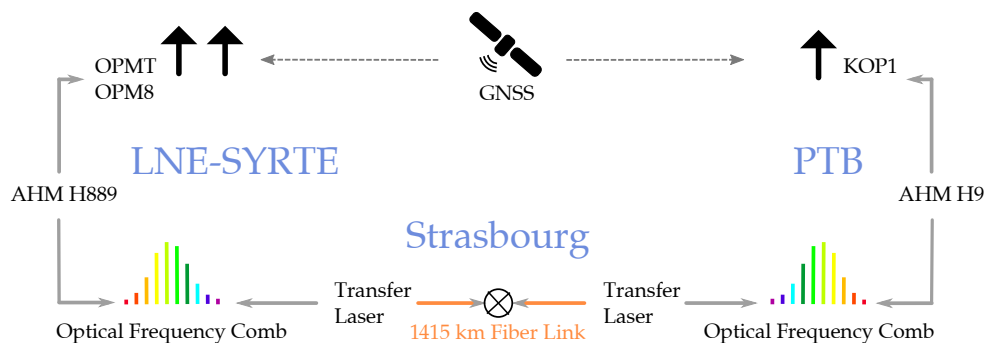


Figure 38: Simplified experimental setup for the characterization of GPS links between LNE-SYRTE and PTB using an optical fiber link. The AHMs H9 and H889 that serve as time and frequency reference for the GPS stations are linked to the transfer lasers of the 1415 km long optical fiber link via optical frequency combs.

For this link characterization, some changes have been applied to the experimental setup at PTB compared to the 2014 measurement campaign with MPQ. Instead



of the PTBB station, which has a large temperature coefficient (see sec. 3.2), a new dedicated station KOP<sub>1</sub> was installed. The GPS stations used in this comparison are described in tab. 5.

Furthermore, the same AHM H<sub>9</sub> that is linked to the transfer laser of the optical fiber link via optical frequency comb, served directly as the time and frequency reference for the GPS station, removing the need for an additional phase comparator measurement between the AHM H<sub>9</sub> and UTC(PTB). While the instability of the phase comparator is significantly smaller than the instability of the PPP link (Droste et al., 2015), it contributed additional dead time due to frequent data outliers.

The AHM and the start point of the optical fiber link are located at different buildings at PTB. During the 2014 AHM comparison campaign, the frequency of the AHM H<sub>9</sub> was transferred via coaxial cable to another building, where it was measured against the transfer laser of the fiber link. In this campaign, two optical femtosecond frequency combs were used, one at each building, and a stabilized fiber replaced the coaxial cable between the buildings.

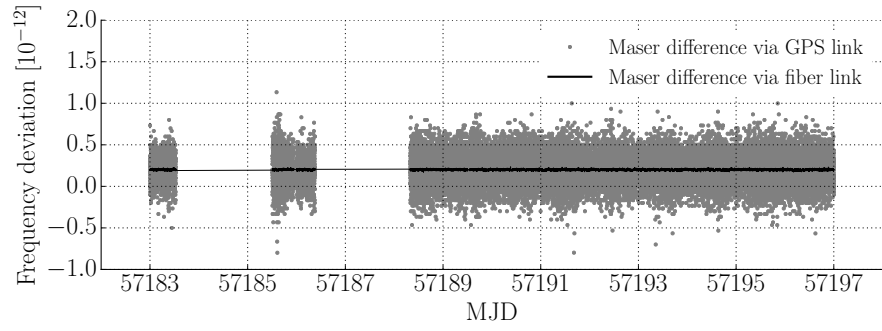
### 3.4.2 Data Analysis

The measurements at PTB, LNE-SYRTE and Strasbourg are combined to obtain the fractional frequency difference between the AHMs H<sub>889</sub> at LNE-SYRTE and H<sub>9</sub> at PTB via optical fiber link on a 1 s grid. The fractional frequency deviations between the AHMs via GPS link are obtained from the phase data that is given on a 30 s grid. To form the double difference between the GPS link and the optical fiber link, the same strategy as in Droste et al., 2015 is applied. For every GPS link average fractional frequency value averaged over a 30 s interval, at least 10 fiber link fractional frequency data points are required from this 30 s period. The instability of the AHMs is approx.  $1 \times 10^{-13}$  for an averaging time of 1 s and the noise contribution from the optical fiber link is negligible. Therefore, averaging at least 10 data points results in a maximum uncertainty of  $3 \times 10^{-14}$ , which is significantly smaller than the instability of the GPS links at 30 s, which is  $2 \times 10^{-13}$ . This approach aims at reducing the effect of the dead time of the optical fiber link on the GPS link characterization. It increases the total measurement time by 3%, but more importantly, it increases the mean length of dead time free segments by a factor of three to 2.5 h and reduces the number of these segments about a factor of three.

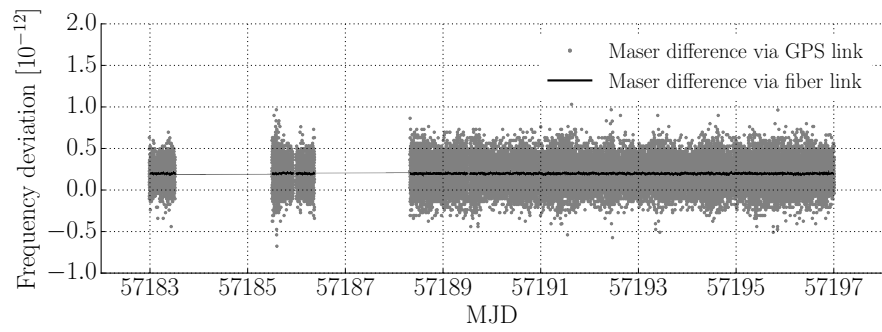
The fractional frequency differences of the double difference are then  $\Pi$ -averaged to obtain the average fractional frequency deviation of the whole measurement period. The uncertainty of the average frequency difference of the double difference is based on the ADEV for an average time of  $\frac{1}{4}T$ , in which T is the total measurement time. The uncertainty is calculated under the assumption of WFM  $u = \sigma_{\lambda}(\frac{1}{4}T)/\sqrt{4}$ .

### 3.4.3 Results and Discussion

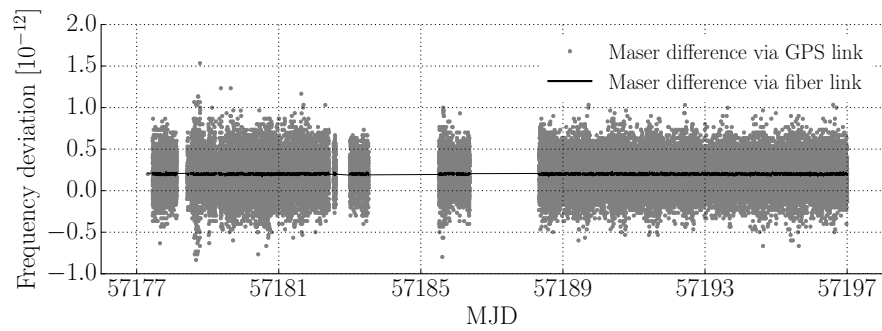
The average fractional frequency deviations of the double difference between the GPS links and the optical fiber link and their uncertainties are summarized in tab. 9. Except for the PPP link using the OPMT station, no systematic frequency offsets are observed and for the IPPP links the average fractional frequency deviations of the double difference are significantly below  $1 \times 10^{-16}$ :  $(-0.34 \pm 2.66) \times 10^{-16}$  for the OPMT station and  $(-0.23 \pm 0.57) \times 10^{-16}$  for the OPM8 station. The comparison with the fiber link confirms the suspicion based on the results from sec. 3.3.2 that the PPP link using OPMT is biased. It has an average fractional frequency deviation of the double difference of  $(-5.94 \pm 2.73) \times 10^{-16}$ , a much better agreement is observed for the PPP link using OPM8 with an average fractional frequency deviation of  $(1.23 \pm 1.07) \times 10^{-16}$  for the double difference.



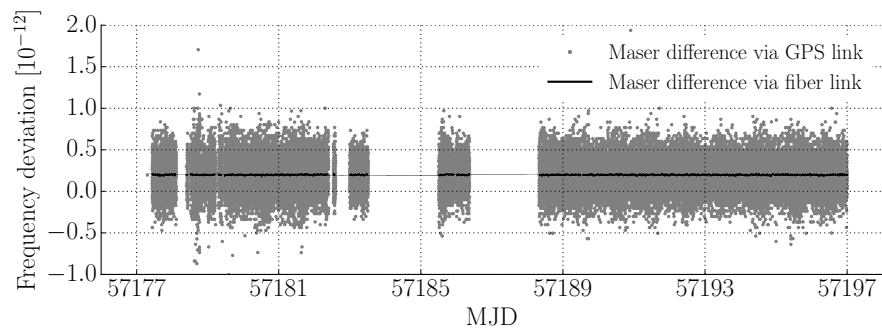
(a) OPM8 PPP



(b) OPM8 IPPP



(c) OPMT PPP



(d) OPMT IPPP

Figure 39: Fractional frequency deviations of the AHM comparison via GPS link and optical fiber link between LNE-SYRTE and PTB for PPP and IPPP links using two different GPS stations at LNE-SYRTE, OPMT and OPM8.

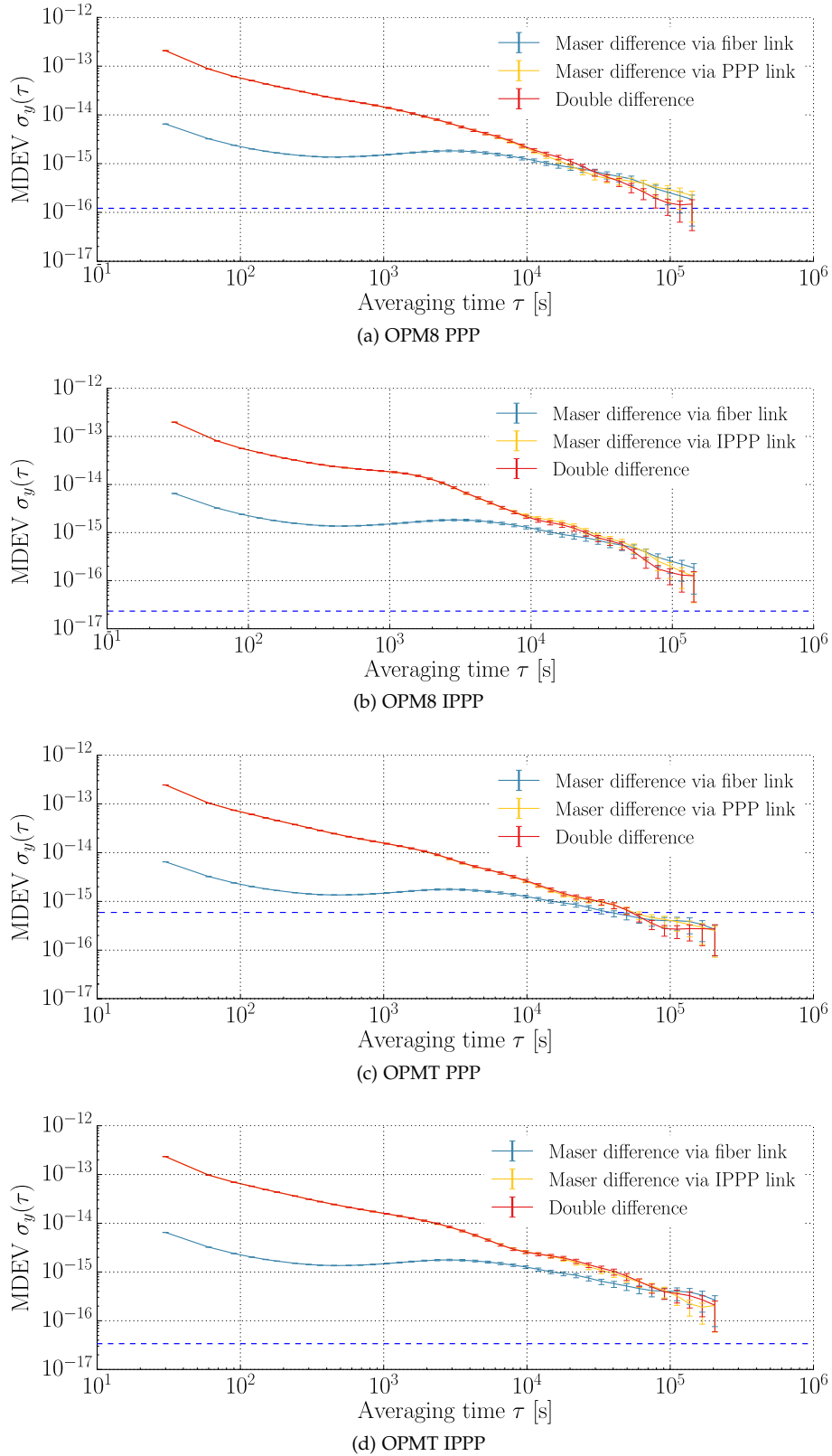


Figure 40: Frequency instability for the AHM comparison via GPS link and fiber link between LNE-SYRTE and PTB and the double difference between the links for PPP and IPPP links using two different GPS stations at LNE-SYRTE. The blue dashed line shows the average fractional frequency of the double difference.

Station	Link	T [ $10^6$ s]	$y_{\text{GPS}} - y_{\text{Fiber}}$ [ $10^{-16}$ ]	$\sigma$ [ $10^{-16}$ ]
OPMT	IPPP	1.2	-0.34	2.66
OPMT	PPP	1.2	-5.94	2.73
OPM8	IPPP	0.9	-0.23	0.57
OPM8	PPP	0.9	1.23	1.07

Table 9: Results of the comparison between the GPS links and the optical fiber link on the PTB-LNE-SYRTE baseline. The average fractional frequency deviations of the double difference  $y_{\text{GPS}} - y_{\text{Fiber}}$ , the corresponding uncertainty  $\sigma$ , and the total measurement time T are reported.

The fractional frequency deviations of the AHM comparison via optical fiber link and GPS link are shown in fig. 39 for the IPPP and PPP links using both GPS stations at LNE-SYRTE, the OPM8 station and the OPMT station.

In fig. 40 the frequency instability for the AHM comparison via optical fiber link and via GPS link is shown, together with the instability of the double difference between the GPS link and the optical fiber link. The instability of the AHM comparison via optical link is dominated by the instability of the AHMs. The instability of the AHM comparison via GPS link is dominated by the instability of the GPS link for averaging times up to 0.5 d for the OPM8 station and up to 1 d for the OPMT station. The cause for the degraded instability of the OPMT IPPP link compared to the OPM8 IPPP link for averaging times above  $10^4$  s is not known. The small bump in the instability of the IPPP link with OPM8 at an averaging time of  $1 \times 10^3$  s to  $2 \times 10^3$  s is related to the high number of troposphere parameters (48 per day) that were used in the IPPP processing for this link. The instabilities of the AHMs at PTB and LNE-SYRTE are already below  $1 \times 10^{-15}$  for averaging times above  $2 \times 10^4$  s, therefore the AHMs noise contribution to the AHMs comparisons via GPS link is not as significant as it was in the PTB-MPQ comparison, in which the AHM at MPQ had a flicker floor of  $1 \times 10^{-15}$ .

Due to the low instability of the involved AHMs, forming the double difference between the GPS links and the optical fiber links does not improve the instability significantly for all GPS links. Furthermore, the frequency instability is based on the periods in which the optical fiber link provided valid data. In the double difference between the GPS links and the optical fiber link, the noise contributions from the AHMs cancel out. Anyhow, the instability of the double difference does not necessarily represent the true instability of a continuous GPS link, because the dead time of the optical fiber link can alter the instability of the double difference in the presence of WPM and FPM, as discussed in sec.1.5.

### 3.5 Summary

The hardware stability of GNSS stations used for time and frequency transfer was reviewed. For frequency comparisons campaigns spanning several days to weeks, the most critical aspect is the temperature sensitivity of the outdoor equipment, the antenna and antenna cable. A temperature coefficient of not more than a few  $\text{ps K}^{-1}$  for the outdoor equipment is desirable and can be achieved with modern antenna cables with low temperature coefficients and typical antennas used for time and frequency transfer with GPS. It is also important to tightly control the temperature of the receiver environment ideally within 0.1 K, especially because temperature variations in the receiver environment can lead to code-phase inconsistencies.

Local baselines at PTB were studied with a focus on their temperature sensitivity. It was found that the PTBB station, often used for remote clock comparisons, has a high temperature coefficient relative to other stations at PTB, probably because it uses a RG-214 antenna cable, that has a 10 times higher temperature coefficient compared to other antenna cables used at PTB. A new dedicated GNSS station was set up at PTB for the optical clock comparison campaigns to avoid systematic frequency offsets due to temperature induced hardware delay variations. The new station was shown to have a good long-term stability, the TDEV of its WRB is 2 ps for an averaging time of one week.

As part of the ITOC project, PPP and IPPP analysis were performed on baselines between European NMIs that operate optical clocks to investigate the suitability of these techniques for the frequency comparison of optical clocks. It was shown that permanent, as well as transient code-phase inconsistencies can easily lead to systematic fractional frequency offsets of a few  $10^{-16}$  in continuous batch PPP solutions.

An optical fiber link between PTB and LNE-SYRTE was used to characterize the PPP and IPPP links between both institutes. The average fractional frequency deviations of the AHM comparison via IPPP and optical fiber link agree within a few  $10^{-17}$  for an averaging time of  $1 \times 10^6$  s, no systematic frequency offsets were observed.

For frequency comparisons of optical clocks IPPP is the preferred method over PPP due to its decreased instability for long averaging times, but more importantly, because it is not prone to systematic frequency offsets due to code-phase inconsistencies. Anyhow as demonstrated for the PTBB station, long-term variations of the carrier-phase hardware delays can lead to systematic fractional frequency offsets in IPPP solutions, therefore the station hardware stability is still an important factor.

If continuous batch PPP solutions are used for time and frequency transfer, it is important to validate the results, e.g. by comparison with daily batch PPP solutions as it is routinely done for the continuous batch PPP solutions used for TAI computations. If an estimate of the WRB for the station is available, it can provide valuable information about the stations hardware instability and the occurrence of code-phase inconsistencies.

# 4

## DIRECT REMOTE FREQUENCY COMPARISONS OF OPTICAL CLOCKS

For the remote frequency comparison of optical clocks using GPS time and frequency transfer techniques a microwave frequency reference for the GPS station is necessary. In many time laboratories of NMIs AHMs are used as flywheel oscillators, due to their reliability, low short-term instability and commercial availability. Other popular choices are commercial caesium or rubidium clocks. Using the optical femtosecond frequency comb technique (Diddams et al., 2000) it is possible to compare the microwave flywheel oscillators frequency with the optical frequency of the optical clock. Another interesting option is to directly generate a microwave frequency reference from the optical clock frequency using a frequency comb, an approach that was used in Fujieda et al., 2016 to compare optical clocks with TWSTFT.

### 4.1 Principles of Remote Frequency Comparisons of Optical Clocks

In this work the flywheel approach is used to perform remote frequency comparisons of optical clocks. The experimental setup is depicted in fig. 41: At both remote laboratories the optical clocks are compared to the microwave flywheel oscillators via optical femtosecond frequency combs and the microwave flywheel oscillators serve as a time and frequency reference for the GPS stations. This setup

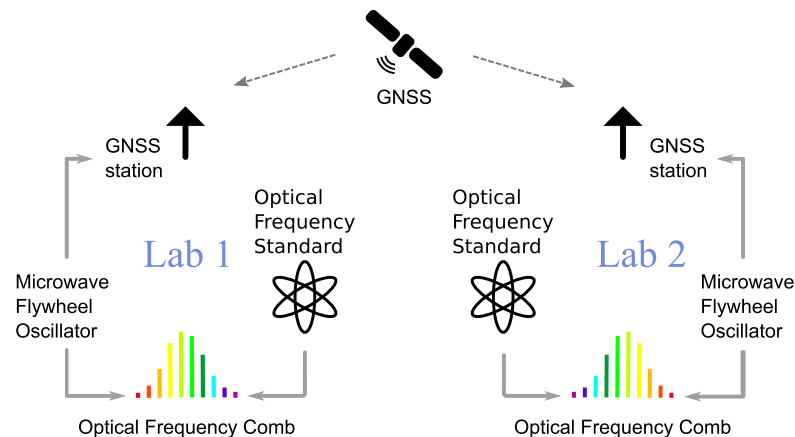


Figure 41: Experimental setup for remote frequency comparisons of optical clocks using GPS links: The optical clocks are compared to the microwave flywheel oscillators via optical femtosecond frequency combs and the microwave flywheel oscillators serve as a time and frequency reference for the GPS stations.

consists of at least three measurements, the local measurements of the relative frequency differences between the optical clocks and the flywheel oscillators at both laboratories and the remote comparison of the flywheel oscillators using the GPS link.

#### 4.1.1 Local and Remote Measurements

For the following discussion it is assumed that AHMs are chosen as the microwave flywheel oscillators and that the optical clocks have a significantly lower instability

than the flywheel oscillators. In this case, the measurements of the relative frequency differences  $\Delta y_j(t)$  between the optical clocks and the AHMs is dominated by the noise of the AHMs. Fig. 42 shows typical instabilities of the involved oscillators and GPS links.

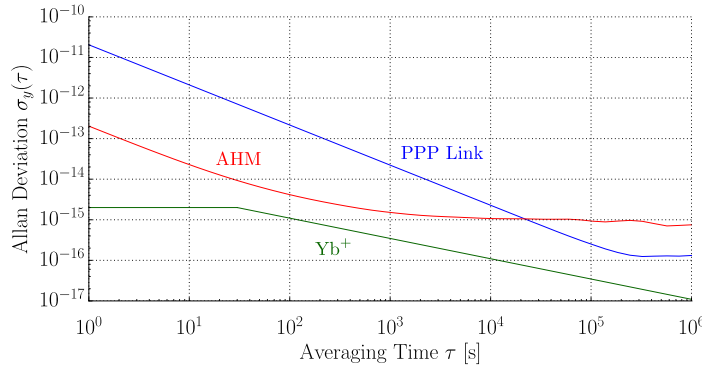


Figure 42: Typical instabilities of oscillators ( $\text{Yb}^+$  ion clock and AHM) and GPS links for remote optical clock comparisons.

The remote comparison of the AHMs consists of time differences  $\Delta x_{1,2}(t)$  usually dominated by the instability of the GPS link for short to intermediate averaging times and by the instability of the AHMs for averaging times above one day. If the results of the three separate, but simultaneous measurements are combined, the noise contributions from the flywheel oscillators cancel out and the instability of the combined measurement is dominated by the instability of the GPS link for all averaging times.

While the time difference data from the remote comparison of the flywheel oscillators is usually a continuous data set, the local frequency comparisons of the flywheel oscillators with the optical clocks often suffer from significant dead time. This dead time can be due to the limited duty cycle of the optical clocks or deliberately chosen measurement schedules.

In summary, the measurements consist of a remote comparison of the flywheel oscillators that

- consists of instantaneous phase time differences  $\Delta x(t)_{1,2} = x_1^{\text{AHM}}(t) - x_2^{\text{AHM}}(t) + \epsilon_{\text{link}}(t)$  every 30s,
- in which  $\epsilon_{\text{link}}(t)$  is the noise contribution from the GPS link to the remote AHM comparison,
- on a continuous time interval  $\mathbb{T}_x$  without dead time,
- and is dominated by the instability of the GPS link for averaging times up to one day depending on the instability of the AHM,

and two local comparisons of the optical clocks with the flywheel oscillators that

- consist of fractional frequency differences  $\Delta y_j(t) = y_j^{\text{opt}}(t) - y_j^{\text{AHM}}(t)$  on a 1s grid,
- on a set of time intervals  $\mathbb{T}_{y_j}$  with dead time in-between,
- are dominated by the instability of the flywheel oscillators.

## 4.1.2 Data Analysis Strategies

## 4.1.2.1 Intersecting Intervals

The most straight forward data analysis strategy would be to consider only the intersecting time intervals  $\mathbb{T}_o = \mathbb{T}_x \cap \mathbb{T}_{y_1} \cap \mathbb{T}_{y_2}$ , during which all three measurements produced valid data. In this case the noise contribution from the flywheel oscillators cancel out completely in the average fractional frequency difference  $\bar{y}(\mathbb{T})$ :

$$\begin{aligned}\bar{y}(\mathbb{T}_o) &= \frac{1}{T_o} \sum_{\mathbb{T}_o} \left( \frac{d\Delta x_{1,2}(t)}{dt} + \sum_{j=1}^2 (-1)^{j+1} \Delta y_j(t) \right) \\ &= \frac{1}{T_o} \sum_{\mathbb{T}_o} \left( y_1^{\text{opt}}(t) - y_2^{\text{opt}}(t) + \frac{d\epsilon_{\text{link}}(t)}{dt} \right),\end{aligned}\quad (114)$$

in which  $T_o = \|\mathbb{T}_o\|$  is the total measurement time of the set of intervals  $\mathbb{T}_o$ . In this case, the statistical uncertainty of the frequency comparison  $u(\mathbb{T}_o) = \sigma_{\text{link}}(\mathbb{T}_o)$  is dominated by the instability of the GPS link, because the instabilities of the optical clocks are negligible in comparison. It is noted that only the derivative of the GPS link noise contributes to the uncertainty, calibration errors do not contribute to the uncertainty of a frequency comparison.

This approach reduces the total measurement time, and creates artificial dead time in the continuous remote comparison of the flywheel oscillators via GPS link. From the discussion in chap. 1 of the impact of dead time on the variance of the sample mean (eq. 35) it is known that depending on the dominant noise type of the GPS link (for WPM and FPM), this artificial dead time can lead to an increase of the statistical uncertainty of the frequency comparison. This increase is larger than what would be expected solely from the reduced total measurement time, because the scaling of the variance of the sample mean with the sample size  $N$  changes from  $1/N^2$  to  $1/N$  due to the vanishing autocorrelation (eq. 36 for WPM and eq. 39 for FPM).

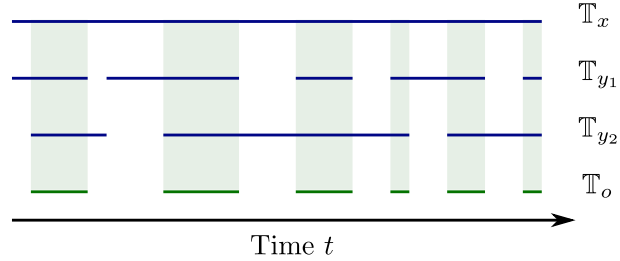


Figure 43: Set of intervals of the remote flywheel comparison ( $\mathbb{T}_x$ ), the two local comparisons between the optical clocks and the flywheel oscillators ( $\mathbb{T}_{y_j}$ ), and the set of intersecting intervals ( $\mathbb{T}_o = \mathbb{T}_x \cap \mathbb{T}_{y_1} \cap \mathbb{T}_{y_2}$ ).

## 4.1.2.2 Extrapolation Intervals

Another approach is to allow intervals, during which dead time occurred in one or both of the local comparisons between the optical clocks and the flywheel oscillators, to nevertheless contribute to the remote comparison of the flywheel oscillators via GPS link in order to increase the total measurement time of the remote comparison and reduce the effect that dead time has on the uncertainty. In this case, the



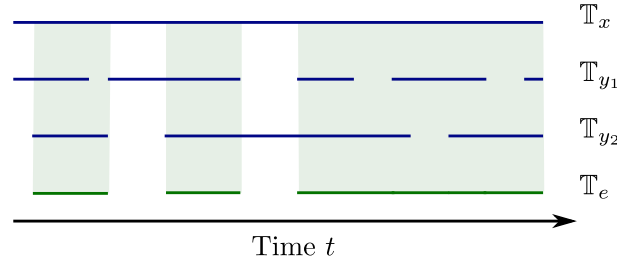


Figure 44: Set of intervals for the remote flywheel comparison ( $\mathbb{T}_x$ ), the two local comparisons between the optical clocks and the flywheel oscillators ( $\mathbb{T}_{y_j}$ ), and the set of extrapolation intervals ( $\mathbb{T}_e$ ).

noise contributions of the flywheel oscillators do not cancel out completely in the average fractional frequency difference:

$$\begin{aligned}
 \bar{y}(\mathbb{T}_e) &= \frac{1}{T_e} \sum_{\mathbb{T}_e} \frac{d\Delta x_{1,2}(t)}{dt} + \frac{1}{T_1} \sum_{\mathbb{T}_{y_1}} \Delta y_1(t) - \frac{1}{T_2} \sum_{\mathbb{T}_{y_2}} \Delta y_2(t) \\
 &= \frac{1}{T_e} \sum_{\mathbb{T}_e} \frac{d\epsilon_{\text{link}}(t)}{dt} + \frac{1}{T_1} \sum_{\mathbb{T}_e \cap \mathbb{T}_{y_1}} y_1^{\text{opt}}(t) - \frac{1}{T_2} \sum_{\mathbb{T}_e \cap \mathbb{T}_{y_2}} y_2^{\text{opt}}(t) \\
 &+ \left( \frac{1}{T_e} - \frac{1}{T_1} \right) \sum_{\mathbb{T}_e \cap \mathbb{T}_{y_1}} y_1^{\text{AHM}}(t) + \frac{1}{T_e} \sum_{\mathbb{T}_e \setminus \mathbb{T}_{y_1}} y_1^{\text{AHM}}(t) - \frac{1}{T_1} \sum_{\mathbb{T}_{y_1} \setminus \mathbb{T}_e} y_1^{\text{AHM}}(t) \\
 &- \left( \frac{1}{T_e} - \frac{1}{T_2} \right) \sum_{\mathbb{T}_e \cap \mathbb{T}_{y_2}} y_2^{\text{AHM}}(t) - \frac{1}{T_e} \sum_{\mathbb{T}_e \setminus \mathbb{T}_{y_2}} y_2^{\text{AHM}}(t) + \frac{1}{T_2} \sum_{\mathbb{T}_{y_2} \setminus \mathbb{T}_e} y_2^{\text{AHM}}(t),
 \end{aligned} \tag{115}$$

in which the set of 'extrapolation intervals'  $\mathbb{T}_e$  is a subset of  $\mathbb{T}_x$  that can include artificial dead time. In eq. 115 six additional sets of intervals are considered:

- $\mathbb{T}_e \cap \mathbb{T}_{y_1}$  ( $\mathbb{T}_e \setminus \mathbb{T}_{y_1}$ ), in which  $\Delta y_1$  is (not) available,
- $\mathbb{T}_e \cap \mathbb{T}_{y_2}$  ( $\mathbb{T}_e \setminus \mathbb{T}_{y_2}$ ), in which  $\Delta y_2$  is (not) available.
- $\mathbb{T}_{y_1} \setminus \mathbb{T}_e$  ( $\mathbb{T}_{y_2} \setminus \mathbb{T}_e$ ), in which artificial dead time has been inserted into the link data  $\Delta x_{1,2}(t)$ , even though  $\Delta y_1$  ( $\Delta y_2$ ) is available.

It is noted that the set of intervals over which optical clocks fractional frequency differences  $y_j^{\text{opt}}(t)$  are averaged are different for each optical clock, and the contribution from the optical clocks to the uncertainty of the comparison is still negligible.

The statistical uncertainty  $u$  of the frequency comparison in this approach is given by

$$u^2(\mathbb{T}_e) = \sigma_{\text{link}}^2(\mathbb{T}_e) + \sigma_{\text{AHM}_1}^2(\mathbb{T}_e) + \sigma_{\text{AHM}_2}^2(\mathbb{T}_e), \tag{116}$$

in which  $\sigma_{\text{AHM}_j}^2$  are the 'extrapolation uncertainties' that stem from the remaining  $y_j^{\text{AHM}}(t)$  terms in eq. 115. The reduced uncertainty from the remote comparison of the AHMs via GPS link  $\sigma_{\text{link}}^2(\mathbb{T}_e) \leq \sigma_{\text{link}}^2(\mathbb{T}_o)$  comes at the price of additional contributions to the statistical uncertainty from the flywheel oscillators. The goal is to find an optimal set of intervals  $\mathbb{T}_e$  that minimizes the uncertainty  $u$ . In some cases it might be beneficial to introduce sets of intervals  $\mathbb{T}_j^*$ , so that  $\mathbb{T}_{y_j}^* \setminus \mathbb{T}_e$  is small.

This flywheel approach was used in the past for the traceability of frequency calibrations in Douglas et al., 1997. Recently, this approach was used for local frequency comparisons involving an optical clock and the generation of a timescale

based on an optical clock (Grebing et al., 2016). In this work, the method has been extended to remote comparisons including a second flywheel oscillator.

#### 4.1.3 Estimation of the Statistical Uncertainty Contributions

From the discussion in chap. 1 it is known that the uncertainty of an average frequency measurement depends on the noise characteristic given by the spectral density  $S_y(f)$  and on the weighting function  $w(t)$ . If  $S_y(f)$  is known, the uncertainty  $u(\mathbb{T}_e)$  can be estimated using eq. 20 and the corresponding weighting function from eq. 115:

$$w_{\mathbb{T}_e, \text{link}}(t) = \begin{cases} \frac{1}{\mathbb{T}_e}, & \text{for } t \in \mathbb{T}_e \\ 0, & \text{elsewhere,} \end{cases} \quad (117)$$

for the statistical uncertainty of the remote AHM comparison via GPS link, and

$$w_{\mathbb{T}_e, \text{AHM}_j}(t) = \begin{cases} \frac{1}{\mathbb{T}_e} - \frac{1}{\mathbb{T}_j}, & \text{for } t \in \mathbb{T}_e \cap \mathbb{T}_{y_j} \\ \frac{1}{\mathbb{T}_e}, & \text{for } t \in \mathbb{T}_e \setminus \mathbb{T}_{y_j} \\ -\frac{1}{\mathbb{T}_j}, & \text{for } t \in \mathbb{T}_{y_j} \setminus \mathbb{T}_e \\ 0, & \text{elsewhere,} \end{cases} \quad (118)$$

for the extrapolation uncertainty. With a power-law noise model of  $S_y(f)$  (eq. 17) and the relation between the spectral density and the standard variance (eq. 20), the link uncertainty is given as

$$\sigma_{\text{link}}^2(\mathbb{T}_e) = \sum_{\alpha=-2}^2 h_{\text{link}, \alpha} \int_0^{\infty} f^\alpha |W_{\mathbb{T}_e, \text{link}}(f)|^2 df, \quad (119)$$

with the Fourier transform  $W_{\mathbb{T}_e, \text{link}}(f) = \int_{-\infty}^{\infty} \exp(2\pi i f t) w_{\mathbb{T}_e, \text{link}}(t) dt$ . Analogously, the extrapolation uncertainties are

$$\sigma_{\text{AHM}_j}^2(\mathbb{T}_e) = \sum_{\alpha=-2}^2 h_{\text{AHM}_j, \alpha} \int_0^{\infty} f^\alpha |W_{\mathbb{T}_e, \text{AHM}_j}(f)|^2 df, \quad (120)$$

with the Fourier transforms  $W_{\mathbb{T}_e, \text{AHM}_j}(f) = \int_{-\infty}^{\infty} \exp(2\pi i f t) w_{\mathbb{T}_e, \text{AHM}_j}(t) dt$ .

In case of FFM and RWFm a lower cutoff frequency is necessary for the integral in eq. 119 and 120 to converge. The cutoff frequency was set to  $f_l = (20T)^{-1}$  throughout this work with  $T$  being the duration of the measurement campaign.

The noise models  $h_{\text{AHM}_j, \alpha}$  and  $h_{\text{link}, \alpha}$  are best estimated based on measured power spectral densities. They can also be calculated based on the AVAR (see tab. 1), but it has to be kept in mind, that there is no unique mapping from the AVAR to the spectral density (Greenhall, 1998).

The uncertainties can also be estimated using a Monte Carlo simulation, an approach used in Leute et al., 2016; Yu et al., 2007. In the Monte Carlo approach the noise models of the flywheel oscillators and the GPS link are fed into a noise simulation software (e. g. Kasdin et al., 1992), that creates ensembles of simulated data sets for each noise model. These dead time free data sets can then be used to calculate average frequency differences for all sets of intervals of interest (e. g. different  $\mathbb{T}_e$ ). By comparison of the average fractional frequency differences for e. g.  $\mathbb{T}_e$  and  $\mathbb{T}_{y_1}$ , and calculating the standard variance of this difference for the whole

ensemble of simulated data sets with the noise model of AHM<sub>1</sub>, the extrapolation uncertainty  $\sigma_{\text{AHM}_1}(\mathbb{T}_e)$  can be estimated.

#### 4.1.3.1 Noise Characterization of the AHMs

For the estimation of the uncertainties noise models  $h_{\text{AHM}_j,\alpha}$  for the AHMs have to be build. Besides the local measurement against the optical clock, measurements against caesium frequency standards or other AHMs can be used for a dead time free estimate of the instability for the flywheel oscillator at longer averaging times.

The three cornered hat method (Gray et al., 1974) is often used to estimate the instability of oscillators from comparisons to other oscillators with a similar instability. Considering three independent frequency comparisons between pairs of oscillators  $\text{osc} = \{a, b, c\}$  with variances  $\sigma_{\text{osc}}^2$ , the variances of the frequency comparisons are

$$\begin{aligned}\sigma_{\text{ab}}^2 &= \sigma_a^2 + \sigma_b^2, \\ \sigma_{\text{ac}}^2 &= \sigma_a^2 + \sigma_c^2, \\ \sigma_{\text{bc}}^2 &= \sigma_b^2 + \sigma_c^2.\end{aligned}\tag{121}$$

The variances of the individual oscillators can be separated accordingly:

$$\begin{aligned}\sigma_a^2 &= \frac{1}{2} \left( \sigma_{\text{ab}}^2 + \sigma_{\text{ac}}^2 - \sigma_{\text{bc}}^2 \right), \\ \sigma_b^2 &= \frac{1}{2} \left( \sigma_{\text{ab}}^2 + \sigma_{\text{bc}}^2 - \sigma_{\text{ac}}^2 \right), \\ \sigma_c^2 &= \frac{1}{2} \left( \sigma_{\text{ac}}^2 + \sigma_{\text{bc}}^2 - \sigma_{\text{ab}}^2 \right).\end{aligned}\tag{122}$$

The AHM noise models used in this work do not include a frequency drift. To minimize the impact of frequency drifts on the calculated average frequency difference based on different sets of intervals, a linear fit to the fractional frequency differences is performed for all data sets. The average fractional frequency difference is then extracted by evaluating the linear fit at the center of mass of the extrapolation interval.

#### 4.1.3.2 Noise Characterization of the GPS Links

The estimation of the uncertainty of the GPS link can be based on the dead time free remote AHM comparison. One difficulty is that for averaging times above 0.5 d the instability of the AHM comparison is usually dominated by the instability of the AHMs. The following assumptions based on the results from ch. 3 are made:

- The instability of the GPS link is given by the ADEV of the AHM comparison via GPS link up to  $\tau = 0.5$  d,
- the dominant noise type for  $\tau \geq 0.5$  d is FPM for PPP and IPPP links,
- with an additional FFM contribution of  $1 \times 10^{-16}$  for PPP links.

Name	T&F Reference	Receiver	Antenna
NP11	Maser HM2	Dicom GTR50	NOV702
KOP1	Maser H9	Septentrio PolaRx4TR	NOV750.R4 NOVS

Table 10: GPS stations for AHM comparison between PTB and NPL.

## 4.2 Remote Comparison of $\text{Yb}^+$ Ion Clocks between PTB and NPL

At NPL and PTB optical clocks based on transitions in the  $^{171}\text{Yb}^+$  ion are developed. Details about the experimental setup of this single-ion clocks can be found in Godun et al., 2014; Huntemann et al., 2012a,b, 2016; Tamm et al., 2009, 2014. The  $\text{Yb}^+$  ion has two transitions that are currently accepted as secondary representations of the second, the electric quadrupole transition (E2:  $^2\text{S}_{1/2} \rightarrow ^2\text{D}_{3/2}$ ) at 436 nm and the electric octupole transition (E3:  $^2\text{S}_{1/2} \rightarrow ^2\text{F}_{7/2}$ ) at 467 nm.

Up until recently this optical clocks could only be compared by measuring their frequency against caesium primary standards (e. g. Godun et al., 2014; Tamm et al., 2014) or other optical frequency standards in local measurements.

In this work a direct remote frequency comparison of the optical clocks via GPS link is presented. In 2014 a comparison of the clocks based on the E2 transition in the  $^{171}\text{Yb}^+$  ion via GPS link was performed, and in 2015 in a second measurement campaign, the E3 transition was chosen as reference for the frequency comparison.

### 4.2.1 Measurement Campaign using the Quadrupole Transition

#### 4.2.1.1 Remote Flywheel Comparison via GPS Link

At PTB the dedicated GNSS station KOP1 with the AHM H9 as external time and frequency reference, and at NPL the NP11 GPS station with the AHM HM2 as reference was chosen for the remote comparison of the AHMs. Details about the stations are summarized in tab. 10. During the comparison period the PPP and IPPP clock solution of the NPL station shows several steps, corresponding to a cycle slip of a 56 MHz oscillator on the JAVAD board in the Dicom GTR50 receiver. These steps are corrected for in post-processing of the PPP and IPPP solution, which is possible because the frequency of 56 MHz is well defined and the time evolution of the clock is unconstrained in the sequential filter used in PPP. Apart from that the GPS link data is continuous and available from MJD 56 951 to 56 961.

#### 4.2.1.2 Local Comparisons of the $\text{Yb}^+$ Ion Clocks with the AHMs

The measurement of the  $\text{Yb}^+$  ion clock at PTB started on MJD 56 952 at around 20:00 UTC, whereas data from the NPL  $\text{Yb}^+$  ion clock is available from MJD 56 958 at around 11:00 UTC. The measurements end with the failure of the maser H9 at PTB on MJD 56 961 at around 6:00 UTC. At PTB the achieved operational time of more than 130 h was mainly limited by failures of the  $\text{Yb}^+$  cooling laser and long dark periods of the ion thought to be caused by collisions. At NPL the operational time of 46 h was limited by the occurrence of an abnormally high drift rate of the probe laser's high-finesse stabilization cavity during the first days of the campaign. The uptime of 66% was limited by the need to repeatedly pause data-taking to measure the background magnetic field.

In order to cancel the quadrupole shift on the transition frequency due to the interaction of the ion with the gradient of the electric field in the trap, measurements have to be averaged over three mutually orthogonal orientations of the magnetic field. At NPL the switch between the different fields was performed every 300 s and

data was collected for 270s within this 300s interval with a dead time between the measurements of 30s to allow the clock servo to settle. This data taking scheme is depicted in fig. 45. This measurement schedule leads to a regularly distributed dead time of 10%. At PTB the magnetic field setting was changed every 8 h, leading to significantly less interruptions.

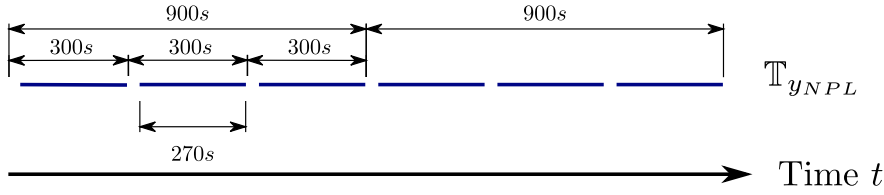


Figure 45: Measurement schedule for local comparison of AHM HM2 and the  $\text{Yb}^+$  clock at NPL with dead time. In a 900s interval three measurements with orthogonal magnetic field settings are scheduled with a dead time of 30s in between.

#### 4.2.1.3 Estimation of the Statistical Uncertainties

In fig. 46 the ADEVs for the flywheel oscillators HM2 (NPL) and H9 (PTB) and the PPP link between PTB and NPL are depicted. The noise model of the AHM H9 is based on its comparison to the  $\text{Yb}^+$  clock, while the AHM HM2 was characterized using a three cornered hat analysis against other AHMs at NPL. The noise model of the PPP link follows the measured noise up to the point where the measured ADEV is dominated by the noise of the NPL maser HM2 ( $\tau \approx 2 \times 10^4 \text{s}$ ) and then assumes that the true link instability is dominated by FPM with a FPM floor of  $1 \times 10^{-16}$ . Figure 46 also demonstrates the impact of the regularly distributed dead time of 30s every 300s in the NPL optical frequency comparison due to the quadrupole cancellation scheme on the ADEV and therefore the uncertainty  $\sigma_{\text{link}}^2(T_o)$  of the PPP link, e.g for an averaging time of  $\tau = 1 \times 10^5 \text{s}$ , the ADEV with dead time is increased by a factor of ten compared to the ADEV without dead time.

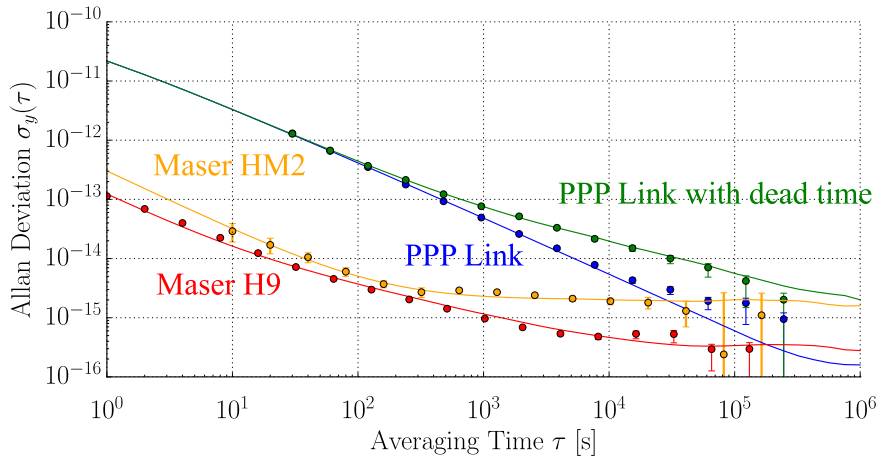


Figure 46: ADEV for the flywheel oscillators at HM2 (orange) and H9 (red) and the PPP link (blue). The dots show measurement data (HM2: three cornered hat, H9: measurement against  $\text{Yb}^+$ ), the solid lines show simulations based on the models described in tab. 11 (using the algorithm from Kasdin et al., 1992). The impact of the regularly distributed 30 seconds dead time from the quadrupole cancellation scheme at NPL on the ADEV of the PPP link is shown in green.

	WPM[s/ $\tau$ ]	FPM[s/ $\tau$ ]	WFM[ $\sqrt{s/\tau}$ ]	FFM
AHM HM2	$3.0 \times 10^{-13}$	0	$3.5 \times 10^{-14}$	$2.0 \times 10^{-15}$
AHM H9	$1.2 \times 10^{-13}$	0	$3.5 \times 10^{-14}$	$3.0 \times 10^{-16}$
PPP link	0	$2.0 \times 10^{-11}$	0	$1.0 \times 10^{-16}$
IPPP link	0	$2.0 \times 10^{-11}$	0	0

Table 11: Noise models (AVAR at 1 s averaging time) of the flywheel oscillators H9 and HM2, and the PPP and IPPP link between NPL and PTB.

To minimize the uncertainty of the frequency comparison four different extrapolation intervals  $\mathbb{T}_e$  are studied:

- A: In the first case only the intersecting intervals between all three measurements are considered  $\mathbb{T}_A = \mathbb{T}_x \cap \mathbb{T}_{y_{\text{NPL}}} \cap \mathbb{T}_{y_{\text{PTB}}}$  with a total measurement time of  $T_A = 33$  h.
- B: In the second case the extrapolation interval starts with the first NPL optical clock measurement and regularly distributed dead time from the quadrupole cancellation scheme is extrapolated, which increases the total measurement time to  $T_B = 45$  h.
- C: In the third case additional dead time due to the maintenance of the clock systems at PTB and NPL are extrapolated between the start of the NPL optical clock measurements and the end of the campaign leading to a total measurement time of  $T_C = 67$  h.
- D: In the fourth case the extrapolation interval covers the whole PPP link measurement  $\mathbb{T}_D = \mathbb{T}_x$ , including several days at the beginning on which no NPL optical clock data is available with  $T_D = 246$  h.

In the first three cases (A-C)  $\mathbb{T}_{y_{\text{PTB}}}^*$  is restricted to the period after the first NPL optical clock measurement.

#### 4.2.1.4 Results and Discussion

The results of the frequency comparison for all four cases (A-D) and both GPS frequency transfer techniques are presented in fig. 47. The individual contributions to the statistical uncertainty and the combined uncertainty (eq. 116) for the four cases (A-D) are summarized in fig. 47.

The largest statistical uncertainty is observed in case A in which no dead time is extrapolated so that  $u(\mathbb{T}_A) = \sigma_{\text{link}}(\mathbb{T}_A) = 5.51 \times 10^{-15}$  (for PPP and IPPP). Without dead time, the uncertainty of the GPS links for an averaging time of  $T_A = 33$  h would be a factor of 10 smaller and to decrease the uncertainty with dead time by this factor a 100 times longer measurement time would be necessary, because the uncertainty with dead time scales with  $1/\sqrt{N}$  instead of  $1/N$ . This demonstrates the significant impact that dead time in the local optical clock measurements can have on the uncertainty of a remote frequency comparison via GPS link.

In the second case (B) in which the regularly distributed dead time due to the quadrupole cancellation scheme at NPL is extrapolated, the uncertainty contributions from the PPP and IPPP links is significantly smaller ( $\sigma_{\text{link}}(\mathbb{T}_B) = 9.5 \times 10^{-16}$ ), even though the measurement time increases only about 12 h. The trade-off are the emerging extrapolation uncertainties due to the maser contributions, which are still below  $1 \times 10^{-16}$  in case B.

In the third case (C), the NPL extrapolation uncertainty becomes noticeably larger ( $\sigma_{\text{HM2}}(\mathbb{T}_C) = 3.8 \times 10^{-16}$ ), due to the performance of the maser HM2, while the

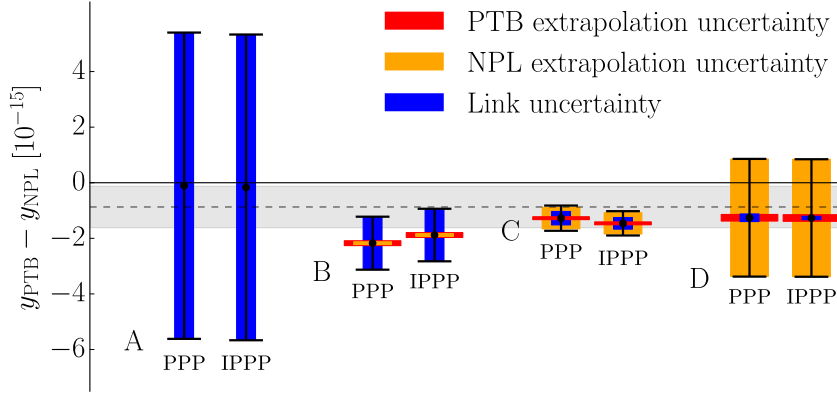


Figure 47: Average fractional frequency difference  $y_{\text{PTB}} - y_{\text{NPL}}$  of the  $^{171}\text{Yb}^+$  E2 transition with statistical uncertainties for four different extrapolation cases (A-D) using PPP and IPPP links. The grey dashed line and the shaded region show the result from absolute frequency measurements against caesium fountain clocks and its uncertainty (from Godun et al., 2014; Tamm et al., 2014).

PTB extrapolation uncertainty is still well below  $1 \times 10^{-16}$ . The total statistical uncertainty  $u(\mathbb{T}_C) = 4.5 \times 10^{-16}$  for the PPP link with a contribution from the link of  $\sigma_{\text{PPP}}(\mathbb{T}_C) = 2.4 \times 10^{-16}$ . For the IPPP link the combined statistical uncertainty  $u(\mathbb{T}_C) = 4.4 \times 10^{-16}$  with a contribution from the link of  $\sigma_{\text{IPPP}}(\mathbb{T}_C) = 2.1 \times 10^{-16}$ .

In case D in which several days of dead time in the NPL optical clock measurement is extrapolated, the advantage of the IPPP link over the PPP link is significant with the contribution from the PPP link of  $\sigma_{\text{PPP}}(\mathbb{T}_C) = 1.4 \times 10^{-16}$  and the contribution from the IPPP link  $\sigma_{\text{IPPP}}(\mathbb{T}_C) = 0.6 \times 10^{-16}$ . Unfortunately, due to the instability of the AHM HM2, the NPL extrapolation uncertainty starts to dominate the total statistical uncertainty  $u(\mathbb{T}_D) = 2.11 \times 10^{-15}$ , reaching the flicker floor of the NPL AHM HM2.

The result of the remote frequency comparison with the smallest combined statistical uncertainty is  $y_{\text{PTB}} - y_{\text{NPL}} = (-1.46 \pm 0.55) \times 10^{-15}$  for IPPP with a measurement time of 67 h (case C), which includes the systematic uncertainties from the Yb<sup>+</sup> ion clocks, which are  $1.0 \times 10^{-16}$  for the PTB clock and  $3.2 \times 10^{-16}$  for the NPL clock (from Leute et al., 2016). A correction for all known systematic frequency shifts, including the gravitational redshift corresponding to a height difference between the clocks of  $(66.7 \pm 0.4)$  m, was applied. This result agrees with the previously published results from comparisons of the Yb<sup>+</sup> ion clocks against caesium fountains  $y_{\text{PTB}} - y_{\text{NPL}} = (-8.7 \pm 7.5) \times 10^{-16}$  (Godun et al., 2014; Tamm et al., 2014).

Results from this measurement campaign based on the PPP link and an estimation of the statistical uncertainty with a Monte Carlo simulation have been published in Leute et al., 2016. The reported average fractional frequency deviation was  $y_{\text{PTB}} - y_{\text{NPL}} = (-1.3 \pm 1.2) \times 10^{-15}$ . The larger uncertainty compared to the PPP results for the same extrapolation scheme in this work is due to a more conservative noise model for the PPP link in Leute et al., 2016.

#### 4.2.2 Measurement Campaign using the Octupole Transition

##### 4.2.2.1 Remote Flywheel Comparison via GPS Link

The same station setup as in the 2014 campaign was used for the 2015 measurement campaign (see tab. 10). The Dicom GTR50 receiver, which is part of the NP11 station at NPL had been repaired in the meantime and no cycle slips occurred. PPP and IPPP solutions are available from MJD 57 177 to MJD 57 202. As discussed in sec. 3.3.3, two large day-boundary discontinuities were observed in the PPP link for this campaign which hints to code-phase inconsistencies that can deteriorate the accuracy of the PPP link.

##### 4.2.2.2 Local Comparisons of the $\text{Yb}^+$ Ion Clocks with the AHMs

The local comparison of the  $\text{Yb}^+$  ion clock with the AHM at PTB started several days after the official start of the campaign on MJD 57 183 around 15:45 UTC. and ended earlier on MJD 57 196 around 17:00 UTC with an operational time of 203 h.

At NPL the local measurement of the  $\text{Yb}^+$  clock started earlier at MJD 57 177 around 14:00 UTC and ended at 57 202 with an operational time of 462 h, which corresponds to an uptime of 74%. A different quadrupole cancellation scheme was used to avoid the frequent dead time from the previous campaign.

##### 4.2.2.3 Estimation of the Statistical Uncertainties

Two extrapolation cases were investigated, in the first case (A) the whole interval of the GPS link measurement from MJD 57 177 to 57 202 was chosen with a total measurement time of 624 h. In the second case (B), the interval starting with the first day of local optical clock measurements at PTB on MJD 57 183 and ending MJD 57 196 with a total measurement time of 336 h was chosen. The same noise models as in the 2014 campaign were used (tab. 11 and fig. 46).

##### 4.2.2.4 Results and Discussion

The results of the frequency comparison between the  $\text{Yb}^+$   $E_3$  transitions realized at PTB and NPL are depicted in fig. 48.

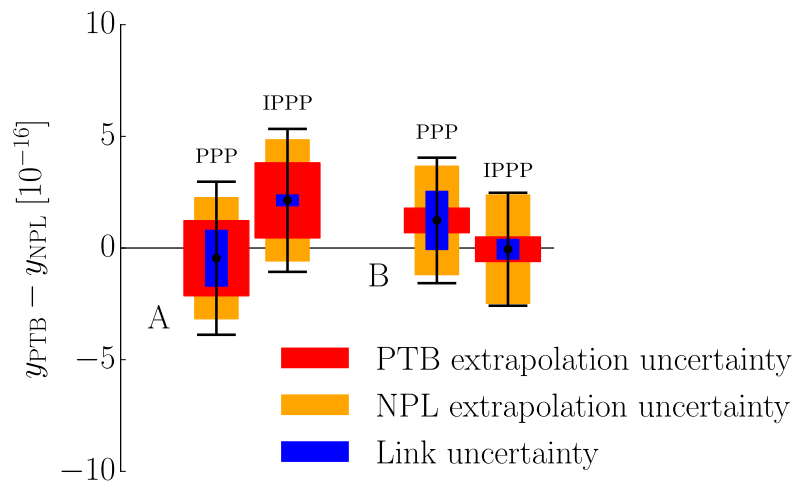


Figure 48: Average  $y_{\text{PTB}} - y_{\text{NPL}}$  of the  $^{171}\text{Yb}^+$   $E_3$  transition with statistical uncertainties for two extrapolation cases (A-B) using PPP and IPPP links.

In case A, the extrapolation uncertainties are  $1.7 \times 10^{-16}$  for the PTB AHM and  $2.7 \times 10^{-16}$  for the NPL AHM. The PPP link uncertainty has the same order of



magnitude with  $\sigma_{\text{PPP}}(\mathbb{T}_\Lambda) = 1.2 \times 10^{-16}$ , due to the flicker floor of the PPP noise model, while the uncertainty for the IPPP is significantly smaller with  $\sigma_{\text{IPPP}}(\mathbb{T}_\Lambda) = 2 \times 10^{-17}$ . The average frequency difference for the comparisons of the AHMs for IPPP and PPP do not agree within the uncertainties of the GPS links, which is probably due to a systematic frequency offset in the PPP link as discussed in ch. 3 sec. 3.3.3 that is not accounted for in the statistical model of the PPP link.

The combined statistical uncertainty in case B is dominated by the extrapolation uncertainty at NPL ( $2.4 \times 10^{-16}$ ), the extrapolation uncertainty at PTB is reduced to  $6 \times 10^{-17}$ . The local optical clock measurement at NPL had an excellent duty cycle, but the higher instability of the AHM at NPL compared to the AHM at PTB results in a four times larger extrapolation uncertainty. Extrapolating less data would significantly increase the link uncertainty, due to the introduction of artificial dead time in the link measurement. The PPP link uncertainty is nearly unchanged compared to case A with  $\sigma_{\text{PPP}}(\mathbb{T}_\Lambda) = 1.3 \times 10^{-16}$  and the uncertainty for the IPPP link increases to  $\sigma_{\text{IPPP}}(\mathbb{T}_\Lambda) = 5 \times 10^{-17}$ .

The final result is based on the IPPP link and the extrapolation interval of case B, because it leads to the smallest statistical uncertainty and the IPPP link is expected to be less affected by systematic effects. The result of the remote frequency comparison between the  $^{171}\text{Yb}^+$  ion clocks based on the octupole transition at PTB and NPL is  $y_{\text{PTB}} - y_{\text{NPL}} = (-0.1 \pm 3.1) \times 10^{-16}$ , including the systematic uncertainties of the optical clocks. The result has been corrected for all known systematic frequency shifts, including the gravitational redshift. The systematic uncertainty of the optical clock at PTB was  $5 \times 10^{-18}$  similar to what was published in Huntemann et al., 2016 and the systematic uncertainty of the optical clock at NPL was  $1.75 \times 10^{-16}$  (Margolis, 2015). This result is in agreement with results from absolute frequency measurements against caesium fountains  $y_{\text{PTB}} - y_{\text{NPL}} = (-0.7 \pm 6.9) \times 10^{-16}$  (from Godun et al., 2014; Huntemann et al., 2014).

### 4.3 Summary

A method to estimate the various contributions to the statistical uncertainty of a remote frequency comparison of optical clocks via GPS link in the presence of frequent dead time was developed. The approach is based on the knowledge of the noise characteristic of the GPS link, as well as the flywheel oscillators that are used to bridge dead time in the local optical clock measurements.

The results of two measurement campaigns comparing clocks based on the electric quadrupole and octupole transition in  $^{171}\text{Yb}^+$  at PTB and NPL were presented. Statistical uncertainties of a few  $10^{-16}$  were reached in both campaigns. While the average fractional frequency differences of the optical clocks agree within the statistical uncertainty for the octupole transition, a systematic frequency offset is observed for the quadrupole transition that is not accounted for in the systematic uncertainty budgets. The results from this remote frequency comparisons via GPS links agree with absolute frequency measurements against caesium fountains.

The significant impact of frequent dead time in a remote clock comparison using a GPS link dominated by WPM and FPM was demonstrated. The flywheel extrapolation approach allowed to reduce the statistical uncertainty in the presence of frequent dead time significantly by a factor of 10.

In both measurement campaigns, the final statistical uncertainty was dominated by the instability of the flywheel oscillator at NPL. This highlights the importance of the performance of the flywheel oscillators, when long measurement times are required in a measurement including optical clocks with limited duty cycle.

The approach used in this work to calculate the various contributions to the statistical uncertainty of a remote frequency comparison of optical clocks via GPS

link does not just provide an estimate of the combined uncertainty, but also gives insight into how certain parts of the experimental setup influence the uncertainty and therefore can be used to identify weaknesses of the measurement setup and schedule. It is a powerful tool to plan and optimize future measurement campaigns. It can be used to study the impact of various flywheel oscillators on the achievable uncertainty for a given duty cycle or to optimize the schedule for required maintenance time of the clock systems.

*One never notices what has been done;  
one can only see what remains to be done.*

Marie Curie

## OUTLOOK

---

It was shown that using an improved GPS frequency transfer technique and sufficiently stable hardware, the comparison of optical clocks with an uncertainty of a few  $10^{-16}$  is achievable. The statistical uncertainty of the frequency comparisons of the  $^{171}\text{Yb}^+$  ion clocks reported in this work was dominated by the noise of one of the flywheel oscillators used to bridge the frequent dead time due to the limited duty cycle of the optical clock. Frequency comparisons of optical clocks with this setup can profit from better duty cycles of the optical clocks and besides that from flywheel oscillators with lower instabilities. Cryogenic sapphire oscillators for example have a short-term instability 10 times lower than AHMs (Nand et al., 2011).

Additionally, a network of optical fiber links between European NMIs, currently between NPL, LNE-SYRTE and PTB will allow the comparison of optical clocks without contributing noise to the uncertainty (Lisdat et al., 2016). Transportable optical clocks reaching accuracies below  $10^{-16}$  (Cao et al., 2017; Koller et al., 2017) are another possibility to compare optical clocks developed at different institutes.

In this work, the performance of IPPP and PPP links on local and continental baselines was studied. It will be of interest to study the performance of IPPP on intercontinental baselines, especially because the establishment of optical fiber links on intercontinental baselines will be challenging. IPPP link on intercontinental baselines can be studied e.g. by comparisons with T2L2 (Samain et al., 2008), ACES MicroWave Link (Cacciapuoti et al., 2011) and carrier-phase TWSTFT (Fujieda et al., 2014).

Further improvements to the IPPP technique can be expected. The dual-frequency GPS IPPP methods based on the ionosphere-free linear combinations (e.g. Collins et al., 2010; Ge et al., 2007; Laurichesse et al., 2007) can be extended to include a third frequency and to include multiple GNSS systems (Geng et al., 2013; Laurichesse et al., 2016). Another more flexible route is to base the IPPP model on uncombined observations (e.g. Teunissen et al., 2010) in order to be able to offer uncombined satellite corrections to the user for multi-frequency and multi-GNSS applications (Odijk et al., 2016). Furthermore, combined precise integer satellite clock products from several ACs can provide more robust clock products (Seepersad et al., 2016). The effect of more robust integer satellite clock products and the inclusion of additional frequencies and GNSS on the frequency transfer performance of IPPP has yet to be studied.



## BIBLIOGRAPHY

---

- Allan, D. W. (1966). 'Statistics of atomic frequency standards'. *Proc. of the IEEE* **54**(2), pp. 221–230.
- Allan, D. W. and M. A. Weiss (1980). 'Accurate Time and Frequency Transfer During Common-View of a GPS Satellite'. In: *34th Annual Symposium on Frequency Control*, pp. 334–346.
- Allan, D. W. and J. A. Barnes (1981). 'A Modified "Allan Variance" with Increased Oscillator Characterization Ability'. In: *Thirty Fifth Annual Frequency Control Symposium*, pp. 470–475.
- Allan, D. W. and C. Thomas (1994). 'Technical Directives for Standardization of GPS Time Receiver Software: to be implemented for improving the accuracy of GPS common-view time transfer'. *Metrologia* **31**(1), p. 69.
- Ashby, N. (2003). 'Relativity in the Global Positioning System'. *Living Reviews in Relativity* **6**(1), p. 1.
- Barnes, J. A. et al. (1971). 'Characterization of Frequency Stability'. *IEEE Transactions on Instrumentation and Measurement* **IM-20**(2), pp. 105–120.
- Baugh, R. A. (1971). 'Frequency Modulation Analysis with the Hadamard Variance'. In: *25th Annual Symposium on Frequency Control*, pp. 222–225.
- Benkler, E., C. Lisdat, and U. Sterr (2015). 'On the relation between uncertainties of weighted frequency averages and the various types of Allan deviations'. *Metrologia* **52**(4), p. 565.
- Bertiger, W. et al. (2010). 'Single receiver phase ambiguity resolution with GPS data'. *Journal of Geodesy* **84**(5), pp. 327–337.
- Boehm, J., A. Niell, P. Tregoning, and H. Schuh (2006). 'Global Mapping Function (GMF): A new empirical mapping function based on numerical weather model data'. *Geophysical Research Letters* **33**(7), p. L07304.
- Boehm, J., R. Heinkelmann, and H. Schuh (2007). 'Short Note: A global model of pressure and temperature for geodetic applications'. *Journal of Geodesy* **81**(10), pp. 679–683.
- Bruyninx, C. and P. Defraigne (1999). 'Frequency Transfer Using GPS Codes and Phases: Short- and Long-Term Stability'. In: *Proc. of the 31st Precise Time and Time Interval Meeting*, pp. 471–178.
- Cacciapuoti, L. and C. Salomon (2011). 'Atomic clock ensemble in space'. *Journal of Physics: Conference Series* **327**(1), p. 012049.
- Calonico, D. et al. (2014). 'High-accuracy coherent optical frequency transfer over a doubled 642-km fiber link'. *Applied Physics B* **117**(3), pp. 979–986.
- Cao, J. et al. (2017). 'A compact, transportable single-ion optical clock with  $7.8 \times 10^{-17}$  systematic uncertainty'. *Applied Physics B* **123**(4), p. 112.
- Cerretto, G., P. Tavella, and F. Lahaye (2008). 'Statistical constraints on station clock parameters in the NRCAN PPP estimation process'. In: *Proc. of the 2008 Precise Time and Time Interval (PTTI) Systems and Applications Meeting*.

- Cerretto, G., F. Lahaye, P. Tavella, and S. Vitrano (2010). 'Precise Point Positioning: Implementation of the constrained clock model and analysis of its effects in T/F transfer'. In: *EFTF-2010 24th European Frequency and Time Forum*, pp. 1–5.
- Chiodo, N. et al. (2015). 'Cascaded optical fiber link using the internet network for remote clocks comparison'. *Optics Express* **23**(26), pp. 33927–33937.
- Collins, P. (2008). 'Isolating and Estimating Undifferenced GPS Integer Ambiguities', in: *Proc. of the 2008 National Technical Meeting of The Institute of Navigation*. San Diego, CA, pp. 720–732.
- Collins, P., S. Bisnath, F. Lahaye, and P. Héroux (2010). 'Undifferenced GPS Ambiguity Resolution Using the Decoupled Clock Model and Ambiguity Datum Fixing'. *Navigation* **57**(2), pp. 123–135.
- Dach, R., T. Schildknecht, T. Springer, G. Dudle, and L. Prost (2002). 'Continuous time transfer using GPS carrier phase'. *IEEE Transactions on Ultrasonics, Ferroelectrics, and Frequency Control* **49**(11), pp. 1480–1490.
- Dach, R. et al. (2003). 'Time transfer using GPS carrier phase: error propagation and results'. *Journal of Geodesy* **77**(1-2), pp. 1–14.
- Dach, R., T. Schildknecht, U. Hugentobler, L.-G. Bernier, and G. Dudle (2006). 'Continuous geodetic time-transfer analysis methods'. *IEEE Transactions on Ultrasonics, Ferroelectrics and Frequency Control* **53**(7), pp. 1250–1259.
- Daubechies, I. (1992). 'Ten Lectures on Wavelets'. CBMS-NSF Regional Conference Series in Applied Mathematics. Society for Industrial and Applied Mathematics.
- Dawkins, S., J. McFerran, and A. Luiten (2007). 'Considerations on the measurement of the stability of oscillators with frequency counters'. *IEEE Transactions on Ultrasonics, Ferroelectrics and Frequency Control* **54**(5), pp. 918–925.
- Defraigne, P. and C. Bruyninx (2007). 'On the link between GPS pseudorange noise and day-boundary discontinuities in geodetic time transfer solutions'. *GPS Solutions* **11**(4), pp. 239–249.
- Defraigne, P. and J. M. Sleewaegen (2016). 'Code-Phase Clock Bias and frequency offset in PPP clock solutions'. *IEEE Transactions on Ultrasonics, Ferroelectrics, and Frequency Control* **63**(7), pp. 986–992.
- Defraigne, P., N. Guyennon, and C. Bruyninx (2008). 'GPS Time and Frequency Transfer: PPP and Phase-Only Analysis'. *International Journal of Navigation and Observation* **2008**, 175468.
- Delporte, J., F. Mercier, D. Laurichesse, and O. Galy (2008). 'GPS Carrier-Phase Time Transfer Using Single-Difference Integer Ambiguity Resolution'. *International Journal of Navigation and Observation* **2008**, e273785.
- Diddams, S. A. et al. (2000). 'Direct Link between Microwave and Optical Frequencies with a 300 THz Femtosecond Laser Comb'. *Physical Review Letters* **84**(22), pp. 5102–5105.
- Douglas, R. J. and J. S. Boulanger (1997). 'Standard uncertainty for average frequency traceability'. In: *Proc. of the 11th European Frequency and Time Forum*. Neuchatel, Switzerland, pp. 345–349.
- Dow, J. M., R. E. Neilan, and C. Rizos (2009). 'The International GNSS Service in a changing landscape of Global Navigation Satellite Systems'. *Journal of Geodesy* **83**(3-4), pp. 191–198.

- Droste, S. et al. (2013). 'Optical-Frequency Transfer over a Single-Span 1840 km Fiber Link'. *Physical Review Letters* **111**(11), p. 110801.
- Droste, S. et al. (2015). 'Characterization of a 450 km baseline GPS carrier-phase link using an optical fiber link'. *New Journal of Physics* **17**(8), p. 083044.
- Fonville, B., E. Powers, A. Kropp, and F. Vannicola (2007). 'Evaluation of carrier-phase GNSS timing receivers for UTC/TAI applications'. In: *39th Annual Precise Time and Time Interval (PTTI) Meeting*. Long Beach, CA, pp. 331–338.
- Fujieda, M. et al. (2014). 'Carrier-phase two-way satellite frequency transfer over a very long baseline'. *Metrologia* **51**(3), p. 253.
- Fujieda, M. et al. (2016). 'Frequency Measurement System of Optical Clocks Without a Flywheel Oscillator'. *IEEE Transactions on Ultrasonics, Ferroelectrics, and Frequency Control* **63**(12), pp. 2231–2236.
- Ge, M., G. Gendt, M. Rothacher, C. Shi, and J. Liu (2007). 'Resolution of GPS carrier-phase ambiguities in Precise Point Positioning (PPP) with daily observations'. *Journal of Geodesy* **82**(7), pp. 389–399.
- Geng, J., X. Meng, A. H. Dodson, and F. N. Teferle (2010). 'Integer ambiguity resolution in precise point positioning: method comparison'. *Journal of Geodesy* **84**(9), pp. 569–581.
- Geng, J. et al. (2012). 'Improving the estimation of fractional-cycle biases for ambiguity resolution in precise point positioning'. *Journal of Geodesy* **86**(8), pp. 579–589.
- Geng, J. and Y. Bock (2013). 'Triple-frequency GPS precise point positioning with rapid ambiguity resolution'. *Journal of Geodesy* **87**(5), pp. 449–460.
- Gill, P. (2016). 'Is the time right for a redefinition of the second by optical atomic clocks?' *Journal of Physics: Conference Series* **723**(1), p. 012053.
- Godun, R. et al. (2014). 'Frequency Ratio of Two Optical Clock Transitions in  $^{171}\text{Yb}^+$  and Constraints on the Time Variation of Fundamental Constants'. *Physical Review Letters* **113**(21), p. 210801.
- Gray, J. E. and D. W. Allan (1974). 'A Method for Estimating the Frequency Stability of an Individual Oscillator'. In: *28th Annual Symposium on Frequency Control*, pp. 243–246.
- Grebing, C. et al. (2016). 'Realization of a timescale with an accurate optical lattice clock'. *Optica* **3**(6), p. 563.
- Greenhall, C. A. (1998). 'Spectral ambiguity of Allan variance'. *IEEE Transactions on Instrumentation and Measurement* **47**(3), pp. 623–627.
- Guenta, J. et al. (2012). 'Progress in atomic fountains at LNE-SYRTE'. *IEEE Transactions on Ultrasonics, Ferroelectrics, and Frequency Control* **59**(3), pp. 391–409.
- Guyennon, N., G. Cerretto, P. Tavella, and F. Lahaye (2009). 'Further Characterization of the Time Transfer Capabilities of Precise Point Positioning (PPP): The Sliding Batch Procedure'. *IEEE Transactions on Ultrasonics, Ferroelectrics, and Frequency Control* **56**(8), pp. 1634–1641.
- Harris, F. J. (1978). 'On the use of windows for harmonic analysis with the discrete Fourier transform'. *Proceedings of the IEEE* **66**(1), pp. 51–83.
- Hatch, R. (1983). 'The synergism of GPS code and carrier measurements'. In: *Proc. of 3rd International Geodetic Symposium on Satellite Doppler Positioning*. Vol. 2. Las Cruces, New Mexico, pp. 1213–1231.

- Heavner, T. P. et al. (2014). 'First accuracy evaluation of NIST-F2'. *Metrologia* **51**(3), p. 174.
- Howe, D. A. and D. B. Percival (1994). 'Wavelet analysis for synchronization and timekeeping'. In: *Proceedings of IEEE 48th Annual Symposium on Frequency Control*, pp. 791–797.
- Huntemann, N. et al. (2012a). 'Generalized Ramsey Excitation Scheme with Suppressed Light Shift'. *Physical Review Letters* **109**(21), p. 213002.
- Huntemann, N. et al. (2012b). 'High-Accuracy Optical Clock Based on the Octupole Transition in  $^{171}\text{Yb}^{+}$ '. *Physical Review Letters* **108**(9), p. 090801.
- Huntemann, N. et al. (2014). 'Improved Limit on a Temporal Variation of  $m_p/m_e$  from Comparisons of  $\text{Yb}^{+}$  and  $\text{Cs}$  Atomic Clocks'. *Physical Review Letters* **113**(21), p. 210802.
- Huntemann, N., C. Sanner, B. Lipphardt, C. Tamm, and E. Peik (2016). 'Single-Ion Atomic Clock with  $3 \times 10^{-18}$  Systematic Uncertainty'. *Physical Review Letters* **116**(6), p. 063001.
- IGS Products (2017). <http://www.igs.org/products>. Accessed: 2017-05-01.
- Kalman, R. E. (1960). 'A New Approach to Linear Filtering and Prediction Problems'. *Journal of Basic Engineering* **82**(1), pp. 35–45.
- Kasdin, N. J. and T. Walter (1992). 'Discrete simulation of power law noise [for oscillator stability evaluation]'. In: *Proceedings of the 1992 IEEE Frequency Control Symposium*, pp. 274–283.
- Koller, S. et al. (2017). 'Transportable Optical Lattice Clock with  $7 \times 10^{17}$  Uncertainty'. *Physical Review Letters* **118**(7), p. 073601.
- Kouba, J. and T. Springer (2001a). 'New IGS Station and Satellite Clock Combination'. *GPS Solutions* **4**(4), pp. 31–36.
- Kouba, J. and P. Héroux (2001b). 'Precise Point Positioning Using IGS Orbit and Clock Products'. *GPS Solutions* **5**(2), pp. 12–28.
- Lagler, K., M. Schindelegger, J. Böhm, H. Krásná, and T. Nilsson (2013). 'GPT2: Empirical slant delay model for radio space geodetic techniques'. *Geophysical Research Letters* **40**(6), pp. 1069–1073.
- Lannes, A. and J.-L. Prieur (2013). 'Calibration of the clock-phase biases of GNSS networks: the closure-ambiguity approach'. *Journal of Geodesy* **87**(8), pp. 709–731.
- Larson, K. M., J. Levine, L. M. Nelson, and T. E. Parker (2000). 'Assessment of GPS carrier-phase stability for time-transfer applications'. *IEEE Transactions on Ultrasonics, Ferroelectrics, and Frequency Control* **47**(2), pp. 484–494.
- Laurichesse, D. and A. Blot (2016). 'Fast PPP convergence using multi-constellation and triple-frequency ambiguity resolution'. In: *Proc. of the IGS Workshop 2016*. Sydney, Australia.
- Laurichesse, D. and F. Mercier (2007). 'Integer ambiguity resolution on undifferenced GPS phase measurements and its application to PPP'. In: *Proc. of the 20th International Technical Meeting of the Satellite Division of The Institute of Navigation (ION GNSS 2007)*. Fort Worth, TX, pp. 839–848.
- Laurichesse, D., F. Mercier, J.-P. Berthias, P. Broca, and L. Cerri (2009). 'Integer Ambiguity Resolution on Undifferenced GPS Phase Measurements and Its Ap-



- plication to PPP and Satellite Precise Orbit Determination'. *Navigation* **56**(2), pp. 135–149.
- Lee, W.-K., D.-H. Yu, C. Y. Park, and J. Mun (2010). 'The uncertainty associated with the weighted mean frequency of a phase-stabilized signal with white phase noise'. *Metrologia* **47**(1), p. 24.
- Leute, J. et al. (2016). 'Frequency Comparison of Ion Optical Clocks at PTB and NPL via GPS PPP'. *IEEE Transactions on Ultrasonics, Ferroelectrics, and Frequency Control* **63**(7), pp. 981–985.
- Leute, J. and A. Wallin (2017). *jleute/colorednoise: thesis*. URL: <https://doi.org/10.5281/zenodo.244113>.
- Lewandowski, W., P. Moussay, J. Danaher, R. Gerlach, and E. LeVasseur (1997). 'Temperature-protected antennas for satellite time transfer receivers'. In: *Proc. of the 11th European Frequency and Time Forum 1997*. Warsaw, Poland, pp. 498–503.
- Lindsey, W. C. and C. M. Chie (1976). 'Theory of oscillator instability based upon structure functions'. *Proceedings of the IEEE* **64**(12), pp. 1652–1666.
- Lisdat, C. et al. (2016). 'A clock network for geodesy and fundamental science'. *Nature Communications* **7**, p. 12443.
- Lopez, O. et al. (2012). 'Ultra-stable long distance optical frequency distribution using the Internet fiber network'. *Optics Express* **20**(21), pp. 23518–23526.
- Loyer, S., F. Perosanz, F. Mercier, H. Capdeville, and J.-C. Marty (2012). 'Zero-difference GPS ambiguity resolution at CNES–CLS IGS Analysis Center'. *Journal of Geodesy* **86**(11), pp. 991–1003.
- Makdissi, A., F. Vernotte, and E. Clercq (2010). 'Stability variances: a filter approach'. *IEEE Transactions on Ultrasonics, Ferroelectrics and Frequency Control* **57**(5), pp. 1011–1028.
- Margolis, H. S. et al. (2013). 'International timescales with optical clocks (ITOC)'. In: *2013 Joint European Frequency and Time Forum International Frequency Control Symposium (EFTF/IFC)*, pp. 908–911.
- Margolis, H. S. (2015). personal communication.
- Marty, J.-C., ed. (2013). *Algorithmic Documentation of the GINS Software*. URL: [grgs.obs-mip.fr/content/download/1460/9226/file/GINS\\_Algo\\_2013.pdf](http://grgs.obs-mip.fr/content/download/1460/9226/file/GINS_Algo_2013.pdf).
- Matsakis, D., Z. Jiang, and W. Wu (2015). 'Carrier phase and pseudorange disagreement as revealed by Precise Point Positioning solutions'. In: *2015 Joint Conference of the IEEE International Frequency Control Symposium the European Frequency and Time Forum*, pp. 717–722.
- Melbourne, W. G. (1985). 'The case for ranging in GPS-based geodetic systems'. In: *Proc. of the first international symposium on precise positioning with the Global Positioning System*. Rockville, Maryland, pp. 373–386.
- Mercier, F. and D. Laurichesse (2008). 'Zero-difference ambiguity blocking properties of satellite/receiver widelane biases'. In: *Proc. of European navigation conference*. Toulouse, France.
- Mervart, L., L. Zdenek, C. Rocken, and T. Iwabuchi (2008). 'Precise Point Positioning with Ambiguity Resolution in Real-Time,' in: *Proc. of the 21st International Technical Meeting of the Satellite Division of The Institute of Navigation (ION GNSS 2008)*. Savannah, GA, pp. 397–405.

- Mosteller, F. and J. W. Tukey (1977). 'Data analysis and regression. A second course in statistics'. Reading, MA: Addison-Wesley.
- Nand, N. R., J. G. Hartnett, E. N. Ivanov, and G. Santarelli (2011). 'Ultra-Stable Very-Low Phase-Noise Signal Source for Very Long Baseline Interferometry Using a Cryocooled Sapphire Oscillator'. *IEEE Transactions on Microwave Theory and Techniques* **59**(11), pp. 2978–2986.
- Nicholson, T. L. et al. (2015). 'Systematic evaluation of an atomic clock at  $2 \times 10^{-18}$  total uncertainty'. *Nature Communications* **6**, p. 6896.
- Odijk, D., B. Zhang, A. Khodabandeh, R. Odolinski, and P. J. G. Teunissen (2016). 'On the estimability of parameters in undifferenced, uncombined GNSS network and PPP-RTK user models by means of  $\mathcal{S}$ -system theory'. *Journal of Geodesy* **90**(1), pp. 15–44.
- Orgiazzi, D., P. Tavella, and F. Lahaye (2005). 'Experimental assessment of the time transfer capability of precise point positioning (PPP)'. In: *Proc. of the 2005 IEEE International Frequency Control Symposium and Exposition*, pp. 337–345.
- Overney, F., L. Prost, U. Feller, T. Schildknecht, and G. Beutler (1997). 'GPS Time Transfer Using Geodetic Receivers: Middle Term Stability and Temperature Dependence of the Signal Delays'. In: *Proc. of the 11th European Frequency and Time Forum EFTF 97*. Warsaw, Poland, pp. 504–508.
- Panfilo, G. and T. E. Parker (2010). 'A theoretical and experimental analysis of frequency transfer uncertainty, including frequency transfer into TAI'. *Metrologia* **47**(5), p. 552.
- Pearson, K. (1895). 'Note on Regression and Inheritance in the Case of Two Parents'. *Proceedings of the Royal Society of London* **58**, pp. 240–242.
- Percival, D. B. (2016). 'A Wavelet Perspective on the Allan Variance'. *IEEE Transactions on Ultrasonics, Ferroelectrics, and Frequency Control* **63**(4), pp. 538–554.
- Percival, D. and A. Walden (2006). 'Wavelet Methods for Time Series Analysis'. Cambridge Series in Statistical and Probabilistic Mathematics. Cambridge University Press.
- Petit, G. and Z. Jiang (2008a). 'GPS All in View time transfer for TAI computation'. *Metrologia* **45**(1), p. 35.
- Petit, G. and B. Luzum, eds. (2010). 'IERS Conventions (2010)'. IERS Technical Note 36. Frankfurt am Main: Verlag des Bundesamts für Kartographie und Geodäsie.
- Petit, G., A. Harmegnies, F. Mercier, F. Perosanz, and S. Loyer (2011). 'The time stability of PPP links for TAI'. In: *2011 Joint Conference of the IEEE International Frequency Control and the European Frequency and Time Forum (FCS) Proceedings*, pp. 1–5.
- Petit, G. and Z. Jiang (2008b). 'Precise Point Positioning for TAI Computation'. *International Journal of Navigation and Observation* **2008**, pp. 1–8.
- Petit, G. and P. Defraigne (2016). 'The performance of GPS time and frequency transfer: comment on 'A detailed comparison of two continuous GPS carrier-phase time transfer techniques''. *Metrologia* **53**(3), pp. 1003–1008.
- Powers, E., P. Wheeler, D. Judge, and M. Demetrios (1998). 'Hardware Delay Measurements and Sensitivities in Carrier Phase Time Transfer,' in: *Proc. of the 30th Annual Precise Time and Time Interval Systems and Applications Meeting*. Reston, Virginia, pp. 293–306.

- Predehl, K. et al. (2012). 'A 920-Kilometer Optical Fiber Link for Frequency Metrology at the 19th Decimal Place'. *Science* **336**(6080), pp. 441–444.
- Raupach, S. M. F., A. Koczwara, and G. Grosche (2015). 'Brillouin amplification supports  $1 \times 10^{-20}$  uncertainty in optical frequency transfer over 1400 km of underground fiber'. *Physical Review A* **92**(2), p. 021801.
- Ray, J. and K. Senior (2001). 'Temperature Sensitivity of Timing Measurements Using Dorne Margolin Antennas'. *GPS Solutions* **5**(1), pp. 24–30.
- Ray, J. and K. Senior (2003). 'IGS/BIPM pilot project: GPS carrier phase for time/frequency transfer and timescale formation'. *Metrologia* **40**(3), pp. 270–288.
- Ray, J. and K. Senior (2005). 'Geodetic techniques for time and frequency comparisons using GPS phase and code measurements'. *Metrologia* **42**(4), pp. 215–232.
- Rieck, C., P. Jarlemark, K. Jaldehag, and J. Johansson (2003). 'Thermal influence on the receiver chain of GPS carrier phase equipment for time and frequency transfer'. In: *Proc. of the IEEE International Frequency Control Symposium and PDA Exhibition Jointly with the 17th European Frequency and Time Forum 2003*, pp. 326–331.
- Rioul, O. and P. Duhamel (1992). 'Fast algorithms for discrete and continuous wavelet transforms'. *IEEE Transactions on Information Theory* **38**(2), pp. 569–586.
- Rothacher, M. and G. Beutler (1998). 'The role of GPS in the study of global change'. *Physics and Chemistry of the Earth* **23**(9), pp. 1029–1040.
- Rothacher, M and R Schmid (2010). *ANTEX: The antenna exchange format version 1.4*. URL: <ftp://igs.cb.jpl.nasa.gov/igs.cb/station/general/antex14.txt>.
- Rubiola, E., M. Lenczner, P. Y. Bourgeois, and F. Vernotte (2016). 'The Counter, a Frequency Counter Based on the Linear Regression'. *IEEE Transactions on Ultrasonics, Ferroelectrics, and Frequency Control* **63**(7), pp. 961–969.
- Rubiola, E. (2005). 'On the measurement of frequency and of its sample variance with high-resolution counters'. *Review of Scientific Instruments* **76**(5), p. 054703.
- Rutman, J. (1974). 'Characterization of Frequency Stability: A Transfer Function Approach and Its Application to Measurements via Filtering of Phase Noise'. *IEEE Transactions on Instrumentation and Measurement* **23**(1), pp. 40–48.
- Rutman, J. (1978). 'Characterization of phase and frequency instabilities in precision frequency sources: Fifteen years of progress'. *Proc. of the IEEE* **66**(9), pp. 1048–1075.
- Samain, E. et al. (2008). 'Time transfer by laser link – the t2l2 experiment on jason-2 and further experiments'. *International Journal of Modern Physics D* **17**(07), pp. 1043–1054.
- Schmid, R., P. Steigenberger, G. Gendt, M. Ge, and M. Rothacher (2007). 'Generation of a consistent absolute phase-center correction model for GPS receiver and satellite antennas'. *Journal of Geodesy* **81**(12), pp. 781–798.
- Schoenberg, I. J. (1946). 'Contributions to the problem of approximation of equidistant data by analytic functions. Part A. On the problem of smoothing or graduation. A first class of analytic approximation formulae'. *Quarterly of Applied Mathematics* **4**(1), pp. 45–99.
- Seeber, G. (2003). 'Satellite geodesy'. 2nd completely rev. and extended ed. Berlin, New York: Walter de Gruyter.

- Seepersad, G., S. Banville, P. Collins, S. Bisnath, and F. Lahaye (2016). 'Integer Satellite Clock Combination for Precise Point Positioning with Ambiguity Resolution'. In: *Proc. of the 29th International Technical Meeting of The Satellite Division of the Institute of Navigation (ION GNSS+ 2016)*. Portland, Oregon.
- Senior, K. and J. Ray (2001). 'Accuracy and Precision of GPS Carrier-Phase Clock Estimates'. In: *Proc. of the 33th Annual Precise Time and Time Interval Systems and Applications Meeting*. Long Beach, California, pp. 199–220.
- Senior, K. L., J. R. Ray, and R. L. Beard (2008). 'Characterization of periodic variations in the GPS satellite clocks'. *GPS Solutions* **12**(3), pp. 211–225.
- Sesia, I. and P. Tavella (2008). 'Estimating the Allan variance in the presence of long periods of missing data and outliers'. *Metrologia* **45**(6), S134.
- Shi, J. and Y. Gao (2014). 'A comparison of three PPP integer ambiguity resolution methods'. *GPS Solutions* **18**(4), pp. 519–528.
- Śliwczyński, L., P. Krehlik, A. Czubla, L. Buczek, and M. Lipiński (2013). 'Dissemination of time and RF frequency via a stabilized fibre optic link over a distance of 420 km'. *Metrologia* **50**(2), p. 133.
- Tamm, C., S. Weyers, B. Lipphardt, and E. Peik (2009). 'Stray-field-induced quadrupole shift and absolute frequency of the 688-THz  $^{171}\text{Yb}^+$  single-ion optical frequency standard'. *Physical Review A* **80**(4), p. 043403.
- Tamm, C. et al. (2014). 'Cs-based optical frequency measurement using cross-linked optical and microwave oscillators'. *Physical Review A* **89**(2), p. 023820.
- Terrien, J. (1968). 'News from the International Bureau of Weights and Measures'. *Metrologia* **4**(1), p. 41.
- Teunissen, P. J. G. and A. Khodabandeh (2015). 'Review and principles of PPP-RTK methods'. *Journal of Geodesy* **89**(3), pp. 217–240.
- Teunissen, P. J., D. Odijk, and B.-C. Zhang (2010). 'PPP-RTK: Results of CORS Network-Based PPP with Integer Ambiguity Resolution'. *Journal of Aeronautics, Astronautics and Aviation. Series A* **42**(4), pp. 223–229.
- Unser, M., A. Aldroubi, and M. Eden (1992). 'On the asymptotic convergence of B-spline wavelets to Gabor functions'. *IEEE Transactions on Information Theory* **38**(2), pp. 864–872.
- Unser, M., A. Aldroubi, and S. J. Schiff (1994). 'Fast implementation of the continuous wavelet transform with integer scales'. *IEEE Transactions on Signal Processing* **42**(12), pp. 3519–3523.
- Vernotte, F., M. Lenczner, P. Y. Bourgeois, and E. Rubiola (2016). 'The Parabolic Variance (PVAR): A Wavelet Variance Based on the Least-Square Fit'. *IEEE Transactions on Ultrasonics, Ferroelectrics, and Frequency Control* **63**(4), pp. 611–623.
- Vernotte, F. and D. A. Howe (2000). 'Generalization of the Total Variance Approach to the Different Classes of Structure Functions'. In: *Proc. of the 14th European Frequency and Time Forum EFTF*. Torino, Italy.
- Weinbach, U (2013). 'Feasibility and impact of receiver clock modeling in precise GPS data analysis'. In: *Wissenschaftliche Arbeiten der Fachrichtung Geodäsie und Geoinformatik der Leibniz Universität Hannover*. Nr. 303. Leibniz Universität Hannover.

- Weiss, M. A., G. Petit, and Z. Jiang (2005). 'A comparison of GPS common-view time transfer to all-in-view'. In: *Proceedings of the 2005 IEEE International Frequency Control Symposium and Exposition, 2005*. P. 5.
- Weiss, M., P. Fenton, E. Powers, and K. Senior (2004). 'Frequency transfer using Precise Point Positioning'. In: *18th European Frequency and Time Forum (EFTF 2004)*, pp. 623–629.
- Weissstein, E. W. (2017). "Sinc Function." From MathWorld—A Wolfram Web Resource. <http://mathworld.wolfram.com/SincFunction.html>.
- Witt, T. J. (2009). 'Practical methods for treating serial correlations in experimental observations'. *The European Physical Journal Special Topics* **172**(1), pp. 137–152.
- Wu, J., S. Wu, G. Hajj, W. Bertiger, and S. Lichten (1993). 'Effects of Antenna Orientation on GPS Carrier Phase Measurements'. *Manuscripta Geodaetica* (18), pp. 91–98.
- Wübbena, G (1985). 'Software developments for geodetic positioning with GPS using TI-4100 code and carrier measurements'. In: *Proc. of the first international symposium on precise positioning with the global positioning system*. Rockville, Maryland, pp. 403–412.
- Wübbena, G., M. Schmitz, and A. Bagge (2005). 'PPP-RTK: Precise Point Positioning Using State-Space Representation in RTK Networks'. In: *Proc. of the 18th International Technical Meeting of the Satellite Division of The Institute of Navigation (ION GNSS 2005)*. Long Beach, CA, pp. 2584–2594.
- Yao, J. and J. Levine (2013). 'A New Algorithm to Eliminate GPS Carrier-phase Time Transfer Boundary Discontinuity,' in: *Proc. of the 45th Annual Precise Time and Time Interval Systems and Applications Meeting*. Bellevue, Washington, pp. 292–303.
- Yao, J. and J. Levine (2014). 'An Improvement of RINEX-Shift Algorithm for Continuous GPS Carrier-Phase Time Transfer,' in: *Proc. of the 27th International Technical Meeting of The Satellite Division of the Institute of Navigation (ION GNSS+ 2014)*. Tampa, Florida, pp. 1253–1260.
- Yao, J., I. Skakun, Z. Jiang, and J. Levine (2015). 'A detailed comparison of two continuous GPS carrier-phase time transfer techniques'. *Metrologia* **52**(5), pp. 666–676.
- Yu, D.-H., M. Weiss, and T. E. Parker (2007). 'Uncertainty of a frequency comparison with distributed dead time and measurement interval offset'. *Metrologia* **44**(1), p. 91.
- Zhang, N. F. (2006). 'Calculation of the uncertainty of the mean of autocorrelated measurements'. *Metrologia* **43**(4), S276.
- Zumberge, J. F., M. B. Heflin, D. C. Jefferson, M. M. Watkins, and F. H. Webb (1997). 'Precise point positioning for the efficient and robust analysis of GPS data from large networks'. *Journal of Geophysical Research: Solid Earth* **102**(B3), pp. 5005–5017.



## ACKNOWLEDGMENTS

---

This work would not have been possible without the work and support of many colleagues. First of all I want to thank Ekkehard Peik and Steffen Schön for examining this work.

I'm grateful to Felicitas Arias and Gérard Petit for the opportunity to spend two months at BIPM to work on the IPPP processing for this work. I enjoyed the strolls in the Parc de Saint-Cloud with Gianna Panfilo, Aurélie Harmegnies, Hawaiï Konaté and Laurent Tisserand. I'd also like to thank Sylvain Loyer and Félix Perosanz for their support and their work on IPPP.

Special thank goes to the group of Gesine Grosche including Christian Grebing, Sebastian Raupach and Sebastian Koke for fruitful collaboration and their work on the optical fiber links. Thanks also goes to Burghard Lippard who connects the microwave and the optical regime. I'm also grateful to our colleagues on the other ends of the fiber links, Ronald Holzwarth and Stefan Droste for the MPQ link, and the group of Paul-Eric Pottie for the link to LNE-SYRTE.

Many people contributed to the ITOC project. I would like to thank Helen Margolis for the project coordination and the colleagues from NPL, INRIM, PTB, LNE-SYRTE and Mittatekniikan keskus (MIKES) that contributed to this project. Giancarlo Cerretto, Peter Whibberley, and Daniele Rovera kindly provided the GPS data from their GPS stations. I'm thankful for fruitful discussions and feedback from Pascale Defraigne, Daniele Rovera, Erik Benkler, Giancarlo Cerretto, Anders Wallin, Helen Margolis, Rachel Godun, Peter Whibberley and Peter Nisbet-Jones.

I would like to thank Nils Huntemann for his work on the  $\text{Yb}^+$  clocks at PTB, for proof reading this thesis and for his constructive criticism.

Last but not least I would like to thank my colleagues from the time dissemination group at PTB Andreas Bauch, Dirk Piester, Franziska Riedel, Thomas Polewka, Jürgen Becker, and Egle Staliuniene for their work and valuable support over the years.





# Curriculum vitæ

---

## Persönliche Daten

Name Julia Leute  
Geburtsdatum 7. Januar 1987  
Geburtsort Obertaufkirchen

---

## Ausbildung

Juli 2003 **Realschulabschluss**, *Realschule am Judenstein*, Regensburg.  
Juni 2007 **Abitur**, *Goethe-Gymnasium*, Regensburg.  
Okt. 2007 – Apr. 2013 **Studium der Physik mit Abschluss als Diplom-Physikerin**,  
*Technische Universität München*, Garching.

---

## Berufstätigkeit

Mai 2013 – Juni 2013 **Wissenschaftliche Mitarbeiterin**, *Excellence Cluster Universe*,  
*Technische Universität München*, Garching.  
Nov. 2013 – April 2017 **Wissenschaftliche Mitarbeiterin**, *Physikalisch-Technische Bundesanstalt*, Braunschweig.